

DISSERTATION

THE EFFECTS OF STRUCTURAL CONFINEMENT AND THERMAL PROFILES ON
PROPAGATING SPIN WAVES

Submitted by

Grant Alston Riley

Department of Physics

In partial fulfillment of the requirements

For the Degree of Doctor of Philosophy

Colorado State University

Fort Collins, Colorado

Spring 2018

Doctoral Committee:

Advisor: Kristen S. Buchanan

James Neilson
David Krueger
Carl Patton

Copyright by Grant Alston Riley 2018

All Rights Reserved

ABSTRACT

THE EFFECTS OF STRUCTURAL CONFINEMENT AND THERMAL PROFILES ON PROPAGATING SPIN WAVES

Spintronics is a growing field that relies on the spin degree of freedom in the form of spin currents instead of electronic charge to transmit and process information. There are many advantages to spin-based devices including scalability, a wide range of host materials including insulators, and almost no energy loss due to Joule heating. Spin angular momentum can be transmitted in the form of spin-polarized currents that flow through a metal, pure spin currents, or in the form of spin waves, disturbances in the magnetization state that can propagate and hence can carry energy. If such a spin-based paradigm is to be realized, there are many open questions that must be addressed. Two questions of particular importance are: how can short wavelength spin waves that are needed for information transmission be controllably generated? and once generated, how can these spin waves be modified and controlled?

This thesis focusses on answering both of these questions through the investigation of spin waves in two different types of samples, patterned microstructures and thin continuous films, performed using Brillouin light scattering (BLS) spectroscopy. In the first experiment, the possibility of generating short wavelength spin waves by dynamically exciting a non-uniform magnetic state called the antivortex (AV) in a Permalloy microstructure is explored. Frequency scans were performed to identify a spectrum of high-frequency modes of the AV state. These modes were then individually mapped out by pumping at the frequency of the mode and performing spatially-resolved BLS scans. Comparing the experimental results with

dispersion curves and micromagnetic simulations reveals that some of most prominent modes involve coupling of the AV dynamics to propagating spin waves in the adjacent nanowires highlighting the fact that the local magnetization state has a significant effect on the spin wave dynamics. Due to the natural way that an antivortex state can be incorporated into a nanowire network, this spin configuration may be useful as a means to generate or control spin waves for applications.

In the second study we explore the possibility of modifying the propagation characteristics of both spin waves and spin caustic beams, which could be highly useful in spin-wave-based logic devices, using non-uniform thermal gradients up to 4.5 K/mm. These experiments were performed in a yttrium iron garnet (YIG) thin film - a model system for studying spin waves due to extremely low damping characteristics. An intricate diamond-shaped propagation pattern was observed and explained using the dispersion manifold for the YIG film and considering the range of wavevectors excited by the antenna. Significant modifications to the propagation characteristics such as beam angle, temporal pulse shape, mode profiles, and group velocity were observed as spin waves travelled into heated regions. These results will serve to broaden the understanding of how heat can be used to affect and control spin waves.

ACKNOWLEDGEMENTS

This work would not have been possible without the considerable support of my advisor Kristen S. Buchanan. She fosters an environment of “hands-off” leadership which gives freedom for her students to pursue a wide range of unanticipated yet exciting research directions. Her commitment to the highest degree of excellence in every publication and presentation consistently challenged me to form and then polish the most compelling interpretation of the data. I am also grateful for her financial support and sponsorship to have many opportunities to travel to share findings and network with other scientists in our field. Her support in every aspect of research and her students’ general well being is a hallmark of her leadership. I am also indebted to my committee for taking the time to participate in the many hurdles required to earn graduate degrees.

I want to thank H. J. Jason Liu who laid the foundation of solid lab practices, built the apparatus which I used for so many experiments, taught me how to get the most out of a conference, for the hands-on instruction he provided, and for being a great friend outside the lab. I am thankful for Martin Asmat-Uceda for many useful discussions of spin wave dynamics and his support in numerical calculations. I owe a big debt of gratitude to Cesar L. Ordonez-Romero for sharing the inspiration to pursue several projects, for many fruitful chalkboard style conversations, thorough instruction in spin wave dispersion, and microwave circuits and characterization. I would like to thank my other lab mates, most notably Katie Nygren for being an interested learner and thinking of improvements to several methods and lab practices that will no doubt make the BLS lab run more efficiently. I want to thank all my fellow graduate students who contributed to my success and helped me maintain my sanity through the late nights and stressful times. I consider Joel Finkeldei and James

Hitchman to be almost like war buddies after all that we went through together. My sincere appreciation goes to Christine Purba for the support and encouragement she brought during the last year, perhaps when I needed it most. Many other friends from church played an integral role in giving me a strong social network upon which I relied through many of the most difficult times in my life.

Most importantly, I want to thank my parents. Without your support in every aspect of life I would not have attained this monumental achievement. Dad, thank you for all the late night discussions that made me excited about the philosophy of science. I also want to thank you for pushing me to help in so many hands-on projects that gave me such a breadth of understanding on how to approach so many different problems. Mom, you gave me the confidence and inspiration to really believe in myself and know that I could achieve anything I set my mind to. You shaped me to be who I am today and there is not a day that I do not think of you. Your memory will forever be so dearly cherished. This dissertation is dedicated to you both.

Thermal project: I acknowledge César Ordóñez-Romero for many fruitful discussions and supplying the YIG films. Katherine Nygren assisted in collecting a portion of the short pulse TR-BLS data and Melissa Aguilar helped with FMR and SQUID measurements. We are also grateful to Prof. John William (Mechanical Engineering, CSU) and his students for helping us use their thermal camera on several occasions. We acknowledge support from the U.S. Department of Energy, Office of Basic Energy Sciences, Division of Materials Sciences and Engineering under Award #ER 46854 and by UNAM-DGAPA Grant No. 1N103915.

Antivortex project: This work builds upon studies of the success of AV formation in various structure sizes and geometries as described in Refs. [1, 2]. Martin Asmat-Uceda

assisted with the MFM measurements and performed the micromagnetic simulations and analysis. Please refer to Martin's thesis [3] for more detailed information on the simulations and a more in-depth analysis of the effect of structure size and shape on the observed AV dynamics. H. J. Jason Liu and Katherine Nygren assisted occasionally with micro-BLS data collection. This research was supported by the U.S. Department of Energy, Office of Basic Energy Sciences, Division of Materials Sciences and Engineering under Award No. ER 46854 (experiments and simulations) and the National Institute of Standards and Technology Grant No. 60NANB10D011 (development of the micro-BLS). Use of the Center for Nanoscale Materials, an Office of Science user facility, was supported by the U.S. Department of Energy, Office of Science, Office of Basic Energy Sciences, under Contract No. DE-AC02-06CH11357.

This dissertation is typeset in \LaTeX using a document class designed by Leif Anderson.

TABLE OF CONTENTS

Abstract	ii
Acknowledgements	iv
List of Tables	xi
List of Figures	xii
List of Symbols	xv
List of Acronyms	xvii
Chapter 1. Introduction	1
1.1. Motivation	1
1.2. Objectives	4
1.3. Outline of thesis	4
Chapter 2. Review of magnetism and magnetic materials	7
2.1. Magnetic moments	7
2.2. Magnetostatic energies	11
2.3. Domains and saturation	12
2.4. Magnetic anisotropy	14
2.5. Magnetization dynamics	14
2.5.1. Equation of motion	14
2.5.2. Uniform precession	16
2.6. Spin waves	18
2.7. Spin wave modes	19

2.8.	Dispersion theory	20
2.8.1.	Partial wave (PW) method	21
2.8.2.	Spin wave mode (SWM) method	22
2.8.3.	Nature of solutions	28
2.8.4.	Limiting cases	31
2.9.	Conclusions	34
Chapter 3.	Characterization techniques	35
3.1.	Introduction	35
3.2.	Ferromagnetic resonance	35
3.3.	Magnetometry	38
3.3.1.	Vibrating sample magnetometry	38
3.3.2.	SQUID magnetometry	40
3.4.	Light scattering	40
3.4.1.	Mechanism of light scattering with magnetic materials	42
3.4.2.	Brillouin light scattering	44
3.4.2.1.	Conventional BLS	51
3.4.2.2.	Micro-BLS	55
3.5.	Summary	57
Chapter 4.	Dynamic excitation of a magnetic antivortex	59
4.1.	Introduction	59
4.2.	Background and motivation	59
4.3.	Experimental setup	62
4.3.1.	In-plane excitation	62

4.3.2.	Out-of-plane excitation	64
4.4.	Experimental results	66
4.4.1.	In-plane excitation	67
4.4.1.1.	Frequency scans	67
4.4.1.2.	2D position scans	70
4.4.1.3.	Compare with simulations	71
4.4.1.4.	Discussion	77
4.4.2.	Out-of-plane excitation	80
4.4.2.1.	Frequency scans	81
4.4.2.2.	2D position scans	82
4.4.2.3.	Compare with simulations	83
4.5.	Summary	86
Chapter 5.	Thermal control of spin waves	88
5.1.	Motivation	88
5.2.	Effects of thermal profiles on spin wave dynamics	89
5.3.	Experimental setup	90
5.4.	Results and discussion	95
5.4.1.	Spectral profile	95
5.4.2.	2D BLS scans	97
5.5.	Calculated dispersion relations	99
5.6.	Short pulse excitation	105
5.7.	Project summary	113
Chapter 6.	Summary	115

6.1. Future directions	116
Bibliography	118
Appendix A. Catalog of modes	137
A.1. List of modes to accompany Chapter 4	137
Appendix B. Dispersion calculator	139
B.1. How to use the code	139
B.1.1. The interface script	140
B.1.2. The calculating function	141

LIST OF TABLES

A.1	List of modes for experimental data for in-plane excitation.....	137
A.2	List of modes for simulation data for in-plane excitation.....	137
A.3	List of modes for experimental data for out-of-plane excitation.....	137
A.4	List of modes for simulation data for out-of-plane excitation.....	138

LIST OF FIGURES

2.1	Classification of magnetic materials	10
2.2	Hysteresis loop of a ferromagnet	13
2.3	Illustration of the FMR mode.....	17
2.4	Spin wave diagram.....	19
2.5	Dispersion relation geometry.....	25
2.6	Experimental evidence of pinning parameters	26
2.7	Spin wave manifold for in-plane magnetization	29
2.8	Spin wave dispersion relations for BV and DE configurations.....	30
2.9	Dipole gaps in dispersion curves	30
2.10	Thickness dependence of the dynamic magnetization	31
2.11	Limiting cases of spin wave dispersion.....	32
3.1	FMR experimental diagram.....	37
3.2	VSM experimental diagram.....	39
3.3	Typical SQUID measurement.....	40
3.4	MOKE experimental configurations.....	45
3.5	Illustration of magnon creation and annihilation	46
3.6	Overview of BLS apparatus and TFP interferometer	49
3.7	TFP interferometer transmission spectrum.....	50
3.8	BLS beam path for the back-scattering configuration.....	52
3.9	BLS beam path for the forward-scattering configuration.....	52

3.10	Screenshot of BLS user interface	54
3.11	Diagram of micro-BLS apparatus	55
3.12	Screenshot of micro-BLS user interface.....	57
4.1	Spin distribution of magnetic vortex and antivortex states.....	61
4.2	SEM image of AV microstructure: in-plane excitation	63
4.3	MFM images of pound-key structures: in-plane excitation.....	65
4.4	SEM image of AV microstructure: out-of-plane excitation.....	66
4.5	Complex frequency scan extraction	68
4.6	Laser intensity fluctuation	69
4.7	Spectral response of antivortex with in-plane excitation	70
4.8	2D mode profiles of antivortex with in-plane excitation.....	72
4.9	Simulated spectral response and 2D mode profiles of the antivortex	74
4.10	Frequency spectrum of AV with out-of-plane excitation	82
4.11	2D position scan of AV with out-of-plane excitation.....	83
4.12	Simulated spectral response and mode profiles for the AV with out-of-plane excitation.....	85
5.1	Experimental setup for YIG thermal project	91
5.2	$4\pi M_S(T)$ for YIG.....	92
5.3	Temperature profile for YIG	92
5.4	$4\pi M_S(x)$ for YIG	93
5.5	2D Temperature profile of the YIG film	94

5.6	Spectral response for YIG in DE geometry	95
5.7	BLS 2D profiles.....	97
5.8	BLS 2D profile comparison for room temp vs heat	98
5.9	Dispersion surfaces and slowness curves for YIG	100
5.10	Thermal effects on group velocity and beam angle.....	102
5.11	Thermal effects on time-resolved pulse shape.....	104
5.12	Temperature profile for YIG for short pulse excitation	107
5.13	TR-BLS data of short pulses in a thermal gradient.....	108
5.14	Decay of a short spin wave pulse traveling into a thermal gradient.....	109
5.15	Spatial extent of a pulse traveling into a thermal gradient.....	110
5.16	Arrival time and width of a short spin wave pulse traveling into a thermal gradient	111
5.17	Pulse shape evolution of short spin wave pulses traveling into a thermal gradient .	112
5.18	Deceleration of a short spin wave pulse traveling into a thermal gradient	113

LIST OF SYMBOLS

B	Magnetic induction.	(G)
H	Magnetic field.	(Oe)
h	Dynamic magnetic field.	(Oe)
N	Demagnetization factor.	(unitless)
m	Magnetic moment.	(emu)
M	Volume magnetization.	(emu/cm ³)
$4\pi M_S$	Saturation magnetization.	(G)
g	Landé g-factor.	(unitless)
$\gamma/2\pi$	Gyromagnetic ratio.	(Hz/Oe)
α	Exchange parameter.	(cm ²)
λ	Wavelength.	(nm)
f_p	Pumping frequency.	(GHz)
v_g	Group velocity.	(μm/ns)
t	Thickness.	(nm)
b	Antivortex structure dimensions.	(μm)
f_p	Pumping frequency.	(GHz)

d Antenna width..... (μm)

LIST OF ACRONYMS

FMR	Ferromagnetic resonance
FVSW	Forward volume spin wave
BVSW	Backward volume spin wave
SSW	Surface spin wave
BLS	Brillouin light scattering
TR-BLS	Time-resolved Brillouin light scattering
BV	Backward volume
DE	Damon-Eshbach
FP1	First Fabry-Perot interferometer
FP2	Second Fabry-Perot interferometer
FSR	Free spectral range
YIG	Yttrium iron garnet
AV	Antivortex
Sat	State saturated parallel to the dynamic field h
Sat _⊥	State saturated perpendicular to the dynamic field h

CHAPTER 1

INTRODUCTION

1.1. MOTIVATION

Ferromagnetic (FM) materials have had a long lasting and far reaching impact on humanity. From the earliest discoveries of lodestone, iron ore with intrinsic magnetization, several thousand years ago people have found the unique properties of FM materials to be of great benefit. The first well-known widespread application of a FM material was to suspend a ferromagnet in a fluid to form a compass that enabled accurate navigation using the magnetic flux lines that follow the longitude lines around the earth. Understanding of the properties of magnetic materials took a giant leap in the 19th century with the foundational scientific exploits of giants like Oersted, Ampère, Gauss, Biot, Savart, Faraday and Maxwell [4, 5]. With these theoretical and experimental foundations magnets began to have widespread use. Soon after discovering the interplay between electricity and magnetism, generators and electric motors became a pivotal part of energy conversion in the industrial age.

Perhaps the most significant is the use of FM materials as media for information storage. Taking many forms from the magnetic tapes used in audio and video cassette tapes, and magnetic tape drives to the modern hard disk drive (HDD), the ability to reliably store and recall information has been the foundation upon which the information age has been established. Another important application is in communication technology from microphones to speakers to microwave communication technology. FM materials have also shown up in commerce in the black strip on the back of credit and debit cards forming a confidential and reliable way to transfer funds. Permanent FM materials have found new applications in nanoscale architectures used to improve the contrast in magnetic resonance imaging (MRI)

to more quickly, accurately, and non-invasively detect physical abnormalities in the body. New FM materials may even play an important role in the development of super speed trains that rely on low-friction magnetic levitation.

As a result of the sheer ubiquity of magnetic materials in modern technology, magnetics research is a crucially important part of scientific exploration. The commercial impetus to improve such magnet-based devices to become faster, more efficient, and smaller has motivated the quest to understand magnetic materials better to predict and control their behavior. Having this said, magnetic materials are formed by very complex electromagnetic interactions with many constituent elements that result in intrinsically interesting behavior. Because of this complexity, magnetic materials form an excellent test bed for many interactions that are otherwise difficult or inefficient to study.

Anyone remotely familiar with information storage knows that solid state drives are superior to HDDs in nearly every relevant metric. They are faster, do not require defragmentation, are far more durable, have smaller form factors, less noise, and consume less power. However HDDs still have a better capacity-to-cost ratio that will give them a significant market share for some time to come and there are several big ideas coming down the pipeline to continue improving HDD technology. Aside from the commercial motivation to study magnetic materials there are many fundamental emerging topics within magnetics research that appear quite removed from application at first glance yet act to move the field forward. From a materials perspective, there is always active research to improve or discover new hard and soft magnets and find new applications for these materials. There is a growing sub-field under the umbrella of magneto-electronics, a field that explores the interaction

between spin and electronic systems, producing novel ideas that show great potential for replacing conventional charge-based electronic devices. Magnetic recording research is showing new potential with studies in structured/patterned media or heat-assisted recording. Most relevant to the work presented in this thesis is research in magnetization dynamics, that is the study of how spins move, especially on fast time scales or high frequencies (e.g., GHz range) with implications for communications devices or to better understand issues in magnetic memory technology. Fundamental research in this field includes research in magnonics, the study of spin waves in nanostructured devices, domain wall motion and the associated dynamics, and ultrafast/optical switching of the local magnetic state [6].

In our lab, we have a powerful and somewhat rare experimental technique called Brillouin light scattering (BLS) spectroscopy, which is particularly well suited for studying magnetization dynamics [7]. This technique relies on measuring the frequency shifts of inelastically scattered light and has many salient features including the fact that it is a non-invasive and non-destructive measurement technique. It also allows for the control of many experimental parameters such as frequency, field, probed wavevector, and it is flexible enough that many different experimental geometries are possible. The intensity of light scattered from a magnetic sample is recorded as a function of the frequency shift of the photons using a sensitive interferometer. The depth sensitivity depends on the optical properties and the experimental setup. BLS measurements can also be performed on the sub-micron scale with the aid of a microscope objective. The BLS technique will be discussed in more detail in Chapter 3.

1.2. OBJECTIVES

The experimental work presented in this thesis focuses on two studies of magnetization dynamics: one looking at the excitation and spin wave modes of a confined magnetic state called an antivortex and the other looking at spin wave propagation in YIG using a thermal gradient. Both experiments center on using the BLS technique to measure spin wave dynamics in continuous and patterned thin films. The results of these projects suggest a new method to generate short wavelength spin waves that are difficult to excite by traditional methods and show that it is possible to steer and slow down spin wave beams using modest thermal gradients, both of which are potentially useful for spin-wave-based logic devices.

1.3. OUTLINE OF THESIS

This thesis is organized as follows:

Chapter 2 gives a review of the fundamental concepts required to understand magnetism, magnetic materials, and the work presented in this thesis. We start with magnetic moments that form the basis of magnetism and work up to macroscopic magnetization that is simply the collection of many interacting magnetic moments that often occur in such large numbers that the magnetization can be treated in a semi-classical regime. Then the factors that determine the distribution of magnetization into domains and saturated states are discussed. We also discuss the origin of anisotropy of magnetic materials and its mathematical treatment. Here we move from a discussion of static magnetization into the territory of magnetization dynamics. The phenomenon of ferromagnetic resonance is described and the Kittel equation for determining the frequency of the resonance is provided. Lastly spin waves are introduced by the idea of breaking the symmetry of the uniform mode. An overview of the simultaneous solution to the equation of motion of the magnetization and Maxwell's equations that

provide the complete dispersion theory of spin waves is provided. The dispersion relations provide all the details necessary to understand and predict spin wave propagation and will be used throughout this thesis to understand the experimental results. This chapter provides solutions for thin films under arbitrary conditions including patterned and continuous thin films.

Chapter 3 presents several measurement techniques required to obtain the data presented in this thesis. A simple, working-knowledge type overview of MFM, VSM, FMR, SQUID, and MOKE are provided. A detailed introduction to the BLS experiment including the apparatus, necessary theory, and operational knowledge is provided. The main components of the BLS are presented, including a description of the most crucial component the tandem Fabry-Perot interferometer. An overview of the micro-BLS, used to measure the antivortex states, is also provided.

Chapter 4 presents a study of the high-frequency dynamics of a magnetic antivortex stabilized in a patterned microstructure. An antivortex is a magnetic state that has spin sweeping in from two directions and out in two directions with an out-of-plane core region in the middle. Due to the difficulty of stabilizing an antivortex, few studies of the dynamics have been performed despite of the fact that the AV dynamics may be highly useful for magnonics applications. The dynamic response of the antivortex to frequency sweeps and position scans made with the micro-BLS technique are discussed. Micromagnetic simulations were performed to help identify the character of each mode, standing or propagating, as well as to confirm the spatial profile of the modes. Both experiment and simulation reveal short wavelength modes that are generated by the antivortex and couple to propagating spin waves in the adjacent legs of the structure.

Chapter 5 presents a study of the possibility of controlling the propagation of a beam of spin waves using a non-uniform thermal profile. The ability to manipulate and control signals in spin wave based devices is highly desirable in the novel field of spintronics. Full dispersion surfaces for arbitrary angle of spin wave propagation with respect to the field were solved for the entire range of $4\pi M_S$ values achieved and were used to predict what should happen to a beam of spin waves as they travel into a progressively hotter region. An intricate diamond-shaped propagation pattern was observed that was modified when a thermal gradient was applied. It is shown that it is possible to steer and slow down spin wave beams by noticeable amounts even under application of only a modest thermal gradient (0.8 K/mm).

CHAPTER 2

REVIEW OF MAGNETISM AND MAGNETIC MATERIALS

2.1. MAGNETIC MOMENTS

At the most fundamental level, magnetism in materials arises from the presence of elementary magnetic moments. These consist of the spin and orbital magnetic moments of electrons and the spin moments of nucleons. In general, the magnetic moment operators ($\boldsymbol{\mu}_S$, $\boldsymbol{\mu}_L$, and $\boldsymbol{\mu}_J$) are related to the angular momentum operators (\mathbf{S} - spin, \mathbf{L} - angular, and \mathbf{J} - total) by

$$\boldsymbol{\mu}_S = -\gamma_S \hbar \mathbf{S} \quad (2.1)$$

$$\boldsymbol{\mu}_L = -\gamma_L \hbar \mathbf{L} \quad (2.2)$$

$$\boldsymbol{\mu}_J = -\gamma \hbar \mathbf{J} \quad (2.3)$$

using $\mathbf{J} = \mathbf{L} + \mathbf{S}$ where γ is the gyromagnetic ratio defined as

$$\gamma_i = \frac{g_i |q|}{2mc} \quad (2.4)$$

where $i = (S, L, \text{ or } J)$, the eigenvalues of the angular momentum operators, and g_i is the spectroscopic splitting factor given by

$$g_S \approx 2 \quad (2.5)$$

$$g_L \approx 1 \quad (2.6)$$

$$g_J = \frac{3}{2} + \frac{S(S+1) - L(L+1)}{2J(J+1)} \quad (2.7)$$

using Hund's rules [8] and the Russell-Saunders coupling scheme approximation [9]. In practice, the gyromagnetic ratio is a complicated quantity that depends on the interaction between spin and orbital moments and is usually determined experimentally. Thus, for spins, $|\gamma_S/2\pi| = 2.8 \text{ MHz/G}$. These equations and all that follow are given in the CGS system. A comprehensive chart for converting between the CGS and SI unit systems is given in Table A.1 of Ref. [10].

If a particle with a magnetic moment is placed in a magnetic field, \mathbf{B} , the particle will experience a torque given by

$$\boldsymbol{\tau} = \boldsymbol{\mu} \times \mathbf{B}. \quad (2.8)$$

where the magnetic moment $\boldsymbol{\mu}$ is the total magnetic moment of the particle. Both the angular momentum and the magnetic moment are quantized in terms of the reduced Planck constant \hbar . The magnetic moment of the spin moment of one electron is approximately equal to one Bohr magneton, which is given by $\mu_B = \hbar q_e / 2m_e = 9.274 \times 10^{-24} \text{ J/T}$ for an electron where q_e is the magnitude of the elementary charge of an electron and m_e is the mass of an electron. Although there are many subatomic particles that may exhibit magnetic moments, in this work I focus on macroscopic magnetic materials that contain only protons, neutrons, and electrons. Furthermore, the magnetic moments of both protons and neutrons are dwarfed by that of electrons. Thus for practical purposes, materials that we commonly refer to as magnetic materials possess a magnetic moment due to the presence of unpaired electrons with a preferred spin direction.

When introduced to a magnetic field, a magnetic moment has a potential energy, called the Zeeman energy given by [5] $E_{Zeeman} = -\boldsymbol{\mu} \cdot \mathbf{B}$, which depends on the orientation of the moment with respect to the field. The Zeeman energy is minimized when the moment

is parallel/antiparallel to the field direction. If a single magnetic moment is perturbed from equilibrium, by a thermal excitation for example, the field will then exert a torque on the moment given in equation 2.8 that will cause it to precess around the field direction. This process is called Larmor precession and is the basis for dynamic processes in magnetic materials.

The macroscopic magnetic moment of a material is simply the sum of all the individual magnetic moments in a given volume following the rules of quantum mechanics for the addition of angular momenta. In order to understand the properties of magnetic materials, it is helpful to distinguish them by how their individual moments contribute to their macroscopic magnetization. A useful flow chart is shown in Fig. 2.1. Any materials that do not possess an atomic magnetic moment can immediately be identified as diamagnetic. Diamagnetic materials have an induced magnetic moment that arises from the modification of the orbits of the electrons in the presence or absence of an applied magnetic field, where the electrons act to counter the change in magnetic flux. Materials with permanent moments can be further characterized based on the presence or absence of long range order (alignment of the moments through the exchange interaction) at room temperature. Materials with no long range order (no exchange coupling between moments), called paramagnets, have magnetic moments that interact so weakly that long range order is destroyed by even a small amount of thermal energy. Paramagnets only exhibit a significant macroscopic moment when there is a strong enough magnetic field to align the moments. Materials that do exhibit long range order can be divided into two categories: those with neighboring moments that tend to align either parallel or antiparallel due to their quantum mechanical exchange coupling, known as ferromagnets and ferrimagnets, respectively. Ferromagnets tend to have a stronger

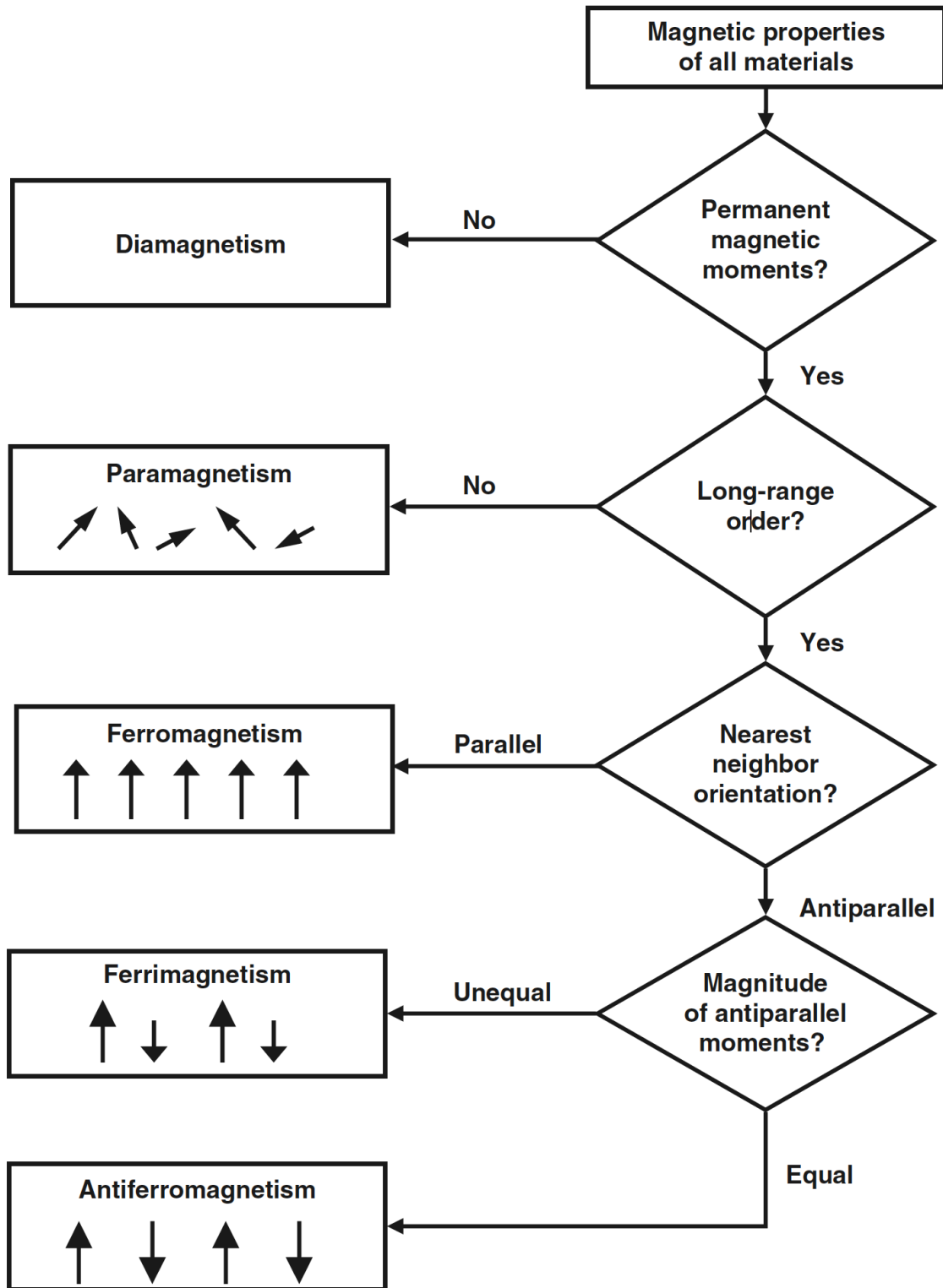


FIGURE 2.1. Flow chart to classify materials by their magnetic properties. Reproduced from [6] with permission from Springer.

permanent magnetization than ferrimagnets but both typically have a measurable remanent magnetization. For a ferrimagnet, in the limiting case that the neighboring moments are equal and opposite in magnitude the material is called an antiferromagnet and the net moment is zero. This thesis will treat both ferromagnets and ferrimagnets. Since they both have nonzero magnetization both can and will be treated as ferromagnets. Further discussion of the types of magnetic materials can be found in Ref. [6].

2.2. MAGNETOSTATIC ENERGIES

In addition to the Zeeman energy mentioned above, there are several different energies that influence both the static and dynamic properties of ferromagnetic materials including the exchange, dipole-dipole, and anisotropy energies. The concept of magnetic anisotropy is discussed in a later section.

Each dipole moment in a magnetic material generates a magnetic field that is felt by the other moments in the material. The superposition of all the dipole fields into one effective magnetic field is referred to as the demagnetization field. The energy associated with this long range interaction between moments is called the dipole-dipole or demagnetization energy. The total demagnetization energy for one dipole is found by summing the energy of that dipole in the fields generated by each of the other dipoles in the material [10]

$$E_{dipole-dipole} = (\gamma\hbar)^2 \sum_{i \neq j}^N \left[\frac{\boldsymbol{\mu}_i \cdot \boldsymbol{\mu}_j}{r_{ij}^3} - \frac{3(\boldsymbol{\mu}_i \cdot \mathbf{r}_{ij})(\boldsymbol{\mu}_j \cdot \mathbf{r}_{ij})}{r_{ij}^5} \right]. \quad (2.9)$$

The exchange energy is the result of a quantum mechanical interaction between nearest neighbor spins and leads to short range interactions. The exchange energy in a chain of N

spins is given as

$$E_{exchange} = -2J \sum_{i=1}^N \mathbf{S}_i \cdot \mathbf{S}_{i+1} \quad (2.10)$$

where J is the exchange integral. J is positive for ferromagnets which means that the exchange energy is minimized when nearest neighbors spin are aligned parallel. J is negative for ferrimagnets and antiferromagnets so their nearest neighbor spins will be aligned antiparallel.

2.3. DOMAINS AND SATURATION

The magnetic moments of ferromagnets have two main and often competing mechanisms of interaction that operate on two distinct length scales. Nearest neighbor interactions are dominated by exchange interactions that lead to parallel neighboring spins in a ferromagnet. Over a longer range the dipole-dipole interaction becomes significant. In order to reduce the demagnetization energy, domains - regions of locally uniform magnetization - form. These domains also reduce the total magnetic moment of the magnet. Domains also play an important role in the reversal process of a magnetic material. A typical magnetization vs. field curve, also known as a hysteresis loop, is shown in Fig. 2.2. When a static magnetic field is applied, the domains oriented parallel to the field are favored energetically and become larger in size. After a strong enough field is reached, known as the saturating field, the domains oriented in other directions are eliminated in favor of one single domain and all the moments are parallel to the field. This is called the saturated state and it is associated with the maximum magnetization, M_S , the magnet can attain. If the field is removed, domains oriented in other directions will again form and start to grow as the field is changed (decreased and then increased in the opposite direction). At zero field there will generally be

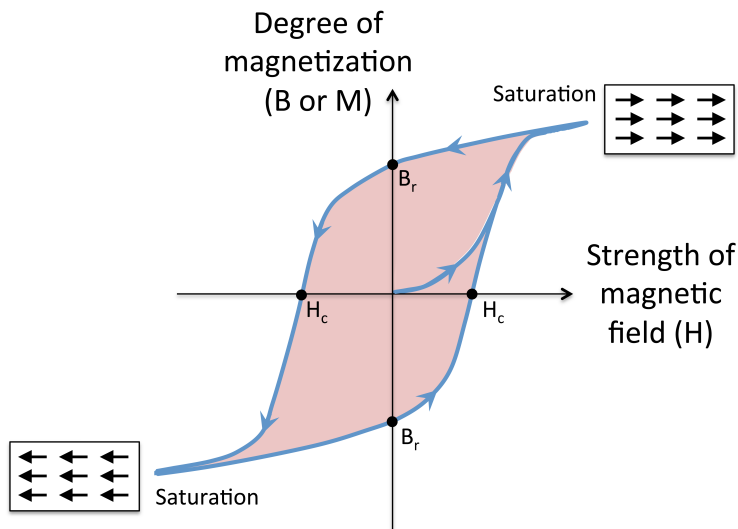


FIGURE 2.2. Hysteresis loop of a ferromagnet [11].

a significant saturation magnetization, called the remanent magnetic field B_r or remanent moment M_r . If the field is then increased in the negative direction, the magnetization will eventually drop to zero and become negative as the domains adjust. The field needed to obtain zero magnetization is known as the coercive field H_c . At larger negative fields, the domains oriented parallel to the field will grow until there again is one single domain parallel to the field that is again the saturated state. This process is called magnetic hysteresis since the magnetic state of a ferromagnet will, in general, depend on the history of field exposure. For any kind of magnetic measurement, including dynamic measurements, it is important to pay attention not just to the applied field but also to the field history for measurements made below saturation. Techniques used to measure hysteresis loops will be discussed in Section 3.3. The width of a ferromagnet hysteresis loop is determined by the magnitude of the coercive field. Materials with a small coercive field (or coercivity) are easily switched and thus are called soft ferromagnets. Materials with a high coercivity require a large field to be switched and are referred to as hard ferromagnets.

2.4. MAGNETIC ANISOTROPY

While it is possible to have an isotropic ferromagnet that exhibits hysteresis curves that are independent of the applied field direction, it is common to have differences in shape of the hysteresis loop depending on the angle of the applied field with respect to the crystal lattice and the sample geometry, which occurs due to the presence of magnetic anisotropy. Anisotropy occurs when the energy depends on the orientation of the magnetization with respect to the crystal lattice. Anisotropy can also come about due to the structural geometry of the sample, which is called the shape anisotropy. Shape anisotropy becomes more significant as the size of the sample is constrained in one or more dimensions. In this case the moments near the boundary will act to reduce the demagnetization energy on the boundary by orienting themselves parallel to the constrained boundary. In thin films, the focus of study in the projects presented in this thesis, this is an important factor because it is much easier to saturate the sample within the plane of the thin film than out of the plane. Anisotropy is not only an important consideration for the static magnetization but has pronounced effects on the magnetization dynamics.

2.5. MAGNETIZATION DYNAMICS

2.5.1. EQUATION OF MOTION. So far we have considered ferromagnets with a static magnetization. Now we will look at dynamic processes in ferromagnets. Our goal is to find the magnetization as a function of time as described by the equation of motion given as

$$\frac{d\mathbf{M}}{dt} = -\gamma \mathbf{M} \times \mathbf{H} \quad (2.11)$$

where γ is the gyromagnetic ratio. When combined with Maxwell's equations [5] and appropriate boundary conditions, the equation of motion can be used to solve for M vs t , or for dispersion relations. Equation 2.11 does not account for any intrinsic sources of damping and as such damping must be incorporated phenomenologically. There are two common methods to account for damping, the method presented by Landau and Lifshitz [12]

$$\frac{d\mathbf{M}}{dt} = -\gamma(\mathbf{M} \times \mathbf{H}_{eff}) + \frac{\lambda\gamma}{M_S^2}\mathbf{M} \times (\mathbf{M} \times \mathbf{H}_{eff}), \quad (2.12)$$

where λ is the damping parameter, and the method presented by Gilbert [13]

$$\frac{d\mathbf{M}}{dt} = -\gamma\mu_0(\mathbf{M} \times \mathbf{H}_{eff}) + \frac{\alpha}{M_S} \left(\mathbf{M} \times \frac{d\mathbf{M}}{dt} \right). \quad (2.13)$$

where α is the damping parameter and where H_{eff} is the effective field that may include contributions from the demagnetization and anisotropy and is given by

$$\mathbf{H}_{eff} = \mathbf{H}_{ext} + \mathbf{H}_{ex} + \mathbf{H}_{dem} + \mathbf{H}_{ani}. \quad (2.14)$$

In the expression above, \mathbf{H}_{ext} is the external magnetic field, \mathbf{H}_{dem} is the demagnetization field given by

$$\mathbf{H}_{dem} = -N_d\mathbf{M}, \quad (2.15)$$

\mathbf{H}_{ani} is the anisotropy field

$$\mathbf{H}_{ani} = -\frac{1}{M} \nabla_M E_{ani}, \quad (2.16)$$

and \mathbf{H}_{ex} is the exchange field

$$\mathbf{H}_{ex} = \lambda_{ex} \nabla^2 \mathbf{M} \quad (2.17)$$

where N_d is the demagnetization tensor, λ_{ex} is the exchange length, and E_{ani} is the anisotropy energy the exact form of which depends on the symmetry of the anisotropy. In many spin wave studies, the sample is saturated before oscillations are excited. In this state the damping will compensate thermal fluctuations and the magnetization will sit at equilibrium along the direction of the effective field. In experiments the precession is driven through use of a dynamic magnetic field. In the linear response regime the dynamic magnetization deviates only slightly from the saturation direction. As a result, a small angle approximation may be used to linearize the equation of motion. Taking the $+\hat{z}$ direction along the direction of the static magnetization, we can write the total magnetization as the sum of the static and dynamic contributions

$$\mathbf{M}(t) = M_z \hat{z} + \mathbf{m}(x, y, t) \quad (2.18)$$

where $|\mathbf{m}| \ll M_z$. Substituting this back into equation 2.11, we can solve for the dynamic components only

$$\frac{d\mathbf{m}}{dt} = \gamma \mathbf{m} \times \mathbf{H}, \quad (2.19)$$

which is the torque equation for the dynamic component of the magnetization. This approximation can be used to treat uniform as well as non-uniform spin excitations.

2.5.2. UNIFORM PRECESSION. If a ferromagnet is saturated in a single domain state and a field is applied, all of the spins will precess around the direction of the effective field. A free spin will precess around an external field, which is called Larmor precession, whereas for a spin in a ferromagnetic material, the precession frequency will depend on the effective field that includes not only the external field but also contributions from the magnet itself such as the demagnetization field and anisotropy as given in equation 2.14. This precession

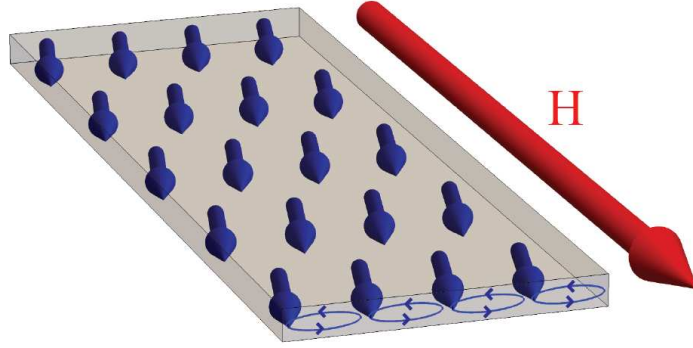


FIGURE 2.3. Illustration of a ferromagnetic sample undergoing uniform precession. The precession is generally elliptical in thin films due to the shape anisotropy.

is called ferromagnetic resonance (FMR). All the moments in the sample precess in-phase and the mode is uniform with infinite wavelength. This precession occurs at a frequency given by the Kittel resonance condition [14] as

$$\omega = \sqrt{[\omega_H + (N_y - N_x)\omega_M] [\omega_H + (N_z - N_x)\omega_M]}, \quad (2.20)$$

where γ is the gyromagnetic ratio, (N_x, N_y, N_z) are demagnetizing factors that depend on the shape of the magnetic sample, $\omega_H = \gamma H$, and $\omega_M = \gamma 4\pi M_S$. Here H is the external field and the equation assumes that the only anisotropy is due to the shape of the sample. For a given applied field there is a specific frequency at which all the spins in the sample precess around the field in phase in the so-called FMR mode, which is illustrated in Fig. 2.3. This mode can be driven by applying an oscillating (or dynamic) magnetic field perpendicular to the static magnetization at the required frequency or it can be excited by a short pulse. Due to damping, if the dynamic field is removed, the magnetization will undergo relaxation processes that transfer the angular momentum to the crystal lattice until it is back in the equilibrium state - parallel to the static field.

For an extended thin film magnetized out-of-plane the resonance condition 2.20 reduces to a simpler form

$$\omega = \omega_H - \omega_M \tag{2.21}$$

where $\omega_H > \omega_M$. For in-plane magnetized films the resonance condition is

$$\omega = \sqrt{\omega_H(\omega_H + \omega_M)}. \tag{2.22}$$

The equations give a simple approximation to quickly evaluate the frequency of the uniform mode in thin film applications.

2.6. SPIN WAVES

Now that we have explored the mode of uniform precession, we will take a look at the non-uniform excitations that are allowed to exist in magnetic materials. In this thesis, “spin wave” will be used as the general term to describe all non-uniform excitations of the spin system that can propagate. This includes excitations historically classified as magnetostatic waves, dipolar spin waves, and exchange spin waves depending on the magnitude of the wavenumber. A spin wave is simply illustrated by a chain of neighboring moments as shown in Fig. 2.4. All the moments in this chain precess around the local field direction at the same frequency and cone angle but have a constant phase difference between them. The wavelength of a spin wave is defined as the distance over which the difference in phase is equal to 2π radians and is related to the wavenumber in the usual way $\lambda = 2\pi/k$. As with excitations in all physical systems, spin waves are quantized and the quasi-particle associated with the quantization is called a magnon. The theory of spin waves can be developed from a quantum perspective. A full derivation can be found in Section 7.4 of Ref. [10], for instance.

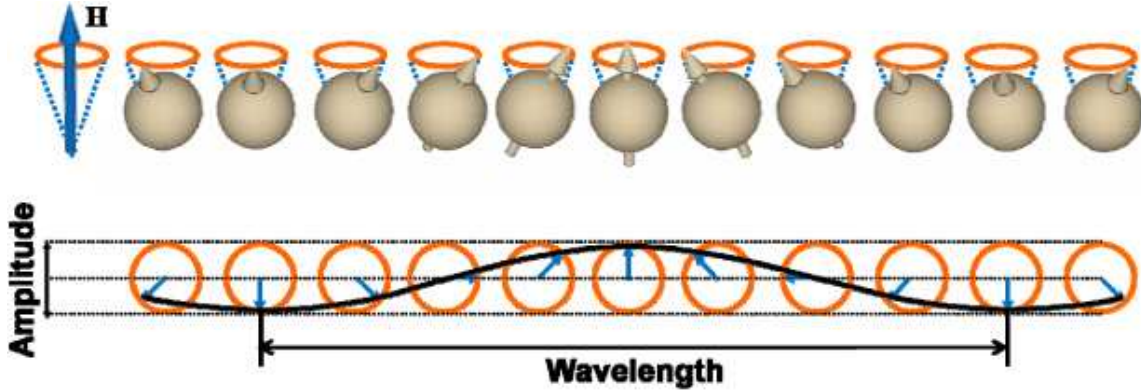


FIGURE 2.4. Diagram of a spin wave demonstrated on a chain of moments where subsequent moments have a constant difference in the phase of their precession. The yellow magnetic moments can represent individual atomic moments or the average moments of macroscopic regions [15] reproduced with permission from IOP Publishing.

An important aspect of the quantum view that is relevant to this work is that the energy and momentum of a magnon are given by $\hbar\omega$ and $\hbar\mathbf{k}$ respectively. Spin waves exhibit all the properties of waves including propagation, interference, reflection, and refraction. This thesis will focus on spin waves in thin films.

2.7. SPIN WAVE MODES

Spin waves are typically discussed as plane waves that are classified by the orientation of their wavevector relative to the direction of the saturation magnetization M_S . Spin waves may propagate at any arbitrary direction with respect to the magnetization and can be thought of as linear combinations of plane waves. Spin waves that propagate in the plane of the film that are saturated with an out of plane field are known as forward volume spin waves (FVSW). If the magnet is saturated parallel to the plane, spin waves that travel in the plane and parallel to the magnetization are called backward volume spin waves (BVSW) and surface spin waves (SSW) if they travel perpendicular to the magnetization. SSWs are also commonly referred to as Damon-Eshbach (DE) spin waves after the authors of Ref.

[16]. It is also possible to excite standing spin wave resonances across the thickness that are called the perpendicular standing spin wave (PSSW) modes. In thin films the component of the wavevector along the thickness is quantized as $k_n = n\pi/t$ where t is the film thickness and $n = 1, 2, 3\dots$. In out-of-plane magnetized films, the FVSW do not have a preferred propagation direction. They have a standing wave profile across the thickness and in-plane wavevector k_{\parallel} . The group and phase velocities for FVSWs are parallel to each other. These modes are discussed in further detail in Section 2.8.4 and shown in Fig. 2.11. The dispersion relations, described in the next section, are different for each of these configurations, which leads to different propagation characteristics.

2.8. DISPERSION THEORY

Dispersion relations relate the energy ($\hbar\omega$) and momentum ($\hbar\mathbf{k}$) of a wave and are a powerful tool in spin wave research. The most obvious function is to predict the frequency over a range of possible wavevectors given the experimental conditions and material parameters. In addition to this, they can be used to find the phase and group velocity and hence to determine the speed and direction of energy propagation spin waves. If the material parameters are not completely known, the dispersion relations can also be used to fit experimental data, such as the spin wave frequency measured for a spin wave with known wavevector, to extract the parameters of interest. Because the equation of state for the macroscopic magnetization is nonlinear, solving for the dispersion relations is a non-trivial task. There is an extended history of different approaches that have been used to solve the dispersion relations for ferromagnetic materials. Here we present two mathematical approaches based on the continuum model for magnetization dynamics and that allow for the determination of the dispersion relations up to arbitrary precision. One is the partial wave (PW) method

and the other is the spin wave mode (SWM) method. Both methods provide a solution for spin waves in an extended thin film geometry. Aside from the different forms assumed for the solutions, the two approaches lead to identical results, as would be expected. In this section, I will provide a brief walkthrough of the steps required to obtain the dispersion relations following both methods. An example script for computing the dispersion relations under arbitrary conditions using the SWM approach is presented and discussed in B.

2.8.1. PARTIAL WAVE (PW) METHOD. The central idea behind the partial wave method is to assume the dynamic magnetization can be written as a linear combination of plane waves, plug the assumed solutions into Maxwell's equations and apply appropriate boundary conditions. This method was first established by Rado and Wertman [17] but a very understandable presentation was provided in Ref. [18] for multilayers, which also applies to single layer films. The first step is to start with the full equation of motion, usually the LLG equation, including the Zeeman, dipole, and exchange interactions. Now apply Maxwell's equations to obtain the boundary conditions on H and B (and therefore M), which are that $H_{\parallel inside} = H_{\parallel outside}$ and $B_{\perp inside} = B_{\perp outside}$ where the subscripts indicate the orientation and location of the fields with respect to the bottom and top surfaces of the extended thin film. In the case of multilayer structures, two additional boundary conditions arise: Rado-Wertman conditions if there is no exchange coupling across the boundary [17] or the Hoffman conditions if the layers are exchange coupled [19]. Now we linearize the equation of motion assuming the dynamic components of the field and magnetization are small, i.e., $|\mathbf{m}| \ll |\mathbf{M}|$ and $|\mathbf{h}| \ll |\mathbf{H}|$. Next we assume a plane wave form for the dynamic components inside the film, \mathbf{h} and \mathbf{m} proportional to $\exp[i(\omega t - \mathbf{Q} \cdot \mathbf{R})]$. Where \mathbf{Q} is the total wavevector and \mathbf{R} is the position vector. Inserting this form into the linearized equation of

motion and the boundary conditions we arrive at a matrix whose elements depend on \mathbf{Q} and are the coefficients of the components of \mathbf{h} and \mathbf{m} . The determinant of the matrix must vanish providing the dispersion relation. The matrix can also be found in terms of the elements of \mathbf{h} and \mathbf{m} at the boundaries. In this case the elements of \mathbf{m} can be written as elements of \mathbf{h} to obtain a matrix whose coefficients are all components of \mathbf{h} at the boundaries. The determinant again must vanish resulting in the dispersion relation.

2.8.2. SPIN WAVE MODE (SWM) METHOD. The SWM method is based on a complete set of vector functions that satisfy the exchange boundary conditions (given in equation 10 of Ref. [20]). In this case a vanishing infinite determinant provides the solution to the dispersion relations. One advantage of this method is that it provides approximate solutions that don't have dispersion properties hidden in transcendental equations as is the case with the PW method [21]. Instead the approximate forms give an intuitive dependence of the frequency on many parameters including wavevector, angle of propagation with respect to the field, and the effects of exchange and anisotropy. Foundational work for this method was first established by [22] and a very comprehensive reference has been given by Kalinikos [20, 21] that will be followed here.

In the first step, the dynamic magnetization is assumed to be proportional to $\exp[i(\omega t - k_\zeta \zeta)]$ where k_ζ is the in-plane wavenumber and ζ is a coordinate along which the spin wave propagates. Next the dipole field is written in terms of the variable magnetization using a tensorial Green function. This form of the dipole field is inserted into the linearized equation of motion for magnetization, the linearized Landau-Lifshitz equation. This leads to an integro-differential equation that describes the Fourier amplitude of the spin wave. This one equation is the equivalent of Maxwell's equations, the boundary conditions, and

the equation of motion and solving it provides the full spectrum of dipole-exchange spin waves. Kalinikos solved it by using the eigenfunctions of the exchange operator as normal modes [20]. Physically these eigenfunctions are found to be perpendicular standing spin wave (PSSW) modes that are quantized by the thickness. Hereafter, I will refer to these PSSW eigenfunctions as thickness modes. This process is neither straightforward nor intuitive but the results are very useful for analyzing propagating spin waves.

In this section, I will “walk” the reader through the list of equations needed to numerically calculate the dispersion relations. The problem is usually presented in the following way. Every antenna has a certain range of wavevectors it can efficiently excite. This range is approximately determined by taking the Fourier transform of the dynamic field across the width of the antenna. A more exact solution incorporates an additional surface current generated in the antenna by the fluctuating magnetization beneath but this level of precision is not typically required. Knowing this range, the experimentalist can set H_{ext} and the orientation of the film with respect to the applied magnetic field and use these dispersion calculations to determine many features of the spin wave propagation including but not limited to the range of frequencies, the group velocities, and the presence of standing spin wave modes.

The first step in the calculation is to set up an array of in-plane wavenumbers (k_ζ, k_η) . The step size is determined by the user but has a large effect on computation speed so it is smart to start with large steps. The next step is to initialize the frequency arrays. For each thickness mode we can find a frequency for every combination of wavevectors, thus the total frequency array should have dimensions of [length(k_ζ range), length(k_η range), number of thickness modes]. Note that the thickness modes interact heavily when they are tightly

spaced (for thick films) thus the more thickness modes that are included, the more accurate the answer will be. The number of thickness modes also affects computation speed. Thus a rule of $n + 3$ modes is usually followed where n is the number of thickness modes that you actually want to study. Next the angles θ and ϕ are computed as defined in Fig. 2.5. The trigonometric coefficients A - E (equations 28-32 in [20]) can then be found

$$A = \cos^2 \phi - \sin^2 \theta (1 + \cos^2 \phi) \quad (2.23)$$

$$B = -\cos \phi \sin 2\theta \quad (2.24)$$

$$C = \cos \theta \sin \phi \cos \phi \quad (2.25)$$

$$D = -\sin \theta \sin \phi \quad (2.26)$$

$$E = \sin^2 \phi \quad (2.27)$$

Now we need to find the matrix \mathcal{L} that is composed of the block elements given by equation 34 in Ref. [20]. We see that the terms along the diagonal involve only a single thickness mode denoted by n . The off-diagonal elements describe the interaction of thickness modes n and n' . In this way, every thickness mode interacts with every other thickness mode and there are infinitely many modes. However, the interaction of thickness modes decreases drastically with the frequency spacing between the modes, i.e., the interactions between modes 4 and 9 is much less than between 8 and 9, hence the $n+3$ rule mentioned above. In the so called “zero-order approximation”, the modes are not allowed to interact and thus the frequency of each mode is simply equal to the determinant of the corresponding \hat{D}_{nn} matrix given below. In this case the thickness modes are degenerate at certain values of the wavenumber where the thickness modes cross. In the full calculation, where mode interaction

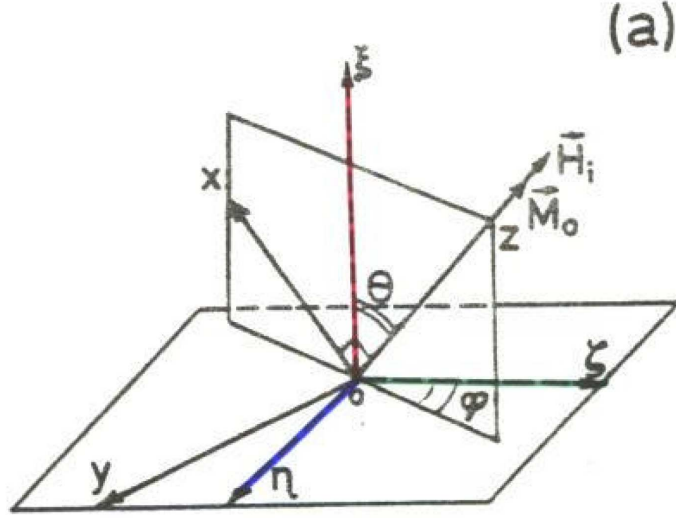


FIGURE 2.5. The geometry of the dispersion relation calculation given in personal communication with Kalinikos, B. A. [23]. Here the field $H_{eff} = H_i$ which lies at an angle θ from the normal to the surface of the film and at an angle ϕ from the direction of the spin wave wavevector k_ζ .

is permitted, the degeneracy is lifted and the modes never cross. In order to find \mathcal{L} we need to compute the \hat{D}_{nn} and $\hat{R}_{nn'}$ matrices. D is given in equation 23 as

$$\hat{D}_{nn} = \begin{bmatrix} [N_n^x + \sin^2 \theta + AP_{nn}^{xx}] & [CP_{nn}^{xy} - i(\frac{\omega}{\omega_M} T_{nn}^{xy} - DQ_{nn}^{xy})] \\ [CP_{nn}^{yx} + i(\frac{\omega}{\omega_M} T_{nn}^{yx} + DQ_{nn}^{yx})] & [N_n^y + EP_{nn}^{yy}] \end{bmatrix} \quad (2.28)$$

and the R matrix is given in equation 24 as

$$\hat{R}_{nn'} = \begin{bmatrix} [AP_{nn'}^{xx} + iBQ_{nn'}^{xx}] & [CP_{nn'}^{xy} - i(\frac{\omega}{\omega_M} T_{nn'}^{xy} - DQ_{nn'}^{xy})] \\ [CP_{nn'}^{yx} + i(\frac{\omega}{\omega_M} T_{nn'}^{yx} + DQ_{nn'}^{yx})] & [EP_{nn'}^{yy}]. \end{bmatrix} \quad (2.29)$$

Here we encounter many new parameters. First we have the pinning parameters that describe the pinning of the magnetization at the boundaries of the film thickness and depend critically surface anisotropy [20]. The pinning can be experimentally determined by a network

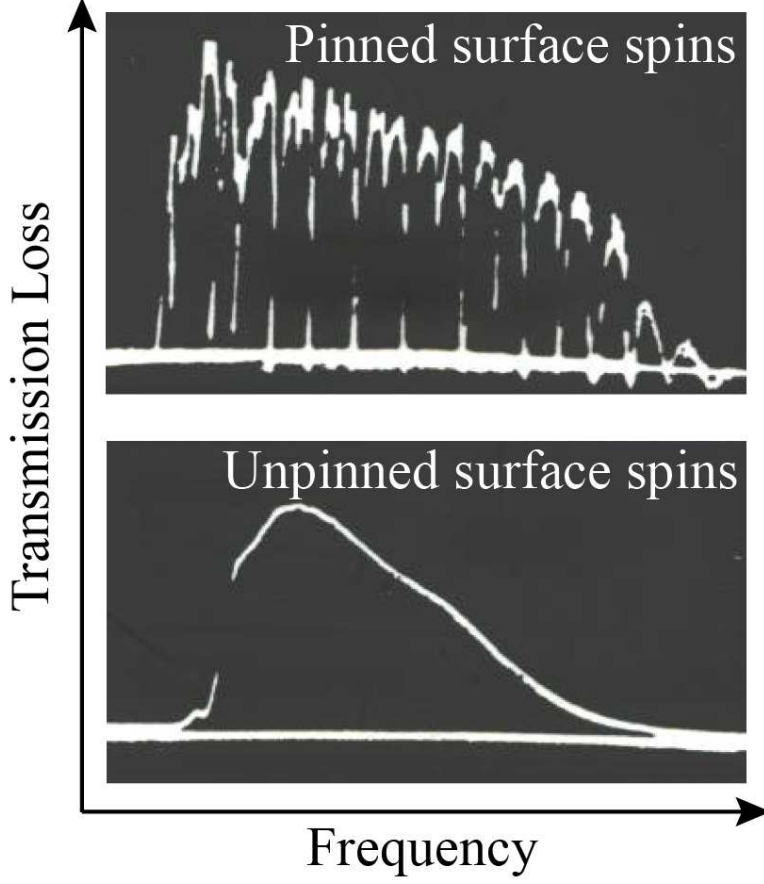


FIGURE 2.6. Experimental evidence of the effects of pinning on the transmission loss in a thin magnetic film. In the top plot the dips indicate pinning of the magnetization at frequencies where the perpendicular standing spin wave modes occur and energy is not transmitted through the film. The bottom plot shows that when the magnetization is not pinned frequencies of the entire range allowed by the input antenna are passed.

analyzer measurement where the amount of pinning is proportional to the depth of the dips in the transmission profile (S_{21}). Figure 2.6 shows characteristic insertion loss measurements for pinned and unpinned ferromagnetic films [23].

The parameters for pinned surface spins are provided in the appendix of Ref. [20] by equations A10 and A11 as

$$P_{nn'} = \frac{k_{\zeta}^2}{k_{n'}^2} \delta_{nn'} + \frac{k_{\zeta}^2}{k_n^2} \frac{K_n K_{n'}}{k_{n'}^2} F_n \left(\frac{1 + (-1)^{n+n'}}{2} \right) \quad (2.30)$$

$$Q_{nn'} = \frac{k_\zeta^2}{k_{n'}^2} \left(\frac{K_n K_n'}{K_{n'}^2 - K_n^2} \frac{2}{k_\zeta t} - \frac{k_\zeta^2}{2k_n^2} F_n \right) \left(\frac{1 + (-1)^{n+n'}}{2} \right). \quad (2.31)$$

The parameters for unpinned surface spins are give by equations A12 and A13 as

$$P_{nn'} = \frac{k_\zeta^2}{k_{n'}^2} \delta_{nn'} - \frac{k_\zeta^4}{k_n^2 k_{n'}^2} F_n \frac{1}{[(1 + \delta_{0n})(1 + \delta_{0n'})]^{1/2}} \left(\frac{1 + (-1)^{n+n'}}{2} \right) \quad (2.32)$$

$$Q_{nn'} = \frac{k_\zeta^2}{k_{n'}^2} \left(\frac{K_{n'}}{K_{n'}^2 - K_n^2} \frac{2}{k_\zeta t} - \frac{k_\zeta^2}{2k_n^2} F_n \right) \left(\frac{1 - (-1)^{n+n'}}{2} \right) [(1 + \delta_{n,0})(1 + \delta_{n',0})]^{-1/2} \quad (2.33)$$

where $Q_{nn'}$ for the unpinned case is taken from equation 34 of Ref. [24]. Here δ_{ij} represents the familiar Kronecker delta function having a value of 0 for $i \neq j$ and 1 for $i = j$. The term containing the delta functions seems to have been dropped in Refs. [21, 20] but arises from the orthonormality of the eigenfunctions Φ_n^p present in the double integral definition of $Q_{nn'}$ in equation 26 of Ref. [20].

Now we have the T parameter given in equation 27 as

$$T_{nn'}^{pp'} = T_{n'n}^{p'p} = \frac{1}{t} \int_{-t/2}^{t/2} \Phi_n^p(\xi) \Phi_{n'}^{p'}(\xi) d\xi \quad (2.34)$$

but by symmetry arguments it can be shown that $T = 1$ for $n = n'$ and $T = 0$ for $n \neq n'$.

Finally we have that F is given by equation A14 as

$$F_n = \frac{2}{k_\zeta t} [1 - (-1)^n e^{-k_\zeta t}] \quad (2.35)$$

where t is the film thickness, k_ζ is the in-plane spin wave wavenumber defined to be along the propagation direction, K_n is the out-of-plane wavenumber quantized as $n\pi/t$, and k_n is the total wavenumber given by $\sqrt{k_\zeta^2 + K_n^2}$. The allowed thickness modes are determined by

the surface pinning conditions with $n = 0, 1, 2, \dots$ for unpinned surface spins and $n = 1, 2, 3, \dots$ for pinned surface spins.

2.8.3. NATURE OF SOLUTIONS. The dispersion relations allow for arbitrary directions of the magnetization and wavevector with respect to the ferromagnetic sample. In practice the direction of the wavevector is determined by the excitation geometry and the dispersion relations can be used to calculate the expected frequency. However, many antenna structures excite a range of wavevectors and often excite wavevectors in more than one direction. One of the uses of dispersion curves is to evaluate the expected wavevectors and group velocities of spin waves that are generated using a microstrip antenna. A characteristic set of dispersion surfaces, or spin wave manifold [6], with each surface corresponding to a thickness mode is shown in 2.7. Cuts of the dispersion surfaces along the $k_x = 0$ and $k_y = 0$ axes provide the dispersion curves of pure BV and DE spin wave modes as shown in Fig. 2.8, for instance. A given pumping frequency will slice through the surfaces providing the range of wavevectors that can be excited. These cuts are called slowness curves, where the slowness is defined as the inverse of the group velocity (and also depends on the wavevector and frequency), and they will be discussed in more detail in Chapter 5. The group velocity of a given spin wave is given by $\mathbf{v}_g = \nabla_{\mathbf{k}}\omega$ and the phase velocity is $\mathbf{v}_p = \omega\mathbf{k}/k^2$. Thus each component of the velocities is a set of surfaces in k space.

The dispersion relations described above are for continuous thin films. By construction, these solutions all have a quantized wavevector across the thickness of the film given by $K_n = n\pi/t$ where n is the thickness mode number and depends on the pinning conditions at the boundary. A sample is considered unpinned if the surface spins are free to precess at the boundary and pinned if the precession of the surface spins is constricted. These

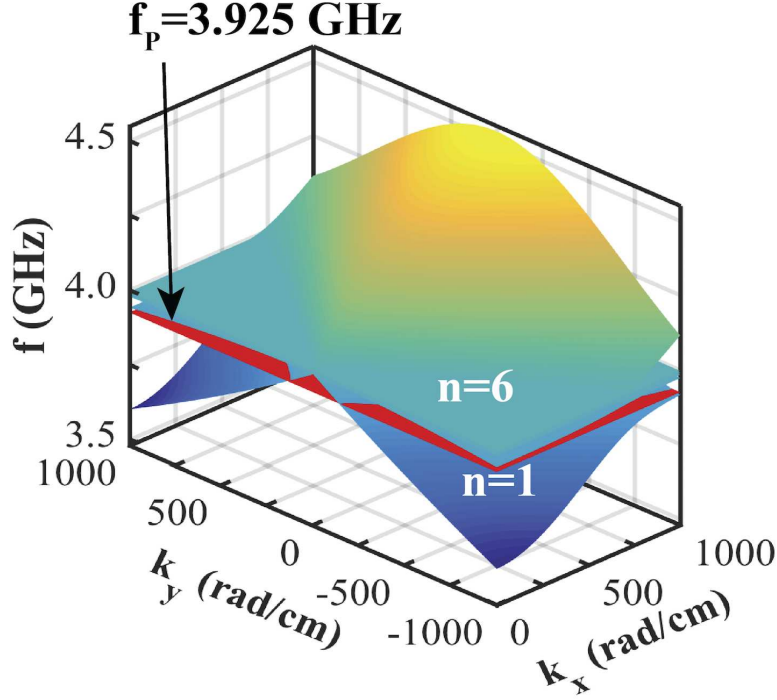


FIGURE 2.7. A characteristic dispersion manifold for a thin continuous film with in-plane magnetization saturated along the y-axis. Calculated for an 6.3 μm thick YIG film with $H = 779$ Oe and $4\pi M_S = 1821$ G and unpinned surface spins. The red plane indicates a pumping frequency of $f_p = 3.925$ GHz.

so-called perpendicular standing spin waves (PSSW) are formed when spin waves having equal and opposite wavenumbers in the thickness direction interfere constructively. The magnetization precession amplitude has an sinusoidal dependence on the thickness as shown in right two modes in Fig. 2.10. The PSSW resonances are flat planes that cross through the dispersion manifold above the FMR mode. In actuality, the modes are non-degenerate so a hybridization of the modes must occur to lift the degeneracy. The gaps between the hybridized modes are called “dipole gaps” [20]. Mode hybridization leads to large changes to group velocity and propagation angles in near the SSW/PSSW crossing points. An example of the crossing points is shown in Fig. 2.9.

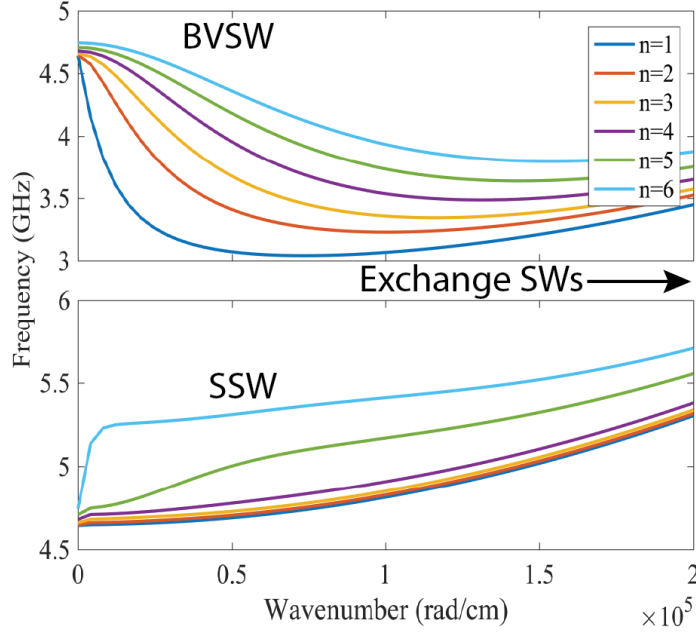


FIGURE 2.8. Characteristic dispersion curves for a thin continuous film in both the BV (low frequencies) and DE (high frequencies) configurations. The first six PSSW modes are shown. These dispersion curves were calculated for an 2 μm thick YIG film with $H = 1000$ Oe and $4\pi M_S = 1750$ G and unpinned surface spins.

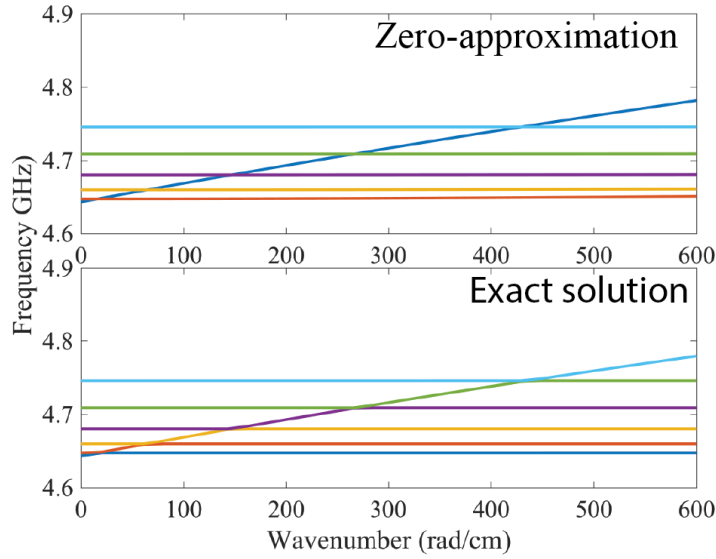


FIGURE 2.9. PSSW surfaces cut through the propagation surface wave. The zero-approximation (top) is computationally efficient but allows degeneracy between spin wave modes. The full theory lifts the degeneracy and never lets modes cross. Instead, the modes bend sharply near the resonances leading to dipole gaps. These dispersion curves were calculated for an 2 μm thick YIG film with $H = 1000$ Oe and $4\pi M_S = 1750$ G and unpinned surface spins.

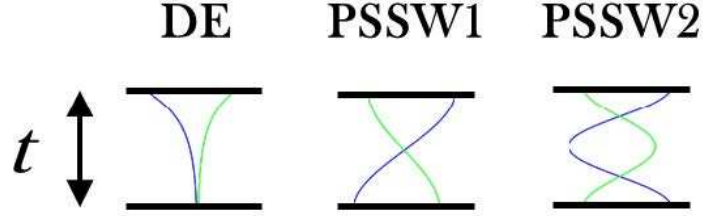


FIGURE 2.10. The profile of the dynamic magnetization across the film thickness for DE and PSSW modes shown for unpinned surface spins. The black lines represent the boundaries of the film while the green and blue curves illustrate the amplitudes of the dynamic component of the magnetization for upward and downward traveling waves that superpose to form standing waves.

2.8.4. LIMITING CASES. There are a few types of thin film spin wave solutions that are useful to highlight. These correspond to geometries of high symmetry that can be chosen experimentally by the orientation of a microstrip antenna with respect to the external field. Two orientations of the static magnetization are considered: parallel to the plane of the sample (tangentially magnetized) and perpendicular to the plane of the sample (normally magnetized). Figure 2.11 shows the dispersion curves for the two limiting cases for a tangentially magnetized sample and also for a normally magnetized sample. For a tangentially magnetized film, when the wavevector is oriented parallel to the static magnetization, as illustrated in the bottom inset of Fig. 2.11, the spin waves are referred to as magnetostatic backward volume spin waves (BVSW). The volume character of these modes arises from the fact that they form standing waves across the thickness of the film and thus a majority of the precession amplitude lies within the bulk of the film. The group and phase velocities are in opposite directions for small wavevectors, which occurs due to magnetostatic field effects. Because of the opposing group and phase velocity directions, this is referred to as a backward wave. The second case is where the wavevector is perpendicular to the static magnetization

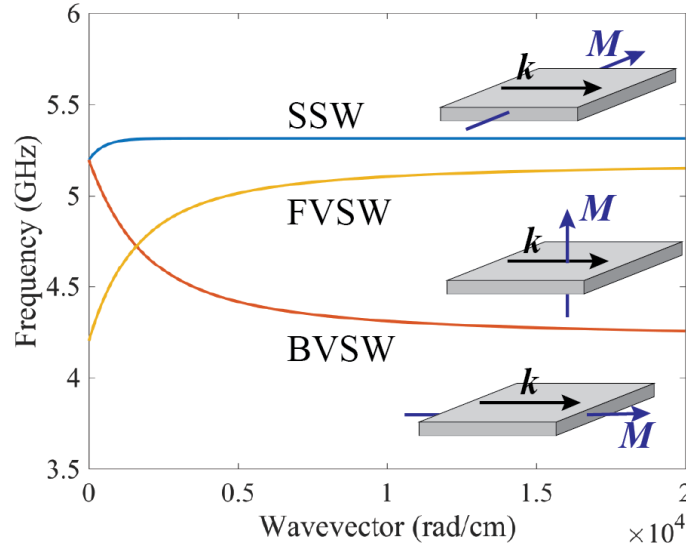


FIGURE 2.11. The first order thickness mode dispersion relation for the three commonly used excitation geometries.

vector as illustrated in the top inset of Fig. 2.11. These spin waves are referred to as magnetostatic surface spin waves (SSW). The surface wave character comes from the fact that the precession amplitude is highest on the surfaces of the film and decays exponentially with the thickness. These solutions are also non-reciprocal in the sense that the mode with one direction of group velocity will be localized on one surface of the film while the mode with the opposite group velocity is localized on the other side as illustrated by the left diagram in Fig. 2.10. The field direction and antenna placement must be chosen carefully for SSWs to ensure that the wave propagates along the desired surface.

In a normally magnetized sample there is just one limiting case, referred to as the magnetostatic forward volume spin wave (FVSW). Like the BVSW case, these wave solutions form a standing wave across the thickness of the film and, consequently, have a volume wave character. Here the wave propagates parallel to the plane of the film as illustrated in the middle inset of Fig. 2.11 but the dispersion characteristics are the same for any direction of

the in plane wavevector. The group and phase velocities of FVSWs are both positive and point in the same direction.

The approximate dispersion relations have convenient analytical solutions for the three limiting cases discussed above. The dispersion relation for out-of-plane magnetization is

$$\omega_{FVSW}^2 = (\omega_H - \omega_M + \alpha\omega_M k_n^2)(\omega_H - \omega_M + \alpha\omega_M k_n^2 + \omega_M P_n). \quad (2.36)$$

The dispersion relation for in-plane magnetization is

$$\omega_{in-plane}^2 = (\omega_H + \omega_M + \alpha\omega_M k_n^2 - \omega_M P_n)(\omega_H + \alpha\omega_M k_n^2 + \omega_M P_n \sin^2 \theta) \quad (2.37)$$

where $k_n^2 = k_\zeta^2 + K_n^2$, α is the exchange parameter, and θ is the angle between the wavevector and the static magnetization (specifically $\theta = 0$ for BVSW and $\theta = \pi/2$ for SSW). Recall that k_ζ is the in-plane wavenumber and K_n is the out-of-plane quantized wavenumber. The pinning parameter for unpinned surface spins is given by

$$P_n = \frac{k_\zeta^2}{k_n^2} - \frac{2k_\zeta^4}{k_\zeta t k_n^4} \left(\frac{1}{1 + \delta_{0n}} \right) [1 - (-1)^n e^{-k_\zeta t}] \quad (2.38)$$

where $n = 0, 1, 2, 3, \dots$ The pinning parameter for pinned surface spins is given by

$$P_n = \frac{k_\zeta^2}{k_n^2} + \frac{2k_\zeta^2 K_n^2}{k_\zeta t k_n^4} [1 - (-1)^n e^{-k_\zeta t}]. \quad (2.39)$$

where $n = 1, 2, 3, \dots$ These equations are highly useful for a quick calculation of the dispersion for spin waves excited in one of the three limiting geometries. They also give an explicit dependence on parameters that allows one to get a feel for how each parameter can affect the calculated frequency.

2.9. CONCLUSIONS

The origin of macroscopic magnetization and types of magnetic materials were presented. An overview of several common approaches used to find dispersion curves was provided. In all cases, the theory is based on a solution of the equation of motion and Maxwell's equations. Several characteristic modes of spin wave dynamics were presented including uniform (FMR) and non-uniform propagating (spin wave) modes. The dispersion relations presented in this chapter are for extended thin films with uniform properties. Spatial confinement and non-uniform thermal profiles have a profound impact on the dispersion relations, which will be explored in Chapters 4 and 5 respectively.

CHAPTER 3

CHARACTERIZATION TECHNIQUES

3.1. INTRODUCTION

This section will provide a detailed description of several techniques commonly used to characterize magnetic materials and that were used to collect the data presented in this thesis. First, I will describe a technique that proved fundamental to early magnetics research when it was first developed many decades ago - ferromagnetic resonance (FMR). I will then discuss two experimental techniques used to quantify the magnetic moment: vibrating sample magnetometry (VSM) and superconducting quantum interference detection (SQUID). Then I will discuss two very powerful techniques for studying spin waves, Brillouin light scattering spectroscopy (BLS), and magneto-optical Kerr effect spectroscopy (MOKE). Lastly, I will include an introduction the concept of spin wave excitations.

3.2. FERROMAGNETIC RESONANCE

The initial theory of ferromagnetic resonance (FMR) was introduced by Charles Kittel in 1948 [14]. Griffiths [25] made the first experimental observation of FMR. The FMR experiment can be used to study many properties of a magnetic material including the $4\pi M_s$ value [26–28], magnetic anisotropy [29–32], exchange coupling in multilayer systems [33, 34], and most commonly to provide insight into the spin relaxation mechanisms [35–38]. As discussed in Section 2.5, spins in a thin film experience a torque and undergo precession around the direction of the effective magnetic field with a frequency described by equation 2.22 for an in-plane magnetized film. The goal of FMR is to measure this resonance.

Since its discovery, FMR has been used to determine the damping parameter of magnetic materials. If the damping is introduced phenomenologically, as by the second term on the right of equation 2.12 for instance, one can use the resonance condition to find the diagonal components of the susceptibility tensor χ_{ij} :

$$\chi''_{xx} = \frac{\omega_M \omega H}{\omega \Delta\omega} \quad (3.1)$$

$$\chi''_{yy} = \frac{\omega_M}{\omega \Delta\omega} [\omega H + 4\pi\omega_M] \quad (3.2)$$

where ω is the frequency and $\Delta\omega$ is the linewidth which is equal to the FWHM of the susceptibility found by the points where χ is equal to half of its maximum value.

A diagram of a the FMR experimental setup is shown in Fig. 3.1. For a typical measurement the reflected microwave energy is monitored while the sample is excited at a fixed frequency and the external magnetic field is swept. The reflected energy drops when energy is absorbed by the magnetic material at resonance. Alternatively, it is possible to hold the field constant and sweep the frequency through the resonance. Either way the precession is typically driven with a spatially uniform field, either through use of a microwave cavity or a shorted waveguide. With a cavity, the frequency is held fixed at the resonance of the cavity then the field is swept through the FMR resonance as the reflected power is measured. This method is sensitive enough to study samples with very small power absorptions or small saturation magnetizations (low volume or with $T \sim T_c$), for instance. With a shorted waveguide, there is no specific cavity resonance so the frequency can be adjusted over a large range. It is possible to either rotate the sample or the magnetic field to perform angle dependent measurements to measure any anisotropy or measure the demagnetization coefficients for samples with constricted dimensions [39, 40]. Non-uniform spin wave modes

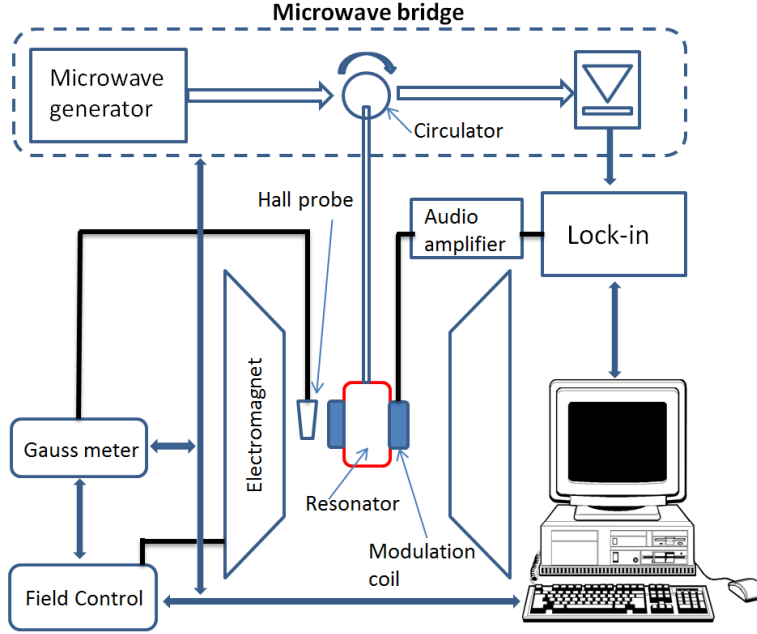


FIGURE 3.1. The main components of an FMR experiment. The electromagnet provides the static magnetic field, the CW stimulation is provided by the microwave generator. An audio amplifier drives a current through the modulation coil which oscillates the field make a lock-in style measurement possible. The reflected microwaves are converted to a voltage by a diode then sent to the lock-in to be analyzed by the computer.

[41]

can also be observed as resonances with lower absorption at higher frequencies in a surface wave geometry or lower frequencies for backward volume excitation geometries.

Even at FMR, the microwave power absorbed by the sample can be quite small. Thus a lock-in detection technique is often used where a small oscillating field parallel to the external field is created by modulation coils that are typically driven at acoustic frequencies. Thus it is actually the real and imaginary components of the dynamic susceptibility that are obtained. The absorption often appears in the data as the derivative of a Lorentzian function. The peak-to-peak distance is equal to the FWHM of the Lorentzian fit and is related to the FMR linewidth by

$$\Delta H_{FMR} = \sqrt{3}\Delta H_{pp} \quad (3.3)$$

which is related to the damping parameter by

$$\alpha = \frac{\mu\gamma\Delta H_{FMR}}{4\pi\omega}. \quad (3.4)$$

In the case of a multilayer stack or in a situation where propagating spin wave modes are excited, multiple resonances will appear at different frequencies but each can be individually fit to measure the resonance field and damping of each layer.

3.3. MAGNETOMETRY

Saturated ferromagnetic materials are surrounded by a non-uniform magnetic field where the strength of the field is directly proportional to the magnetic moment. If the sample is then oscillated, the magnetic field of the sample oscillates along with it generating a change in flux in the space around it. In magnetometry, magnetic induction through some arrangement of pickup coils is used to measure the magnetic moment of a sample at different fields, angles, and even temperatures. The measured quantity is the current generated in the induction coils which is proportional to the rate of change of flux. The main principles of two magnetometry techniques, vibrating sample and SQUID magnetometry are discussed below.

3.3.1. VIBRATING SAMPLE MAGNETOMETRY. Vibrating sample magnetometry (VSM) is an inductive measurement technique that uses a field and pickup coils to measure the induced current generated by vibrating a magnetic sample next to a set of coils [42]. The experimental concept is so simple that the first experimental apparatus consisted of an electromagnet, loudspeaker, a drinking cup and straw, and a rudimentary pickup coil [43]. A diagram of a more refined experimental configuration is shown in Fig. 3.2. A magnetic sample is placed at the end of a long, usually glass or metal, rod which is driven by a linear

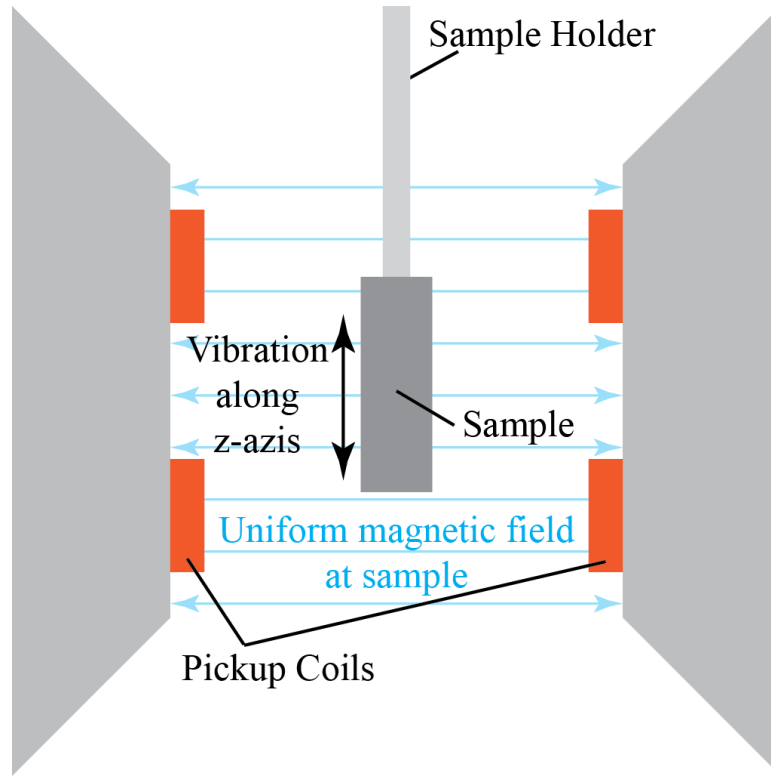


FIGURE 3.2. The main components of a vibrating sample magnetometer.

motor to oscillate the sample sinusoidally next to a set of pickup coils. The resulting change in flux through the pickup coils leads to an induced current due to Faraday’s law of magnetic induction.

To make a measurement with the VSM, the first step is to turn on the electromagnet to saturate the sample. Then the sample is centered in three directions. Once centered, the sample is oscillated at a constant rate. Measurements of the magnetization are made as a function of the external field to obtain a full hysteresis loop. The measurement can be repeated at different temperatures or field orientations to find the M_S vs T curve or to measure the angle dependent anisotropy both in and out of the plane of the film. While in most cases the VSM is not as sensitive as SQUID magnetometry it is a faster technique, because of the magnets typically involved, which is convenient for quickly finding the properties of magnetic materials.

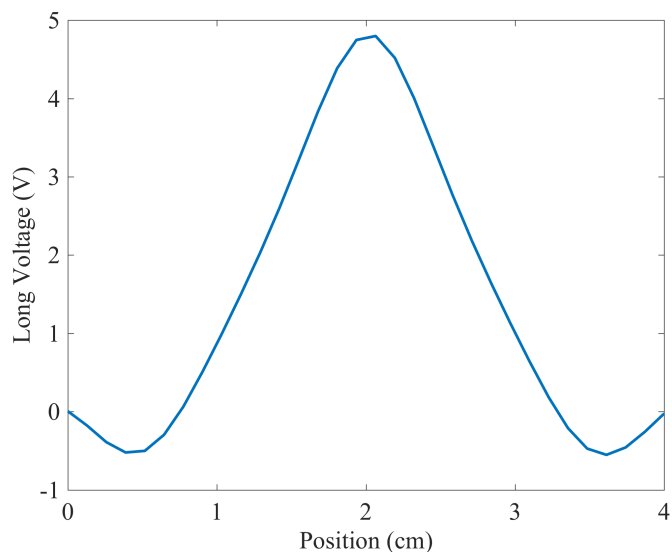


FIGURE 3.3. Typical measurement of a SQUID measurement showing the voltage of the current induced in the pickup coils as a function of the sample position.

3.3.2. SQUID MAGNETOMETRY. A superconducting quantum interference device (SQUID) is the most sensitive magnetometry technique usually used to detect magnetic signals as small as one flux quantum. A diagram of a typical SQUID measurement is shown in Fig. 3.3. The operating principle is similar to the VSM except that the induced current is detected by a superconducting Josephson junction. SQUID magnetometry is sensitive enough to measure one single Bohr magneton of magnetization. For more information on SQUID magnetometry please refer to Ref. [44].

3.4. LIGHT SCATTERING

Light scattering is a powerful tool for studying magnetic materials as it is non-contact, non-destructive, and can provide high resolution up to the diffraction limit. The basic principle is that light is scattered from the material under study and the properties of the scattered light are compared to those of the incident light. In this section we will focus on

the scattering process involving photons, the elementary particle of light, and magnons, the quasi-particles associated with magnetic waves.

Light scattering events can be categorized based on the energetics of the scattering process as either elastic or inelastic. In elastic scattering the photon momentum can change through the process of being absorbed and re-emitted by an electron but the photon does not lose or gain energy and thus the frequency remains constant through the scattering process. In contrast, inelastic scattering results in a scattered photon with a change in both energy and momentum. There are three categories of light scattering that are commonly used to study crystalline solids: Rayleigh, Raman, and Brillouin. The majority of the light scattered from a ordered crystalline solid is elastically scattered. Since the scatterers in a crystal are the ions in the lattice, the size of the scatterer is much smaller than the wavelength of the light. This type of scattering is referred to as Rayleigh scattering. Because the intensity of scattering is proportional to the number of scatterers, Rayleigh scattering can be used to measure fluctuations in the density of crystals [45].

We are then left with the inelastic scattering processes: Raman and Brillouin. Raman scattering happens when light scatters from atoms or molecules with some energy being lost to vibrational or rotational transitions [46]. Brillouin light scattering (BLS) happens when light scatters from low-energy and macroscopic collective excitations in a crystal such as from phonons or magnons. Raman scattering spectra are usually reported in wavenumber (cm^{-1}) units but typically involve much higher frequency shifts (10s of THz) than Brillouin scattering (10s of GHz). BLS has found broad application from measuring the elastic properties of water [47–50], a range of solids [51–55], collagen [56], muscle fibers [57], bone tissue, [56, 58], and

even spider silks [59] to measuring magnetic spin waves as discussed in this thesis. As a non-contact measurement, BLS has been used to determine the elastic properties of mammalian eyes on murine models and human tissues [60–62].

BLS has found broad application in magnetics research because it can measure spin wave properties and propagation. BLS is an effective tool for measuring the dynamic properties of magnetic materials because of the great degree of flexibility offered to the user in the experimental setup. Spin wave dispersion, discussed in Chapter 2, relies on many material parameters. Thus the BLS can be used as a direct measure of those material parameters. In addition to material properties, BLS has been used to study topics of fundamental interest in magnetics research including Bose-Einstein condensates [63, 64], spin-transfer torque [65–71], magnonic crystals [72–76], and spin wave logic devices [77–79].

3.4.1. MECHANISM OF LIGHT SCATTERING WITH MAGNETIC MATERIALS. In scattering experiments, the differential cross section, written as $d^2\sigma/d\Omega d\omega_S$, gives the number of photons that are scattered into a solid angle $d\Omega$ with a frequency between ω_S and $\omega_S + d\omega_S$ per unit of flux density of the incident light [80]. There are three key parameters of the scattered light which can be analyzed in the experiment: wavevector, frequency and polarization. A classical description of the BLS is based on considering the spin wave as a fluctuation in the dielectric permittivity (ϵ) caused by magneto-optical effects. As the spin wave propagates, the fluctuation propagates along with it and effectively creates a moving phase grating. The scattering can then be considered a Bragg diffraction coupled with a Doppler shift effect in which the scattered light receives a shift in wavevector and frequency determined by the phase velocity of the spin wave. Under this model the differential scattering cross section

can be written as [81]

$$\frac{d^2\sigma}{d\Omega d\omega_S} \propto \langle \delta\epsilon^*(\mathbf{q}_I - \mathbf{q}_S) \delta\epsilon(\mathbf{q}_I - \mathbf{q}_S) \rangle_{\omega_I - \omega_S} \quad (3.5)$$

where \mathbf{q}_I (ω_I) and \mathbf{q}_S (ω_S) are the wavevectors (frequencies) of the incident and scattered light, respectively, and $\langle \dots \rangle$ represents a statistical average. Here the correlation function is given by [80]

$$\langle \delta\epsilon^*(\mathbf{q}_I - \mathbf{q}_S) \delta\epsilon(\mathbf{q}_I - \mathbf{q}_S) \rangle_{\omega_I - \omega_S} \propto \int dt d^3(\mathbf{r}_2 - \mathbf{r}_1) e^{i(\omega t - (\mathbf{q}_I - \mathbf{q}_S) \cdot (\mathbf{r}_2 - \mathbf{r}_1))} \times \langle \mathbf{m}^*(\mathbf{r}_1, 0) \mathbf{m}(\mathbf{r}_2, t) \rangle. \quad (3.6)$$

Determination of the complete differential cross section of scattering between light and magnetic materials is an involved problem. The reader is encouraged to read Ref. [82] for more details on the description of the problem and derivation of the differential cross section and correlation function. For the purposes of understanding the material presented in this thesis, a few key points will be highlighted. First we notice that the number of scattered photons (within the given solid angle and frequency range) are proportional to the modulus-squared dynamic component of the magnetization averaged over the BLS probe spot. Second, the complete scattering cross section, provided in [82], shows that there are selection rules for the polarization of the light upon scattering such that the scattered light will have a polarization rotated 90° from the polarization of the incident light. Third, the fluctuations in the dielectric permittivity give rise to the magneto-optical effects of circular dichroism and birefringence. The first two effects play an important role in BLS experiments but polarization analysis is not performed so the effects of the third point are not observed. However,

we present a brief description of the Magneto-optical Kerr experiment that highlights the capabilities of exploiting these magneto-optical effects.

Magneto-optical Kerr effect (MOKE) is a reflectometry experiment that relies on a rotation to the polarization of light, called the Kerr effect, imposed by a magnetic material upon reflection. This effect was discovered by John Kerr in 1877 [83]. The scattering process results in a small rotation of polarization (called the Kerr angle) that arises due to a fluctuation of the off-diagonal terms of the permittivity tensor that depends on the local magnetization of the material. The electric field of the light interacts with the dynamic magnetization in a way that leads to a bi-refringence in which left and right circularly polarized light have different speeds through the material. Thus if linearly polarized light is incident upon a magnetic sample, the reflected light will become elliptically polarized and/or will show a change in amplitude depending on the geometry.

A MOKE experiment can be performed in three geometries as shown in Fig. 3.4: polar, longitudinal, and transverse. Analyzing the change in polarization of the reflected light, the Kerr angle Θ_{Kerr} , allows one to measure the magnetization of the sample. Since spin waves are defined as fluctuations in the magnetization, MOKE can be used to gain a very complete picture of spin wave dynamics including phase information [7]. It is commonly used to measure hysteresis but can be used in a micro-focussed time-resolved configuration to obtain sensitive measurements of the response of the magnetization to a stimulus in the time domain.

3.4.2. BRILLOUIN LIGHT SCATTERING. Brillouin light scattering (BLS) spectroscopy, theorized by Brillouin in 1922 [85], is an inelastic light scattering technique wherein light is scattered from a crystalline material in order to measure low-frequency excitations such

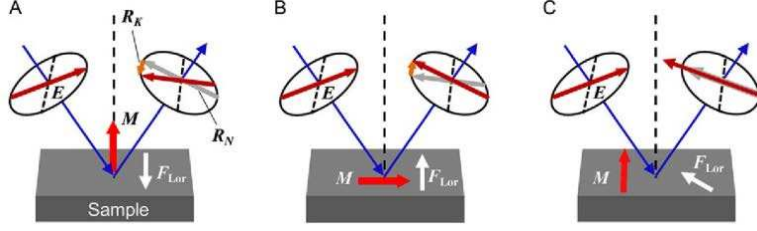


FIGURE 3.4. The three experimental configurations of the MOKE effect for thin films. In a) the magnetization lies perpendicular to the plane of the film (referred to as polar MOKE), b) the magnetization lies in the plane of the film parallel to the scattering plane (longitudinal MOKE), and c) when the magnetization lies in the plane of the film perpendicular to the scattering plane (transverse MOKE). This figure was reproduced from [84] with permission from Elsevier.

as magnetic spin waves, lattice density waves (phonons), and surface excitons [80]. Because of the measurement sensitivity and the wide range of problems that can be studied, BLS is a powerful technique in modern magnetics research. Figure 3.5 shows diagrams of the scattering processes between photons and magnons. In BLS there are two types of inelastic scattering processes, Stokes scattering wherein a magnon is created and thus the scattered light has a reduced energy and a lower frequency as shown in Fig. 3.5a. This energy shift shows up in the data as a negative frequency shift relative to the elastic peak. Anti-Stokes scattering occurs when a quasiparticle is annihilated resulting in a scattered photon with higher energy and frequency (positive frequency shift relative to the elastic peak). The shifted energy and momentum of the scattered photon are given by

$$\hbar\omega_S = \hbar\omega_I \pm \hbar\omega_m \quad (3.7)$$

$$\hbar\mathbf{q}_S = \hbar\mathbf{q}_I \pm \hbar\mathbf{k}_m \quad (3.8)$$

where $\mathbf{q}(\omega)$ is the wavevector (frequency) of the photon, the subscript I (S) denote the incident (scattered) photon, and m denotes the magnon.

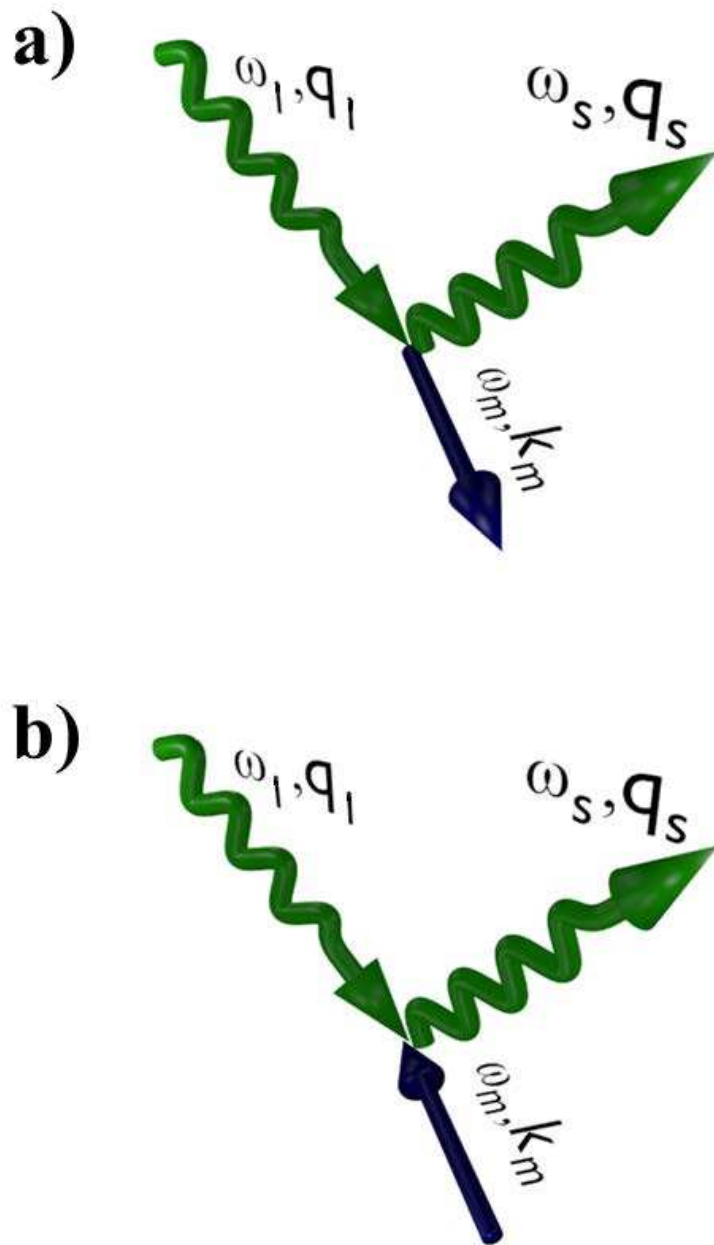


FIGURE 3.5. (a) Scattering event for a Stokes process resulting in the creation of a magnon. (b) Anti-Stokes process involving the destruction of a magnon [86].

Since the frequency shifts involved in BLS are small (GHz range) and the scattering cross sections are small, specialized equipment is required to perform BLS measurements. The crucial elements of the BLS are a single-mode laser and a sensitive interferometer to

distinguish the inelastically scattered light from the elastic light. A diagram of the experimental apparatus used for BLS is shown in Fig. 3.6a. In order to measure small shifts in the frequency of the scattered light ($\pm 1-100$ GHz shift to 500 THz light), it is necessary to use a single-frequency single-mode laser. For the work presented here we have used the Excelsior laser by Spectra Physics, a 200 mW diode laser with a 532 nm wavelength and a spectral linewidth < 0.5 nm. The laser is linearly polarized in a direction normal to the optical table. Light from the sample is focused on the sample with traditional optics coated for optimum transmission of light at this wavelength. For our experiments, optimized for the detection of magnons, after the light scatters from the sample it passes through a linear polarizer set to extinguish light without a rotation in polarization. Due to the selection rules, linearly-polarized light scattered from magnetic materials is polarized at 90° with respect to the polarization of the incident light as discussed in Section 3.4.1. Hence the polarizer acts as the first step to isolate the magnetically-scattered light from the elastically scattered light that forms a majority of the scattered light. The polarizer is typically removed to measure light scattered from phonons in the crystal.

The light is then guided into the input pinhole of the interferometer as shown in Fig. 3.6b. Since the light scattered from magnons is considerably less intense than the rest of the scattered light even after passing through the linear polarizer, a highly sensitive interferometer with a large extinction ratio is necessary. Because light scattered from spin waves is usually 10s of GHz, a tandem multi-pass Fabry-Perot interferometer is used. The essential element of an interferometer is two partially silvered mirrors with a reflectivity around 95 percent that are parallel and separated by a known distance that only allow efficient pass-through of light that has a wavelength equal to an integer multiple of the spacing

between the mirrors. The entire spectrum of the scattered light enters the interferometer and is reflected many times. The reflected light interferes with itself constructively and destructively depending on its wavelength. The interference will be constructive when the phase difference upon reflection, is equal to $2\pi n$ as given by [87]:

$$\delta = \left(\frac{2\pi}{\lambda} \right) 2d_m = 2\pi n \quad (3.9)$$

Thus the mirror spacing must be $d_m = n\lambda/2$ where $n=0, 1, 2, 3, \dots$. In this way the transmitted wavelength (frequency) can be selected by scanning the spacing between the two mirrors.

If light were to pass through just one etalon with a given spacing it would have the transmission profile shown in the top of Fig. 3.7. The difference in wavelength between two adjacent transmission peaks is referred to as the free spectral range (FSR) in wavelength. It is given, in terms of wavelength, by

$$FSR(wavelength) = \frac{\lambda^2}{2d_m} \quad (3.10)$$

or in terms of frequency as

$$FSR(frequency) = \frac{c}{2d_m}. \quad (3.11)$$

One etalon passes many wavelengths of light as long as they obey equation 3.9. Thus the precise frequency cannot be unambiguously determined. To bypass this shortfall a second etalon may be placed in series with the first. The spacing of the second etalon can be set to allow the same wavelength of light to pass but with a different half-integer number of wavelengths as the transmission band shows in Fig. 3.7. This combination allows only one

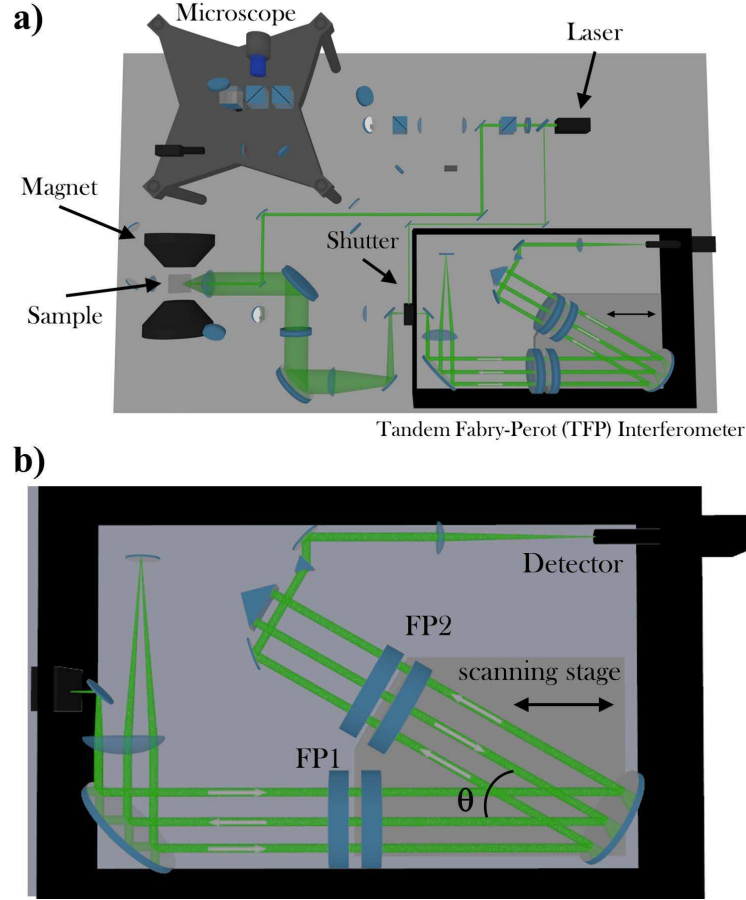


FIGURE 3.6. a) Diagram showing an overview of the BLS experiment in the Nanomagnetism Lab at CSU. The laser is shown in the back-scattering configuration as part of a conventional (not micro) BLS setup. b) Diagram of the beam path within the interferometer. FP1 and FP2 are Fabry-Perot style etalons separated by an angle θ on a scanning stage which simultaneously controls the spacing inside of both etalons [86].

unambiguous wavelength to pass through both. Now the spacing of both etalons can be swept while maintaining a constant ratio of their spacings, usually up to one FSR. In our tandem configuration the etalons are mounted with an angle θ between them so that the two mirror spacings are related by

$$d_{m,FP2} = d_{m,FP1} \cos \theta \quad (3.12)$$

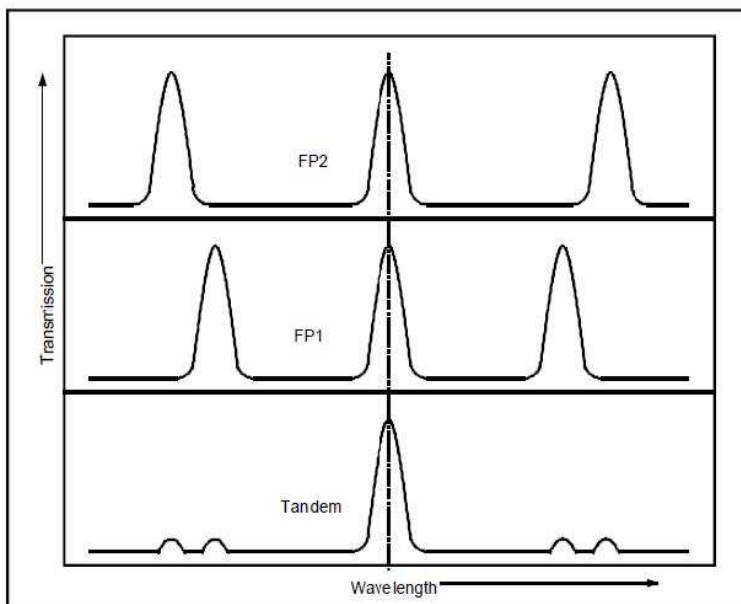


FIGURE 3.7. (top) Transmission spectrum of one etalon shown (FP2). (middle) Transmission spectrum of a second etalon (FP1) set to a different order of a wavelength allowed by the spacing of the first etalon. (bottom) Transmission through both etalons. Only the unambiguous wavelength permitted by the spacing of both etalons will pass [88].

as shown in Fig. 3.6b. The TFP used in our lab is a multi-pass interferometer in which the scattered light passes through each etalon three times for a total of six passes before going to the detector (shown in Fig. 3.6b). This results in a very large extinction ratio, better than 10^{10} and therefore a much better signal-to-noise ratio as compared with a single pass through the interferometer [89].

To analyze the different frequencies contained in the scattered light, the stage holding one side of the mirrors is scanned as indicated by the black arrows in Fig. 3.6b. This setup allows a constant ratio of the spacings as they scan from the wavelength of the laser through the FSR. Instead of scanning through the elastically scattered light, a double shutter is used at the input pinhole of the interferometer. This shutter serves a dual purpose. It protects the detector from the elastically scattered light and it also lets a sample of the initial laser beam through that serves as a reference beam and allows the user to normalize the inelastic

signal to the reference to account for any fluctuations in laser intensity. This reference beam is also used to measure the finesse of the etalon pairs which is a direct measure of their parallelity. The parallelity of the mirrors is stabilized by maximizing the finesse through piezos controlled by a feedback loop in the software. The BLS can be operated in two configurations: conventional and micro-BLS.

3.4.2.1. *Conventional BLS.* The term conventional BLS is used to refer to the scattering setup without a microscope objective. A lens is still used to focus the light on the sample just with much lower power. The focussing lens we use results in a spot size of around $50 \mu m$. Conventional BLS can be performed in two ways: backward and forward scattering. The backward scattering configuration is typically used to study opaque materials, for instance metals. In this configuration, shown in Fig. 3.8, the light is focussed onto the sample with a lens, scatters from the sample and then travels back through the lens to be analyzed by the interferometer. The back-scattered light has been scattered through an angle of 180° . Due to the conservation of momentum, setting the angle of incidence allows one to select the wavenumber that is measured. The wavenumber that will be measured is related to the angle of incidence in the following way

$$k = 2q_i \sin\phi. \tag{3.13}$$

where q_i is the wavenumber of the incident photon and ϕ is the angle of incidence.

For transparent materials, commonly insulators like YIG, the forward scattering configuration is used as shown in Fig. 3.9. In this configuration an additional lens is used to focus the light on the sample before it passes through the sample and the collecting lens. For transparent samples forward scattered light is much more intense than backscattered light

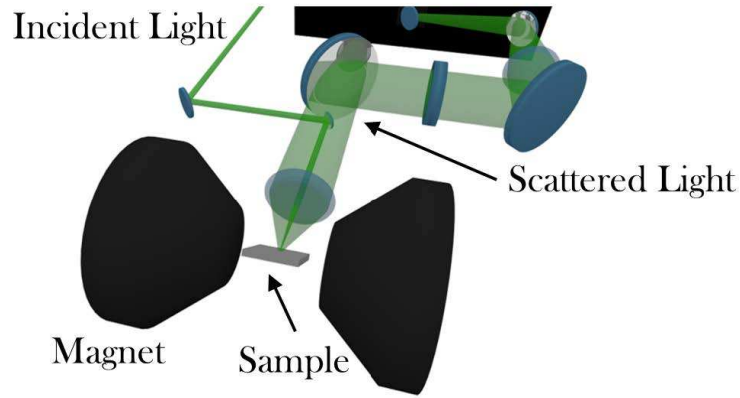


FIGURE 3.8. BLS beam path for the back-scattering configuration. The incident light is focussed onto a sample, mounted at an arbitrary angle, then the scattered light is collected by the same lens and directed into the input pinhole of the interferometer [86].

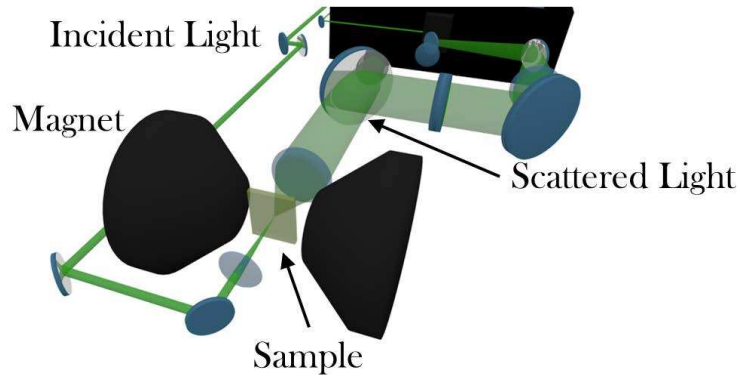


FIGURE 3.9. BLS beam path for the forward-scattering configuration. Here the incident light is transmitted through the magnetic film, collimated by the collecting lens, and directed into the input pinhole of the interferometer. [86].

resulting in an improved signal-to-noise ratio, however, the measurements are usually only made at normal incidence so the ability to select the wavevector by changing the angle is lost so any wavevector control comes from the choice of antenna design or by using apertures, diaphragms, slits, or razor blades to analyze the scattered wavevectors. This is called wavevector selective BLS and more detailed descriptions are available in [90–92].

The BLS can also be operated in a time-resolved configuration. A spin wave pulse is generated by either a DC pulse generator or a CW signal generator paired with a transistor-transistor logic (TTL) switch. When the amplitude of the pulse rises past a certain level a timer is triggered. This timer records the arrival time of all photons measured at the detector until the next pulse is triggered. Hence this is a time-of-flight measurement. The photons are binned according to their arrival time and frequency. Performing time-resolved and two-dimensional measurements essentially allows the user to construct a video of the propagation of each spin wave mode. One can thus determine the group and phase velocities, propagation angles, and it is also possible to directly measure wave interference phenomena and non-linear effects.

Figure 3.10 shows a screenshot of the software interface used to control the BLS apparatus called TFPDAS4. This software plays a crucial role in the active stabilization of the etalon mirrors, setting the timing of the scanning of the etalon spacing, and analyzing the results. The plot shown in the screenshot gives a live view of the BLS spectrum during the scan, where the BLS intensity in photon counts is shown on the vertical axis and the BLS frequency shift is shown on the horizontal axis. The reference peak is displayed at $f=0$ GHz. The negative frequencies compose the Stokes spectrum and correspond to magnon creation processes where the photon has lost energy to the magnetic system. The positive frequencies are referred to as the anti-Stokes spectrum and are the result of a process where the scattered photon has gained energy from the magnetic system by the annihilation of a magnon. The peaks occur at a specific frequency that corresponds directly to the frequency of the detected spin wave.

The timing of the scan can be controlled by a region of interest (ROI), such that outside the ROI the mirrors can be scanned very quickly to save time but scanned slowly within

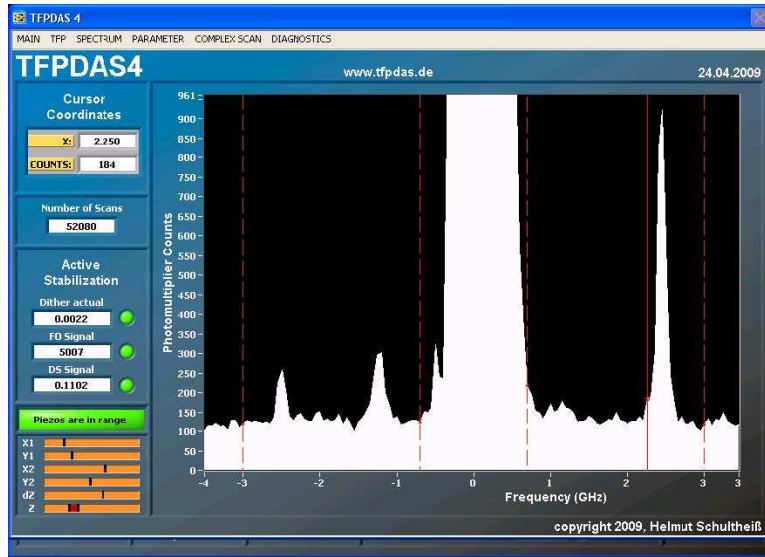


FIGURE 3.10. Screenshot of the software interface used to control the BLS experiment [86].

the ROI to increase the signal obtained there. This region is indicated by the red dashed vertical lines shown in Fig. 3.10. At the zero frequency location, the double shutter is used to analyze the reference beam from the laser instead of the elastically scattered light, as previously discussed. This peak is referred to as the reference peak and is used to normalize all BLS spectra to account for fluctuations in laser intensity. The smallest frequencies that can be measured are around 500 MHz which is determined by the speed of the double shutter and the spectral width of the elastically scattered light.

The software allows a so-called “complex” scan to be performed. This allows the computer to control up to three variables remotely and perform BLS scans as a function of those changing variables. In our lab, we have used time, microwave excitation power and frequency, field, and spatial dimensions as the computer-controlled variables. The user defines the step size and range that these variables should be swept through. This software combined with the BLS apparatus constitute a powerful method to observe many magnetic effects. A more detailed explanation of the software can be found in [93–95].

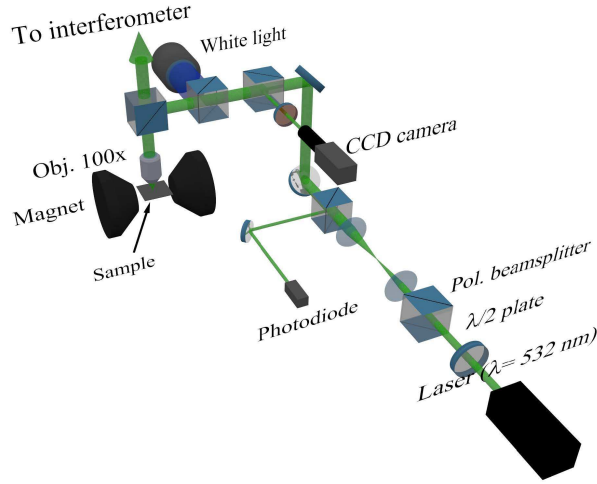


FIGURE 3.11. Diagram of the essential micro-BLS apparatus [86].

3.4.2.2. *Micro-BLS*. A more recent advancement of the BLS technique is the addition of a microscope objective to improve the spatial resolution of the measurement [96, 72]. This technique is highly useful for patterned magnetic thin films and was used to obtain the data presented in Chapter 4. The spot size of the micro-BLS is approximately 250 nm allowing for a much more localized measurement of the spin wave excitations. Since the light is so heavily focussed, the intensity is also much higher resulting in a better signal to noise which helps with the fact that a much smaller population of magnons is being characterized. The essential components required for micro-BLS are a microscope objective, a CCD camera, and high-precision three-dimensional translation stages as shown in Fig. 3.11.

In our setup, we use a Zeiss microscope objective with 100x power, numerical aperture (NA) of 0.75, and a working distance of 3 mm. Due to the nature of the stages and objective, micro-BLS is performed in a back-scattered geometry at normal incidence. The light comes in at a range of angles determined by the numerical aperture of the objective $NA = n \sin \theta$, where n is the index of refraction of air and θ is the angle of incidence. In our case, $NA=0.75$, which corresponds to the range $\theta = 0-48.5^\circ$ as found using equation 3.13.

The CCD camera allows for active monitoring of the sample location under the laser spot. The particular camera we use is a Thorlabs model DCC1545M CMOS monochromatic CCD camera. The BLS software is designed to use autocorrelation functions to actively control the stages to maintain a selected region of the sample at its original location to counter thermal drift. A portion of the reflected laser light is used for focussing. The maximization of the reflected light intensity happens when the sample is in the focus of the objective. The software also continuously analyzes the reflected light intensity measured by a photodiode to control the stages and keep the sample in focus. To control the position at such a fine level a set of Newport high-precision translation stages (model numbers XMS50 and GTS30V) were used. The stages used to control the lateral position have a precision of 1 nm while the vertical stage has a precision of 50 nm. This precision is sufficient to maintain the focus and stabilization over long periods to make possible fine spatial scans.

The software used to control the micro-BLS in our lab was developed by Helmut Schultheiß and a more detailed description of the software can be found in Ref. [97]. It can be run in conjunction with the software used to control the conventional BLS to perform complex spatial scans to map out mode profiles and it can even be used in a time-resolved setup. Figure 3.12 shows a typical screenshot of a patterned magnetic film in the focus of the objective. The magnetic structures are the dark elements within the picture. The red crosshair indicates the location of the probing laser spot. The laser spot itself would overexpose the image of the CCD and so it is filtered out with a notch filter. The red box shows the region chosen for stabilization. The software periodically uses a cross-correlation algorithm to recenter the original contrast of the red box within the yellow box to account for drift. The green box

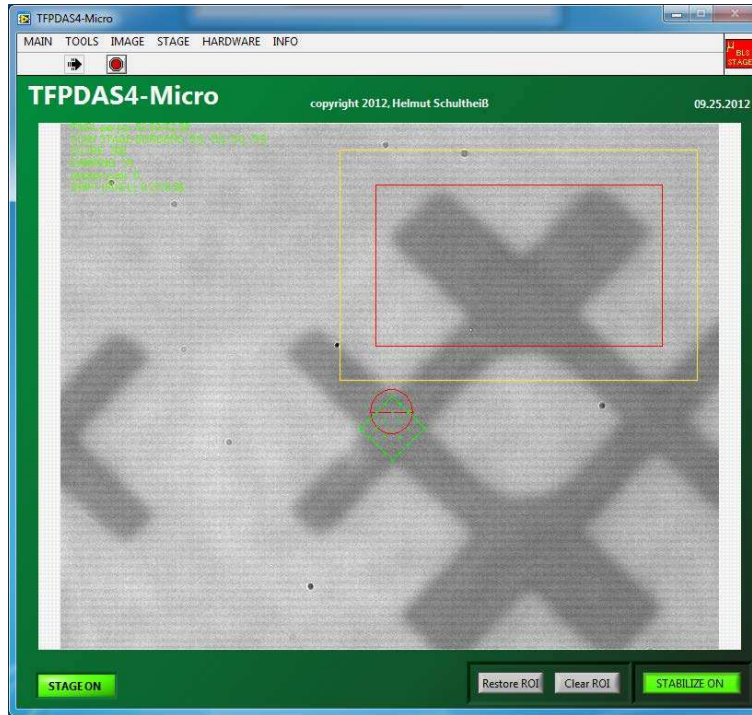


FIGURE 3.12. Screenshot of the software used to control the micro-BLS. The image shows a pound-key-structure that will be discussed further in Chapter 4. The structure has lateral dimensions of $12\ \mu\text{m}$ [86].

represents the scanning ROI which contains the precise locations where BLS spectra will be obtained.

3.5. SUMMARY

There are many powerful techniques used to study magnetic materials. Since all of the techniques have their own strengths and limitations, it is common to use several techniques in a magnetism research project. While this thesis focuses on BLS as the main technique for studying spin waves, SQUID was used as an efficient way to find the $4\pi M_S$ of the YIG film studied in Chapter 5, antenna-based FMR was used over a wide range of frequencies to fit for the YIG film thickness, and MFM (magnetic force microscopy) was used in Chapter 4 to determine the static spin configuration. For dynamic measurements, other commonly used techniques include TR-MOKE and time-resolved X-ray techniques but the former has similar

spatial resolution to micro-BLS and is not as sensitive to small signal dynamics, and while X-ray-based techniques (i.e. XMCD (x-ray magnetic circular dichroism), STXM (scanning transmission X-ray microscopy) offer the advantage of element specificity and higher spatial resolution, they require the use of a synchrotron source. Electron microscopy can also be used for magnetic imaging but has quite limited ability to access dynamics. Inelastic neutron scattering is another method that can be used to measure spin wave dynamics, however, it requires large (several mm^2) samples and imaging is not possible. Micro-BLS offers high spatial resolution and sensitivity as well as experimental convenience.

CHAPTER 4

DYNAMIC EXCITATION OF A MAGNETIC ANTIVORTEX

4.1. INTRODUCTION

In this chapter, we will explore the effect of shape on microscopic patterned thin films. As discussed in Chapter 2, ferromagnetic materials have neighboring moments that are exchange coupled in a way that favors parallel alignment. Under a strong enough applied field all the moments within the film will be parallel to each other, this is called the saturated state. When the field is removed, however, magnetic domains will often form in order to minimize the magnetostatic energy. As a result, there will always be competition between the exchange and magnetostatic energies. It is sometimes possible to use this energy balancing act to our advantage. If the shape of our patterned thin film is tailored just right, in addition to common Landau domain patterns, more exotic metastable ground states that have fundamentally interesting behavior that is highly useful for device applications can be formed. Here we will study the dynamics of two such states: the magnetic vortex and its topological counterpart, the antivortex.

4.2. BACKGROUND AND MOTIVATION

Exotic spin textures in patterned magnetic nanostructures are currently attracting a great deal of attention because they exhibit a variety of interesting physical properties and show promise for applications. By controlling the material properties, geometry, and the external field history, it is possible to form and stabilize topological magnetic states such as magnetic vortices [98, 99], antivortices [100, 101, 1], and more exotic states such as skyrmions [102].

The magnetic vortex, shown in the top of Figure 4.1, is a topological spin configuration where the local magnetic moments are oriented azimuthally around a central core region where the moments tilt out of the plane of the thin film, either up or down. The magnetic vortex has nearly complete flux closure, meaning that there are no free magnetic poles except at the core. This is consequently a low energy configuration and is the lowest energy configuration in many thin magnetic disks depending on the aspect ratio of the structure [103]. Vortices exhibit a variety of interesting dynamic properties that include sub-gigahertz gyrotropic motion that can be driven by magnetic fields [104–106], spin-polarized currents [107–109], higher-frequency (> 1 GHz) quantized spin excitations [110, 111], long range magnetostatic coupling interactions [112, 113], dynamic core reversal [114, 115], and selective ordering effects [116] where a different ground state, each with unique dynamic behavior, can be chosen in the same vortex array. These results would be highly useful in magnonic crystals that rely on periodically arranged vortex states or as nano-oscillator spin wave sources.

The antivortex (AV) state, shown in the bottom of Figure 4.1, involves spins that sweep in from two opposite sides (e.g., the top and bottom) and out from the other two (e.g., left and right), is metastable and more difficult to create as an isolated entity [100, 101, 1, 117]. For this reason the magnetic antivortex has received comparatively less attention even though simulations suggest that AVs should have similarly rich dynamics [118] and may, in fact, have higher potential for spin wave-based applications [117, 119, 120]. Simulated results and analytical models have shown that the AV core will gyrate and that the polarity will reverse when driven by a suitable in-plane magnetic field or a spin-polarized current [119, 121–124]. While these low-frequency processes have been observed experimentally [122, 125, 126], the only studies that have been done thus far on the high-frequency spin dynamics of the AV are

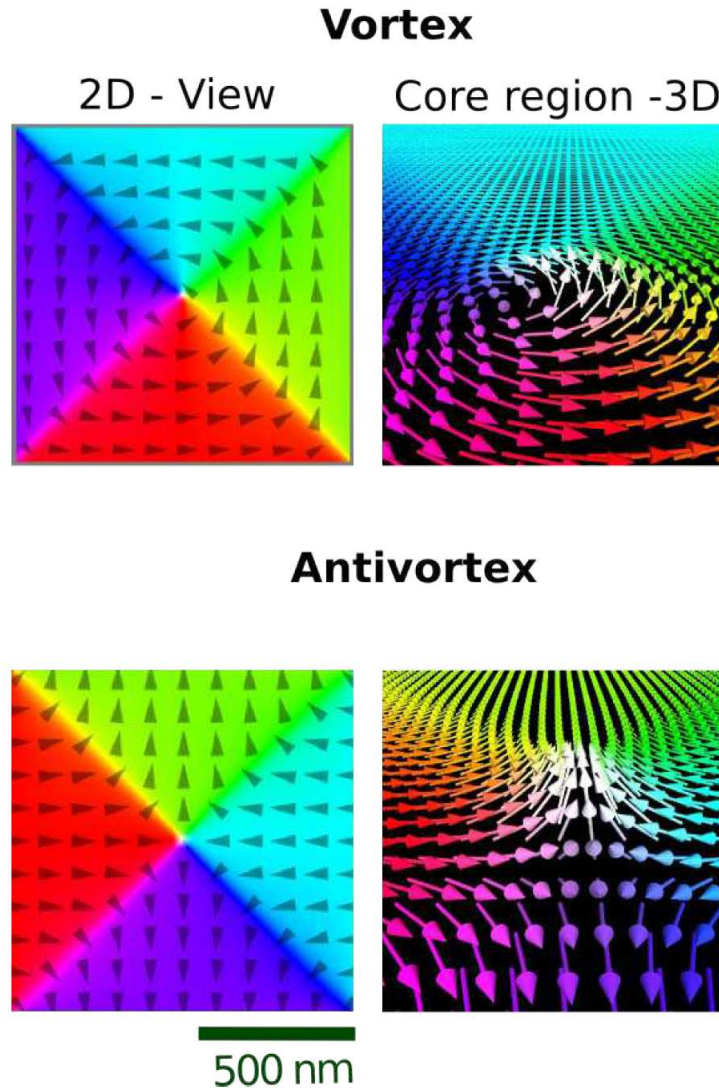


FIGURE 4.1. Spin distributions of the magnetic vortex (top) and antivortex (bottom) states. In the vortex configuration, spins curl smoothly around a central out-of-plane core. In the antivortex configuration, spins sweep in toward the central core in two directions and sweep out away from the core in the other two directions. This allows the magnetization of the antivortex state to have smooth transitions into adjacent microwires [3].

theoretical [118]. Furthermore, it has been shown that is possible to create an antivortex in intersections of microwires resulting in smooth transitions between the static magnetization state of the AV and the microwire (no domain walls in between). This chapter will explore

the dynamic behavior of an antivortex in such a structure and explore the possibility of the antivortex to act as a short wavelength spin wave source.

We use the microfocus Brillouin light scattering (micro-BLS) spectroscopy technique, discussed in Chapter 3, which can be used to obtain frequency-resolved information on dynamics in magnetic materials via inelastic light scattering with diffraction-limited spatial resolution [127], to investigate the dynamics of magnetic AVs in Permalloy microstructures. Measurements conducted as a function of frequency reveal a rich spectrum for the AVs, and spatial imaging combined with micromagnetic simulations provide additional insight into the observed modes.

4.3. EXPERIMENTAL SETUP

4.3.1. IN-PLANE EXCITATION. To investigate the dynamics of the magnetic AV state with in-plane (IP) excitation, pound-key-like magnetic microstructures made of Permalloy ($\text{Ni}_{80}\text{Fe}_{20}$) were fabricated on top of an 18 μm wide, 250 nm thick gold coplanar waveguide using electron beam lithography, magnetron sputtering, and liftoff. Figure 4.2 shows the microstructure grown on top of the waveguide with sample dimensions of $L = 6 \mu\text{m}$, $b = 2 \mu\text{m}$, $w = 1 \mu\text{m}$, and thickness $t = 37 \text{ nm}$. Atomic force microscopy measurements show that the peak-to-peak surface roughnesses of the gold waveguide and the patterned Permalloy structures are 3.5 and 5.0 nm, respectively.

This structure was specifically designed to study AV dynamics not only because it has a cross-tie geometry, which improves the success of localized AV formation, but also because there are adjacent legs into which AV-generated spin waves can travel. The differences in the shape anisotropy in the wide and narrow sections of structures with this general shape can be used to influence the reversal process and hence to promote the nucleation of magnetic AVs,

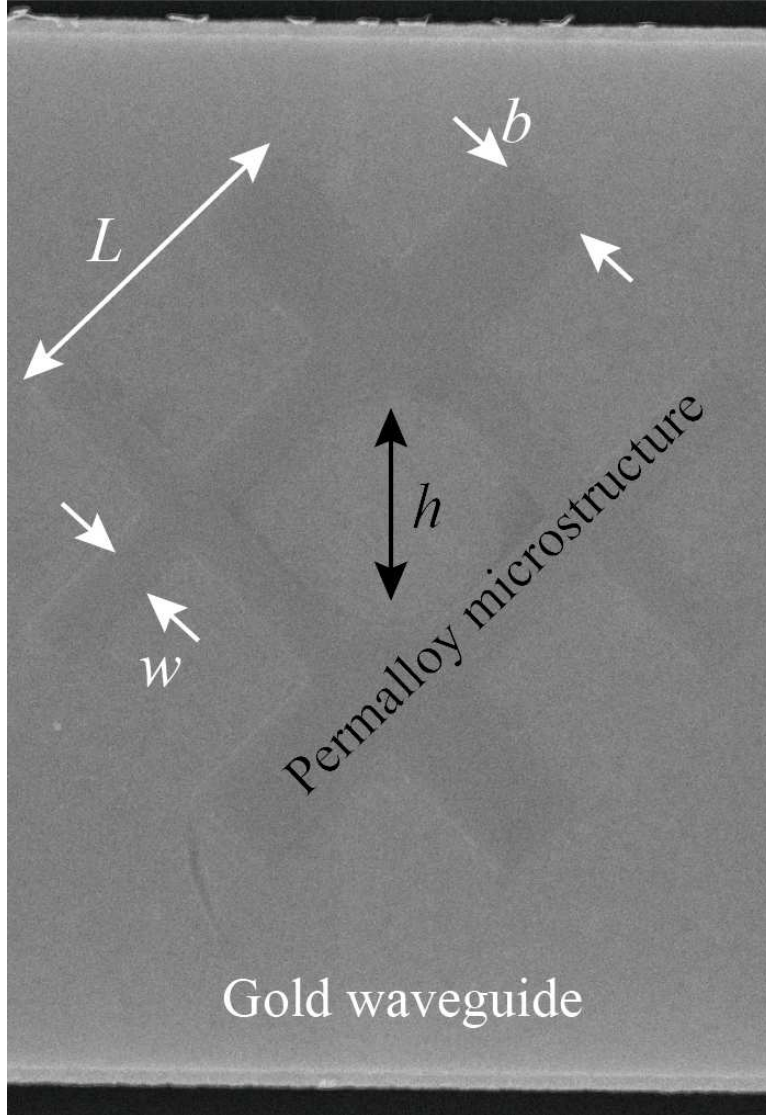


FIGURE 4.2. SEM image of the Permalloy microstructure on top of a gold waveguide shows the experimental geometry. The sample dimensions are $L = 6 \mu\text{m}$, $b = 2 \mu\text{m}$, $w = 1 \mu\text{m}$, and thickness $t = 37 \text{ nm}$. For the micro-BLS measurements the laser spot was focussed on the region of interest having a spot size less than 250 nm . Figure 3.12 shows a characteristic screenshot of the microstructure in-focus and stabilized.

as described in Refs. [1, 2]. The AV states were nucleated by first applying a static field of $H = 600 \text{ Oe}$ along structure diagonal containing the wide legs to saturate the microstructure. Then a much smaller field, $H = 60 \text{ Oe}$, was applied in the opposite direction, to switch only the wide legs to be magnetized in the reversed direction. The magnetization in the narrow

legs is effectively pinned in the original direction by the strong shape anisotropy imposed by the local demagnetization field. The sample was excited using a microwave field h , applied along the structure diagonal as illustrated in Fig. 4.3. A microwave power of 13 dBm, which corresponds to $h \approx 0.6$ mT, was used for all measurements. At this power the structures exhibit a linear response within the frequency range that was considered (1-7 GHz).

Magnetic force microscopy was then used to determine the initial state. As shown in the MFM images, two AVs were present in the samples (AV_1 and AV_2), identified based on the hourglass-like contrast observed at these two intersections. For details on the factors that influence the AV formation success rate, including the role of the sample geometry and the angle of the applied field, refer to Ref. [2]. Figure 4.3 also shows two small leg intersections where AV nucleation was not successful and saturated states are observed: one state saturated parallel to the dynamic field h (which I will call Sat_{\parallel}) and the other state saturated perpendicular to the h (called Sat_{\perp}). These two saturated states provide a reference point for comparison to identify the dynamic behavior which was unique to the AV state.

4.3.2. OUT-OF-PLANE EXCITATION. We also set out to study the AV dynamics under the influence of an out-of-plane (OOP) excitation. Instead of a coplanar waveguide, the Permalloy microstructure was fabricated inside a gold hoop-shaped waveguide that was 250 nm thick. The dimensions of the structure, as defined in Fig. 4.4 are $L = 5.2$ μm , $b = 1.6$ μm , $w = 0.61$ μm , and a thickness of $t = 37$ nm. In this structure w is smaller as compared to the sample used for the IP excitation measurements, which is due to the difference in the backscatter of the electrons in the e-beam patterning over silicon (for OOP excitation) vs gold (for IP excitation) that resulted in a larger effective dose for the structure patterned

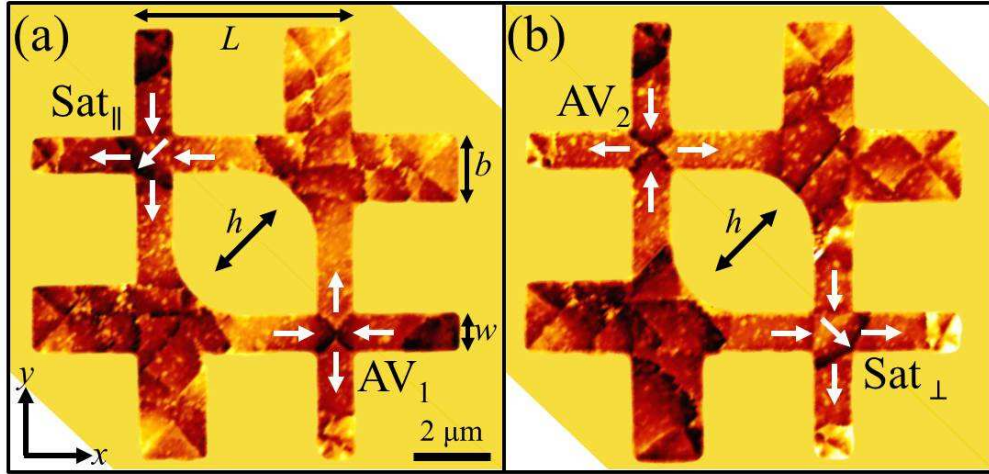


FIGURE 4.3. MFM images of two 37-nm-thick Permalloy structures superimposed on a diagram of a waveguide to illustrate the experimental geometry for an in-plane excitation field. The upper left intersection in structure (a) is saturated parallel to the dynamic field h (Sat_{\parallel}) while the hourglass-like MFM contrast in the lower right intersection indicates that this intersection contains a single AV (AV_1). Structure (b) has an AV in the upper left intersection (AV_2) and is saturated perpendicular to h in the lower right intersection (Sat_{\perp}). The white arrows indicate the direction of the magnetization.

on the gold. The dynamic field was generated by CW microwaves in a range of 1-7 GHz at a power of 15 dBm. The power actually converted to a magnetic field at the sample was expected to be appreciably lower due to impedance mismatch at the waveguide/picoprobe interface. A calculation following the Biot-Savart law was used to find the field inside the hoop at the location of the AV and indicate that h is around a mT which is strong enough to excite dynamic behavior but not strong enough to stimulate non-linear effects. The BLS signal is linear as a function of the microwave power and no parasitic signals at off-pumping frequencies were observed. All of the measurements were performed in the absence of a static external field to preserve the magnetic state. MFM measurements were performed before

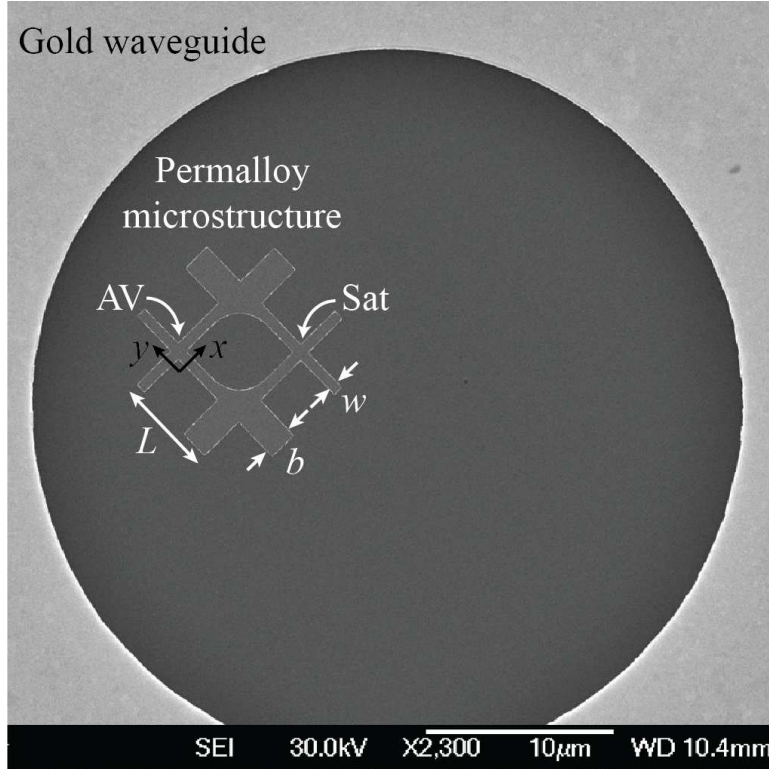


FIGURE 4.4. SEM image of the Permalloy microstructure inside a hoop-shaped waveguide shows the experimental geometry. The sample dimensions are $L = 5.2 \mu\text{m}$, $b = 1.6 \mu\text{m}$, $w = 0.61 \mu\text{m}$, and thickness $t = 37 \text{ nm}$. The magnetic states of the intersections were determined in a separate imaging step by MFM.

and after both the IP and OOP BLS measurements to confirm the presence and persistence of the AV state by the hour-glass like contrast previously discussed.

4.4. EXPERIMENTAL RESULTS

Two types of micro-BLS scans were used to study the dynamic behavior with both IP and OOP excitation. Micro-BLS measurements were made as a function of the microwave pumping frequency f_p for each of the intersections shown in Fig. 4.3 and in the OOP sample intersections at points inside of and near the intersections. Next, spatial maps of several modes of interest were made by raster scanning the micro-BLS probing laser over a square region slightly larger than the small leg intersections and using a step size close to the spatial

resolution of the micro-BLS (≈ 300 nm) where spin excitations with wave vectors of up to $20 \mu\text{m}^{-1}$ (minimum wavelength $\lambda \approx 0.3 \mu\text{m}$) [128] can be detected.

4.4.1. IN-PLANE EXCITATION.

4.4.1.1. *Frequency scans.* Sweeps of the pumping frequency f_p were performed to find modes that are unique to the AV state. Figure 4.7 shows micro-BLS measurements for each of the AV, Sat_{\parallel} , and Sat_{\perp} states as a function of f_p , measured over a frequency range from 1 to 7 GHz in 100 MHz increments. These measurements were made at fixed points that were slightly offset from the center of the intersection. An off-center point was chosen because the resonances of interest involve motion within the intersection but the amplitude is expected to be larger away from the core. The BLS intensities shown here were obtained by integrating each spectrum over the range $f_p \pm 350$ MHz and then normalizing to a reference signal that is proportional to the power of the incident laser beam to account for any fluctuations in the laser intensity as shown in Fig. 4.5. Figure 4.6 shows a typical comparison between an extracted f_p signal and the reference peak indicating the stability of the laser intensity. As shown in Fig. 4.7, the intensity of the strongest Sat_{\perp} resonance is $> 10,000$ counts as compared to $\approx 1,700$ for the AV and Sat_{\parallel} states. The higher intensity for the Sat_{\perp} state occurs because the spins in the intersection are mainly perpendicular to h and consequently the torque is large.

The most notable feature of the AV signal in Fig. 4.7 is the peak near 5.9 GHz. This is the strongest feature for all of the magnetic states in this frequency range and it is relatively wide with several sharper peaks, which suggests that there are multiple closely spaced modes within this range. In addition to the strong peak at 5.9 GHz, the AV state also exhibits a resonance at 3.4 GHz that is well above the noise level. Other features in the AV spectrum

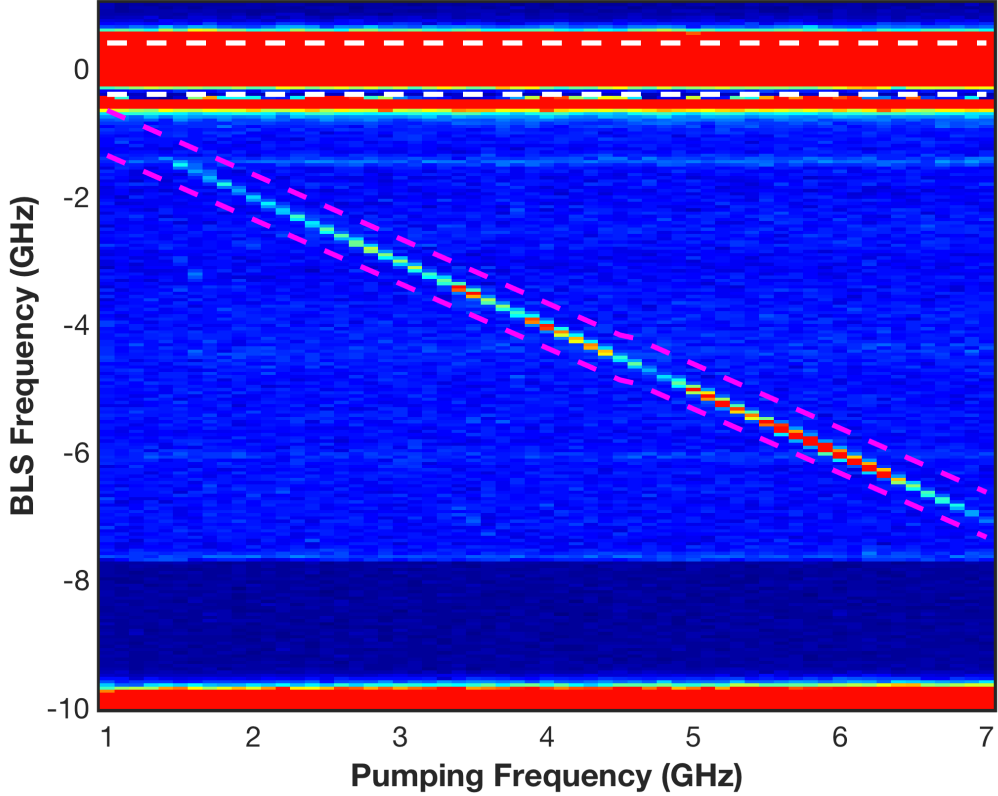


FIGURE 4.5. A characteristic complex frequency scan. A vertical slice corresponds to one individual BLS spectrum (for one specific pumping frequency). The white horizontal lines indicate the integrated portion of the reference peak used to normalize the data. The red slanted lines show the integration region for the pumped spin wave signal. This particular scan is at the top and center location of an AV state with the dynamic field direction as defined Fig. 4.3.

include weak activity just below 3 GHz, most notably at 2.8 GHz, a broad response from 3.9 to 4.5 GHz that shows peaks at 4.0 and 4.3 GHz, and peaks at 5.2 and 6.2 GHz that blend in with the stronger resonance at 5.9 GHz. A complete summary of modes for this chapter is provided in Appendix A.

The saturated configurations also exhibit activity within multiple frequency ranges. The Sat_\perp state shows activity in the range of 1.5-2.5 GHz with a peak at 2.3 GHz, from 3.9 to 5.3 GHz with peaks at 4.6 and 5.1 GHz, and broad activity above 5.3 GHz that tapers off above 6 GHz and shows a strong peak at 5.7 GHz that is close in frequency to the 5.9 GHz

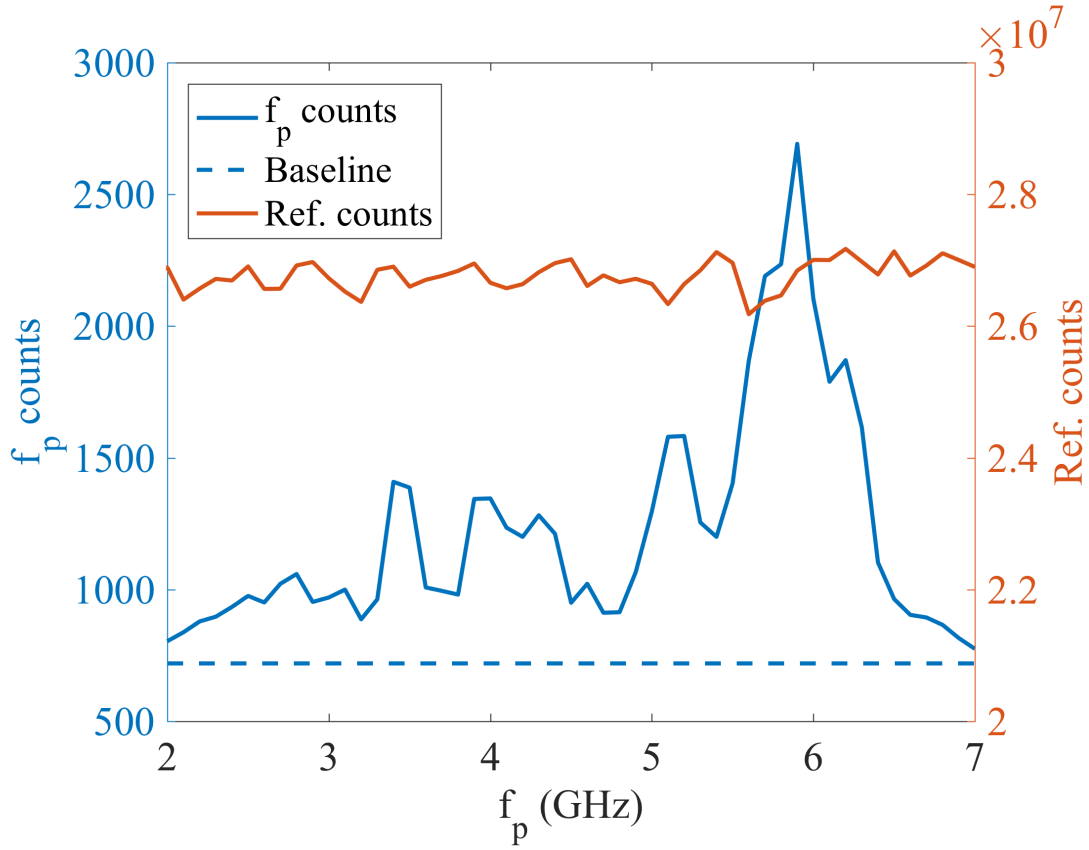


FIGURE 4.6. A characteristic comparison between the reference peak and an extracted pumped BLS signal. The laser fluctuates very little over the course of the scan. This data was extracted from the Stokes side of the spectrum because the negative frequencies had a larger signal above the noise level. The noise level is indicated by the horizontal dashed line and was around 720 counts.

peak observed for the AV state. The Sat_{\parallel} state shows an almost identical response to Sat_{\perp} above 5.3 GHz, but comparatively little activity at lower frequencies with weak peaks at 4.1 and 4.7 GHz and considerably reduced signal below 2.8 GHz, suggesting that much of the Sat_{\perp} signal observed in the low-frequency range is related to the intersection rather than the leg regions indicating that there is very little coupling to the propagating leg modes. Here, the measurements conducted on the saturated state are mainly used to compare with the response of the AV state; a detailed examination of the resonances of the saturated states is beyond the scope of this thesis.

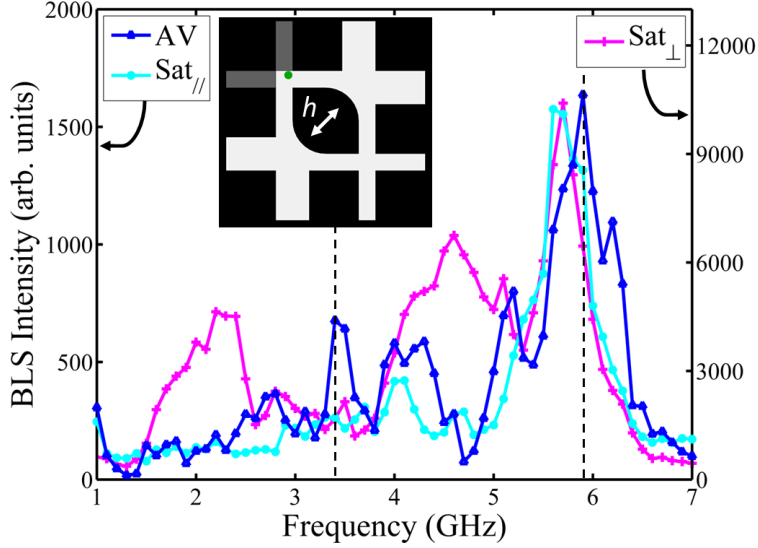


FIGURE 4.7. BLS intensity as a function of f_p measured within the intersection regions of the pound-key-like structures. Data are shown for intersections in the AV, Sat_{\parallel} , and Sat_{\perp} states. The inset illustrates the position of the laser spot (shaded green spot), which is displaced from the center of the intersection towards one of the outer legs. The dashed lines at 3.4 and 5.9 GHz show the frequencies at which spatial scans were obtained (Fig. 4.8).

4.4.1.2. *2D position scans.* For key frequencies of interest, spatial mode profiles were measured by raster scanning over each intersection with the pumping frequency set to the frequency of the mode of interest. The maps were made by integrating all the BLS photon counts over a range of 1 GHz centered on the pumping frequency at each location and normalizing to the reference peak to account for any fluctuation in the laser intensity. Then the regions with the highest intensity correspond to the regions with the highest spin wave amplitude for a given mode. Figure 4.8 shows the normalized BLS intensity as a function of position for a $1.2 \times 1.2 \mu\text{m}^2$ square that is slightly larger than the intersection region, as illustrated in Figs. 4.8(a), 4.8(d), and 4.8(g), for two of the prominent modes observed in Fig. 4.7, one at 3.4 GHz and the other at 5.9 GHz. The former was chosen since the frequency scans indicate that at 3.4 GHz the AV shows a strong resonance while the other states exhibit proportionally less activity, and 5.9 GHz was chosen since the most prominent

mode for all three states occurs at or close to this frequency. The spatial profiles obtained at 3.4 GHz are different for all three states. For the AV (Fig. 4.8(b)) the largest signals are observed near the center of each of the four sides of the intersection region. The mode shows quasi-fourfold symmetry in that the shapes of the intensity profiles on each of the four sides are similar. The peak intensities in the different quadrants do, however, differ significantly. This may be due to the fact that the inner and outer legs have different lengths, which could lead to an asymmetry in the resonance. The Sat_{\parallel} state (Fig. 4.8(e)) shows little signal, whereas a large, slightly off-center signal is observed within the intersection region for Sat_{\perp} (Fig. 4.8(h)) that corresponds to the region where the spins are mainly perpendicular to h . Both Sat_{\parallel} and Sat_{\perp} show some intensity within each of the legs, but the signal is farther from the intersection as compared to that observed for the AV. At 5.9 GHz, the mode profiles observed for the AV, Sat_{\parallel} , and Sat_{\perp} states (shown in Figs. 4.8(c), 4.8(f), and 4.8(i), respectively) are similar in that they exhibit a strong response near the legs and a lesser response within the intersection that is strongest for the Sat_{\perp} state.

4.4.1.3. *Compare with simulations.* In this section we will compare the micro-BLS experimental data with both micromagnetic simulations as well as dispersion curves calculated for the adjacent microstrip legs. The simulations were performed on the GPU-based open source simulation package MUMAX3.

Micromagnetic simulations were performed for a structure with the same geometry and dimensions as used in the experiments ($12 \times 12 \mu\text{m}^2$ and 37 nm thick) using MUMAX3 [129] to gain additional insight into the observed modes. A discretization mesh of $4 \times 4 \times 37 \text{ nm}^3$ was used with magnetic parameters typical for Permalloy: saturation magnetization $M_S = 8.0 \times 10^5 \text{ A/m}$, exchange stiffness constant $A = 1.3 \times 10^{-11} \text{ J/m}$, gyromagnetic ratio

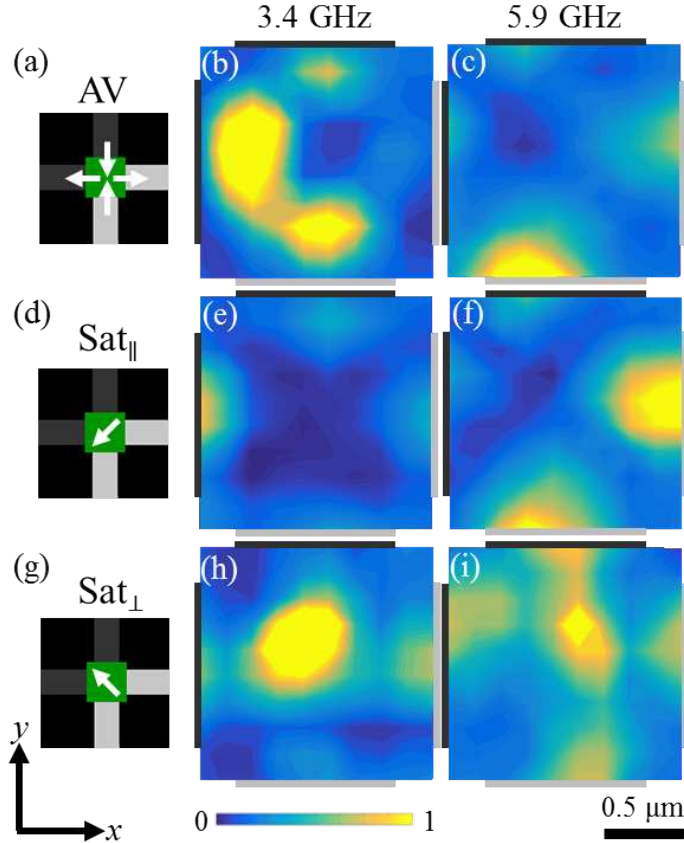


FIGURE 4.8. BLS intensity as a function of position for a 2D grid of 10×10 points obtained over intersections in the (b), (c) AV, (e), (f) Sat_{\parallel} , and (h), (i) Sat_{\perp} states, where h is applied in-plane, along the diagonal, as illustrated in Fig. 4.7. The diagrams (a), (d), and (g) show the scan region (shaded in green), which is slightly larger than the intersection, and the white arrows illustrate the direction of the magnetization for each state. The dark and light gray shading on the diagrams and beside each of the BLS plots is used to identify the outer and inner legs of the structure, respectively, with respect to the scan region. BLS scans are shown for each state for $f_p = 3.4$ GHz in the middle column ((b), (e), and (h)) and $f_p = 5.9$ GHz in the right column ((c), (f), and (i)). Each mode profile is normalized to its maximum value so the color bar represents normalized BLS intensity.

$\gamma = 1.76 \times 10^{11} \text{ s}^{-1}\text{T}^{-1}$, and zero magnetocrystalline anisotropy. Simulations conducted on smaller structures with additional discretization across the sample thickness indicate that a 2D mesh is sufficient to capture the dynamics of interest. An initial state with an AV at one intersection and a saturated configuration at the other was used, which yields a simulated MFM contrast that is in good agreement with Fig. 4.3. The Sat_{\parallel} state rather than the

Sat_⊥ state was chosen for the dynamic simulations because it lacks the high-intensity central mode that is observed for the latter; hence, it provides a more useful comparison to the AV state. The spin configuration was first relaxed to equilibrium with no magnetic field using a damping constant $\alpha = 1$, and then the dynamic response to a Gaussian magnetic field pulse 30 ps in duration (full width at half of the maximum) and 0.1 mT in amplitude was simulated using a realistic damping constant of $\alpha = 0.01$. The pulse was applied in-plane, along the structure diagonal, and the short duration was chosen to suppress the gyrotropic mode in order to focus on the higher frequency dynamics (> 1 GHz). The simulations were repeated at selected frequencies using an in-plane sinusoidal driving field (as in the experiment), which yielded steady state behavior that is essentially the same as the mode maps obtained by cell-by-cell Fourier analysis of the pulsed simulations.

Figure 4.9(a) shows simulated frequency spectra for the AV and Sat_∥ states obtained in response to the in-plane pulsed magnetic field. These spectra represent the amplitude of the Fourier transform of the out-of-plane component of the magnetization M_z averaged over 200×200 nm² subregions that were chosen to approximate the position of the laser spot that was used in the experiment (see the blue and green spots in the inset diagrams). For the AV, notable resonances appear at frequencies of 1.90, 2.22, 3.08, 3.27, and 3.74 GHz. There is also broad activity with multiple peaks over the range from 4.3 to 4.9 GHz, a strong, broad, peak at 5.44 GHz, and a lower amplitude peak at 6.30 GHz. The gyrotropic mode is also weakly excited in the simulations at a frequency of 120 MHz (not shown). Similar to what is observed in the experiments, the Sat_∥ state shows a strong peak at close to, but slightly below, the frequency of the strongest AV peak (5.44 GHz), a general trend of reduced

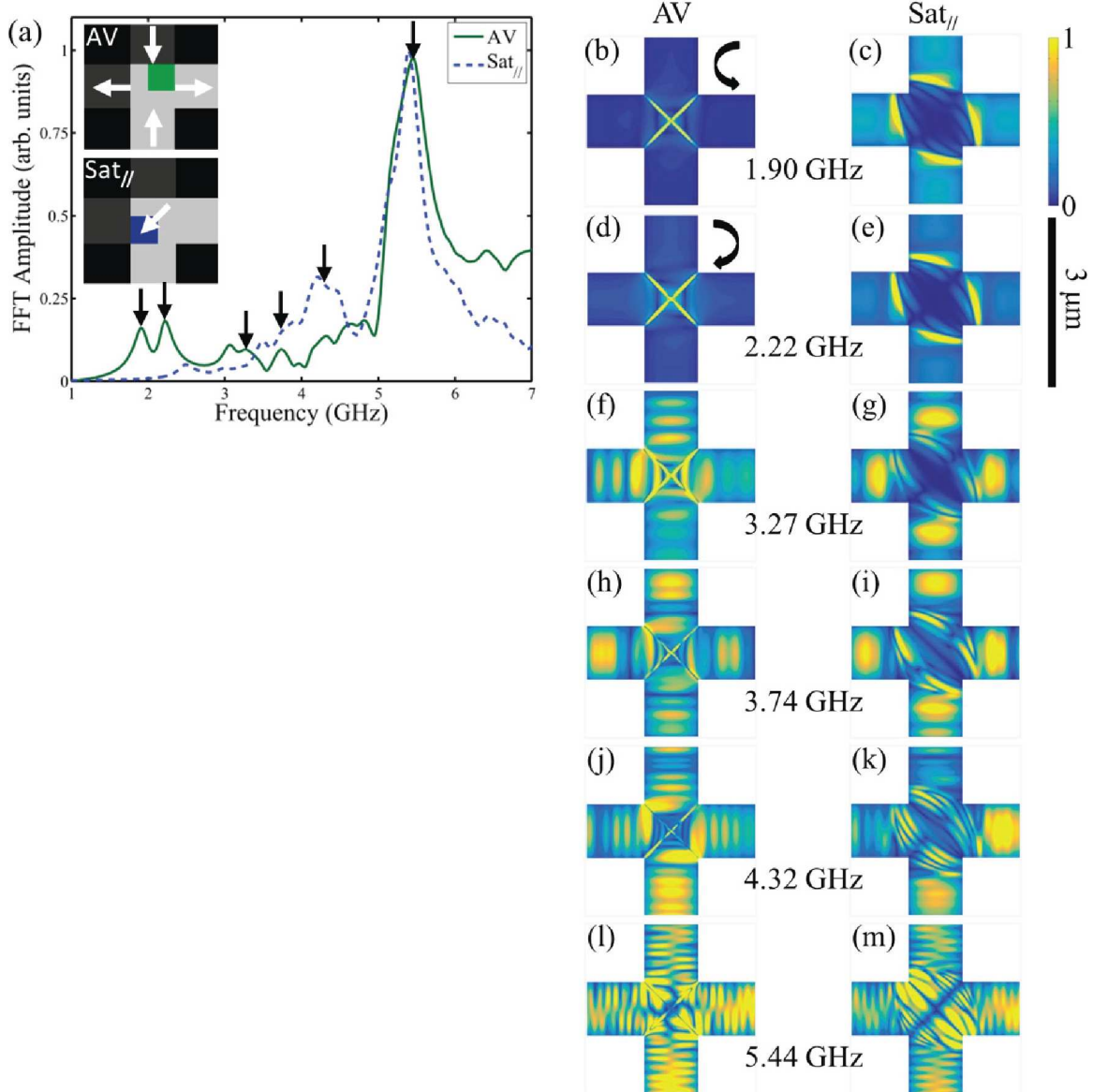


FIGURE 4.9. (a) Frequency spectra and (b)-(m) spatially-resolved mode maps obtained from micromagnetic simulations for intersections that are in the AV (left) and Sat_{||} states in response to an in-plane magnetic field pulse applied along the structure diagonal. The frequency spectra shown in (a) represent the amplitude of the Fourier transform of the time-dependent out-of-plane component of the magnetization M_z in each cell, averaged over a $200 \times 200 \text{ nm}^2$ subregion within the intersection (locations marked by squares in the inset). In the inset, the dark and light shading indicates outer vs inner legs of the structure, respectively, and the white arrows illustrate the spin configurations. The mode maps (b)-(m) show the normalized spectral amplitude of M_z for a $3 \times 3 \mu\text{m}^2$ region centered on the intersection.

response with decreasing frequency is observed, and there is essentially no activity below 2.5 GHz.

Calculated mode maps are shown in Figs. 4.9(b)-4.9(m) for several of the prominent AV resonance frequencies where the Fourier amplitudes are shown for the AV and the Sat_{\parallel} states in the left and right columns, respectively. Note that these are mainly off-resonance mode profiles for the saturated states since the frequencies were chosen based on the AV spectrum. Animations of the most prominent modes are included in the supplemental material in Ref. [34]. Two different types of modes are observed for the AV state: those that involve resonances of just the AV region (1.90 and 2.22 GHz), and those that involve activity within both the AV and the legs that extend outward from the central region (>3 GHz). Several modes have both a standing and propagating character where there are simultaneously either breathing-like or circulating modes that are bound within the intersection and propagating spin wave generated in the intersection that propagate outward. In some cases, for example, for the mode at 3.27 GHz, it appears that the AV region may act as the center of radiation for excitations that propagate outward along the legs.

The AV modes observed at 1.90 and 2.22 GHz both have cross-shaped amplitude patterns (Figs. 4.9(b) and 4.9(d)). The wavelength along the diagonal is approximately twice the distance from the corners of the intersection region to the central AV core. These modes circulate around the AV core in the counterclockwise and clockwise directions, respectively, for positive core polarity, and they are similar to the lowest-order ($n = 1$, where n is the mode number) azimuthal modes that are described in Ref. [118] for an astroid-shaped ferromagnet. The Sat_{\parallel} state, in contrast, exhibits weak (low amplitude) standing spin-wave motion at both of these frequencies (Figs. 4.9(c) and 4.9(e)) that occurs mainly in the regions where the

spins tilt as they enter or exit the intersection. The AV modes at 3.08 GHz and 3.27 GHz (Fig. 4.9(f)) are similar to the 1.90 and 2.22 GHz modes in that the highest amplitude response is along the intersection diagonals, except in this case the wavelength along the intersection diagonals is half of what it is for the $n = 1$ case. The modes appear to circulate counterclockwise for the lower frequency of the mode pair and clockwise for the higher, although these modes can also be viewed as involving spin waves that propagate along the diagonal. Either way, the modes have a handedness, and these are the $n = 2$ azimuthal modes. Unlike the $n = 1$ modes, however, the dynamics are no longer confined to just the intersection region—motion is also visible in the legs of the structure. Spin waves are visible in the legs for the 3.08 and 3.27 GHz modes and are stronger for the latter mode. The spin waves along the legs are quantized across the leg width with a single, central antinode ($m = 1$ mode, where m is the integer mode number across the leg width), which is expected for confined microstrips [130]. The wavelength along the legs is approximately $0.32 \mu\text{m}$, slightly smaller than $w/2$, which is the approximate leg-directed component of the wavelength of the $n = 2$ excitation within the AV region. Activity is also evident in the leg regions for the Sat_{\parallel} state except the wavelength is longer, the peak amplitude is farther from the intersection, and the animations show that the direction of propagation is towards the intersection, opposite to that observed for the AV state. This can be understood by considering the properties of the dispersion curves for long microstrips magnetized along their length, the backward volume spin wave geometry, which will be discussed in more detail below.

For the higher-frequency AV modes (3.74, 4.32, and 5.44 GHz) the simulations show increasing activity in the legs, a trend that is also observed in the simulations of the Sat_{\parallel} state at the same frequencies. The wavevector components along the structure legs tend

to increase with increasing frequency and the mode number within the legs also increases with frequency, where $m = 1$ leg modes are observed from 3.1 to 4.3 GHz and at 5.44 GHz the $m = 2$ leg mode dominates. Distinct modes are more difficult to identify in both the frequency spectra and the spatially resolved mode maps for this frequency range (≥ 3.74 GHz). The peaks at 3.74 and 4.32 GHz (Figs. 4.9(h) and 4.9(j)) show motion along the diagonals that is similar to what is observed for the azimuthal modes, but the wavelength is shorter and there is also increased activity between the intersection diagonals. For these modes as well as the 5.44 GHz mode (Fig. 4.9(l)), the highest amplitude motion within the intersection occurs near the two corners at the top left and bottom right, where the motion in these regions is 180° out of phase across the diagonal (see animations), which is related to the symmetry of the spin distribution and the direction of the excitation field.

4.4.1.4. *Discussion.* The modes observed experimentally at 3.4 and 5.9 GHz (Fig. 4.8) are closest in frequency to the simulated modes found at 3.27 and 5.44 GHz (Figs. 4.9(f) and 4.9(l)), respectively. Since the BLS is sensitive to wave vectors associated with features with spatial wavelengths of $\approx 0.3 \mu\text{m}$ or larger, the finer details near the AV core and near the corners are not expected to be resolved by the experiments, hence the main symmetries of the experimental AV modes shown in Figs. 4.8(b) and 4.8(c) are in reasonable agreement with the simulated modes shown in Figs. 4.9(f) and 4.9(l), respectively. In general, a number of closely spaced modes with complex spin distributions are observed in the higher-frequency range, so it is more difficult to identify the exact mode associated with the 5.9 GHz experimental resonance, however, the peak in the simulations at 5.44 GHz and in the experiment at 5.9 GHz are similarly strong features in the frequency spectra (Figs. 4.9(a) and 4.7, respectively). Furthermore, at 5.44 GHz, the AV and Sat_\parallel states (Figs.

4.9(l) and 4.9(m)) both show similar behavior in the leg regions, and both states also have mainly short-wavelength activity in the intersection that may lead to a lower BLS signal in this region. In the simulated Sat_{\parallel} response at 3.27 GHz (Fig. 4.9(g)), the area of main activity is shifted further down the legs as compared to the AV response (Fig. 4.9(f)) in agreement with experimental observations at 3.4 GHz (Figs. 4.8(e) and 4.8(b)), and there is an asymmetry in the intensity distribution of the simulated AV mode that is similar to what is observed experimentally. Additional simulations show that the corresponding AV mode takes on a symmetric shape in a symmetric cross structure, suggesting that the observed mode asymmetry is caused by the structure shape.

The simulated AV frequency spectrum shows additional features at lower frequencies, and while some are similar to the experimental measurements shown in Fig. 4.7, there are also differences. The broad peaks observed in the experiments at 4.0 and 4.3 GHz are similar in frequency and form to the simulated peaks at 3.74 and 4.32 GHz, respectively. There are several additional peaks in the simulated frequency spectrum at the other azimuthal mode frequencies (1.90, 2.22, and 3.08 GHz) that are more prominent in the simulations than in the experiments. There is a weak peak in the experimental AV spectrum at 2.8 GHz that may correspond to the lower-frequency $n = 2$ azimuthal mode (3.08 GHz in the simulations). There are no particularly prominent features in experimental AV spectrum below 2.8 GHz, however, additional frequency scans conducted at several other points within the intersection show stronger activity at 2.9 GHz as well as two additional peaks at 1.7 and 2.3 GHz (not shown), suggesting that the reason that the lower frequency azimuthal modes are difficult to identify in Fig. 4.7 is likely due to spatial variations of the signal within the structure.

For magnetic vortices, two main types of dynamic modes are observed at frequencies above the gyrotropic resonance (>1 GHz), modes with radial [110, 111] and azimuthal [131] symmetries, whereas for in-plane magnetized wires, the spin excitations are often discussed in terms of backward volume (BV) versus Damon-Eschbach (DE) modes, where the magnetization is along the wire (and parallel to the spin-wave wave vector) for the former and perpendicular for the latter. Simulations of the AV dynamics in astroid-shaped structures have been classified in a similar manner where the “radial” modes are standing spin-wave excitations and the “azimuthal” modes have some propagating character [118]. Unlike the astroid geometry considered in Ref. [118], an AV in a pound-key-like structure is connected to extended microwires. In the pound-key-like structures, the magnetization direction extends smoothly from the AV core and into the legs, so it is possible to have BV-type excitations that will propagate along the legs. In the legs, the wave vectors of the spin waves observed in the simulations are quantized across the leg width, which is expected for magnetic microstrips [130, 132], where one ($m = 1$) and two ($m = 2$) antinodes are observed in Figs. 4.9(f)-4.9(k) and Figs. 4.9(l) and 4.9(m), respectively. BV dispersion curves calculated using Eq. (24) in Ref. [132] yield wavelengths along the wire of $\lambda = 0.32 \mu\text{m}$ ($k = 20 \mu\text{m}^{-1}$) and $\lambda = 0.15 \mu\text{m}$ ($k = 42 \mu\text{m}^{-1}$) for one antinode at $f = 3.27$ GHz and two antinodes at $f = 5.44$ GHz, respectively, both of which are close to the values observed in the simulations of $\lambda = 0.35$ and $0.15 \mu\text{m}$, respectively. The wavelengths of the spin waves were determined from plots of the amplitude and phase. Note that the minimum frequency allowed by the dispersion curves occurs at 3.1 GHz, which explains why no significant activity is observed in the legs for either state at 1.90 or 2.22 GHz.

At 3.27 GHz, the Sat_{\parallel} state shows a longer wavelength (compared to the AV state) along the legs of $\lambda \approx 1 \mu\text{m}$ and, as mentioned previously, the propagation direction is inward, opposite to that observed for the AV state. The wavelengths listed above are obtained from the higher wavevector portion of the dispersion curve where exchange dominates and the spin wave group velocities are positive, however, BV spin wave dispersion curves first decrease and then increase with the wave vector. Consequently, there is another possible wave vector in the lower- k region, which is $\lambda = 0.62 \mu\text{m}$ ($k = 10 \mu\text{m}^{-1}$) at 3.27 GHz, and this corresponds to spin waves with a negative group velocity. Hence, the larger wavelength and the difference in the propagation direction observed for the Sat_{\parallel} state are also consistent with expectations based on calculated dispersion curves. It is interesting that the different spin configurations within the intersection lead to quite different dominant leg modes for the same excitation frequency. Microstrip antennas have limited efficiency for exciting $\lambda < d/2$, where d is the antenna width [133], which places practical limitations on the smallest wavelengths that can be easily excited. Not only do AVs exhibit dynamics that are quite different than the reported modes of a magnetic vortex, but the coupling between the AV modes and leg modes may also offer an alternative means to excite small- λ spin waves. Not only can these waves be generated but the user can determine which leg-width mode will be excited by toggling the magnetic state in the intersection (from AV to Sat or back).

4.4.2. OUT-OF-PLANE EXCITATION. Now that we have explored the dynamic response of an AV to an in-plane excitation, we will look at its response to an out-of-plane excitation. A uniform OOP excitation will not exert a displacing force on the AV core so the gyrotropic mode will not be directly driven. Also, because the OOP excitation is uniform over the intersection, modes with azimuthal symmetry are expected to be suppressed. Thus the main

dynamic modes of an AV with OOP excitation are expected to exhibit radial-type symmetry, where the wavevectors are directed predominantly outward or inwards from the core.

4.4.2.1. *Frequency scans.* Frequency scans were performed at two locations within the intersections containing the AV and Sat states as indicated by points A and B in the inset in Fig. 4.10. The frequency was swept from 3-8 GHz in steps of 100 MHz while keeping the power constant. These scans reveal the response of the two magnetic states to the out-of-plane dynamic field. Both states show a large peak above 6 GHz without much activity at other frequencies. There is perhaps some evidence of other modes in the AV state but they are obscured by the noise. The most prominent mode of the AV occurs at a higher frequency (6.6 GHz) than in the intersection containing the Sat state (6.2 GHz). The responses of the AV at points A and B show quite distinct character. At point A, two small resonances are observed, one between 6.3 and 6.4 GHz and the other at 6.9 GHz, while point B shows one large resonance at 6.6 GHz and two small shoulders at 5.9 GHz and 6.3 GHz. The Sat state frequency response is essentially the same at both locations with a large resonance at 6.2 GHz and without any other significant peaks. The difference in the shape of the prominent mode at points A and B for the AV state indicate that the AV response has a more complicated dependence on position compared with the uniformity of the Sat state which is similar to the results observed at both positions under in-plane excitation. Much shorter frequency sweeps were run between 1-3 GHz but no modes were observed above background for either state. There is an increased background signal in this frequency range since it is closer to the elastic peak of the BLS and the lowest-order radial mode that is expected to be within this range involves spin excitations over a very small spatial extent, which also makes it difficult to detect.

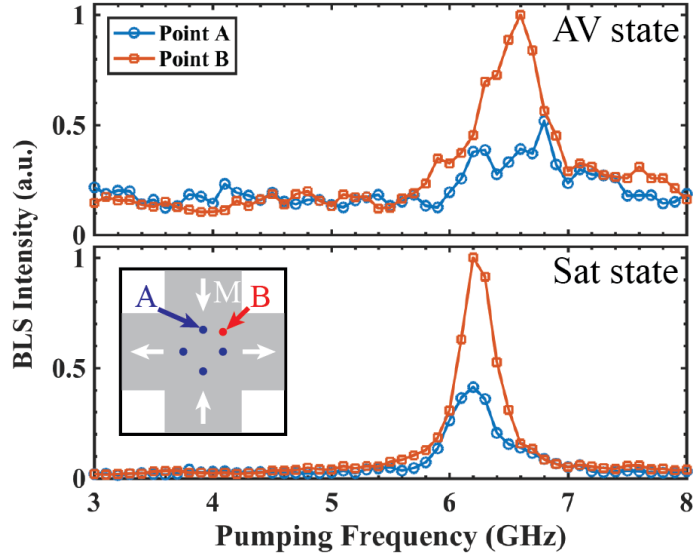


FIGURE 4.10. BLS intensity as a function of pumping frequency for two positions on an antivortex state (top) and saturated state (bottom) in a Permalloy microstructure under the influence of an out-of-plane dynamic field. The inset indicates the two positions (A and B) where the dynamic response was measured. The difference between the frequency sweeps in the top figure also indicates that the shape of the AV absorption depends on the location of the measurement, whereas the Sat state response has a similar shape at both points with only a difference in intensity.

4.4.2.2. *2D position scans.* In order to learn about the spatial profile of the most prominent mode, 2D position scans were performed on both the AV and Sat states as shown in Fig. 4.11. Both scans were performed at a constant frequency corresponding to the peak frequency of the AV state (6.6 GHz, the largest observed amplitude for the AV) over a region of 6 by 10 steps with a step size around 150 nm that corresponds to a region slightly larger than the intersection ($0.9 \times 1.5 \mu\text{m}^2$). Both states show a rough four-fold symmetry. The Sat state shows much higher intensity in absolute photon counts and seems to have the highest activity near the center of the intersection, which is representative of a bulk-type mode (as opposed to an edge mode). Although, as for the in-plane case, the resonance peak is closer to one side of the intersection than the others. The AV state shows a response that is spread more broadly within the intersection and that extends into the legs. The broad response is

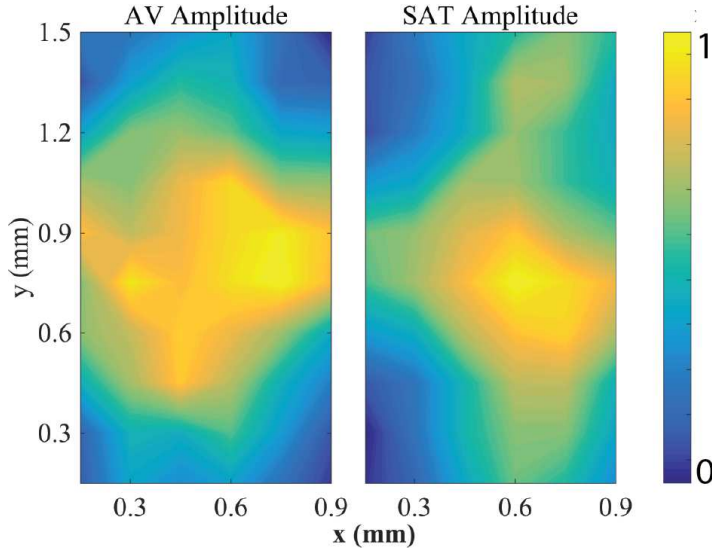


FIGURE 4.11. BLS intensity as a function of position over the intersections containing the antivortex state (left) and saturated state (right) under the influence of an out-of-plane dynamic field. The color scale is normalized to the max and min values of each state; the Sat state has much higher intensity. The directions x and y are defined by the black arrows in Fig. 4.4. Both measurements were performed with $f_p = 6.6$ GHz, the peak resonance of the AV state.

not symmetric with respect to the intersection which is similar to the asymmetry observed for the AV driven in-plane at 3.4 GHz as shown in Fig. 4.8b. The micro-BLS is a diffraction limited measurement with a resolution just below 300 nm so these 2D spatial maps represent a slight oversampling. The limited resolution imposes a blurring effect on modes with sub-resolution features. A comparison with micromagnetic simulations is discussed in the following section.

4.4.2.3. *Compare with simulations.* Micromagnetic simulations under the same conditions reported in Section 4.4.1.3 were performed except now with a geometry that more closely represented the sample studied with the OOP excitation. For the simulations, a structure with dimensions of $2L = 11$ μm and $w = 500$ nm was used. Figure 4.12 shows the frequency response averaged over all the cells in the intersection for both the AV and Sat

states. Similar to the experimental data we see a large response for both states at frequencies (> 6 GHz) with lower activity at lower frequencies (<6 GHz). We see further agreement in that the peak AV response occurs at a higher frequency than the peak response of the Sat state. We do note, however, that there is a discrepancy between the peak frequencies in the experiment compared with the simulations. A possible reason for the upshift is the fact that the size of the structure used in the calculation does not perfectly match that used in the experiment. The structures are close enough in size that we expect that the main features of the spectrum and mode profiles will be preserved, just shifted in frequency. In the simulated AV spectrum the most prominent peak occurs at 7.6 GHz and has two shoulders at 7.2 GHz and 8.5 GHz. One prominent mode low frequency mode is observed at 2.4 GHz which was not observed in the experimental data but corresponds to a mode with radial behavior as verified by the reconstructed mode profile maps discussed next. The Sat state shows one large shoulder-free peak at 7.2 GHz and more complicated behavior at lower frequencies with low amplitude peaks at 2.7 GHz, 3.7 GHz, and 4.6 GHz that are not discussed here because the behavior of the Sat state is beyond the scope of this study. The AV peak at 7.6 GHz is the closest qualitative match to the peak observed in the BLS frequency swept data at 6.6 GHz.

Further characterization of the prominent modes is provided by simulated 2D spatial mode maps obtained following an identical process to what was discussed in Section 4.4.1.3. Figures 4.12b and 4.12c show mode maps for both states that correspond to the most prominent frequency of the Sat state (7.20 GHz). At this frequency, the AV state has an intricate pattern response with $n=2$ leg quantization. The Sat state response is stronger at this frequency and it couples to an $n=1$ width quantized mode in the structure legs. At 7.59 GHz,

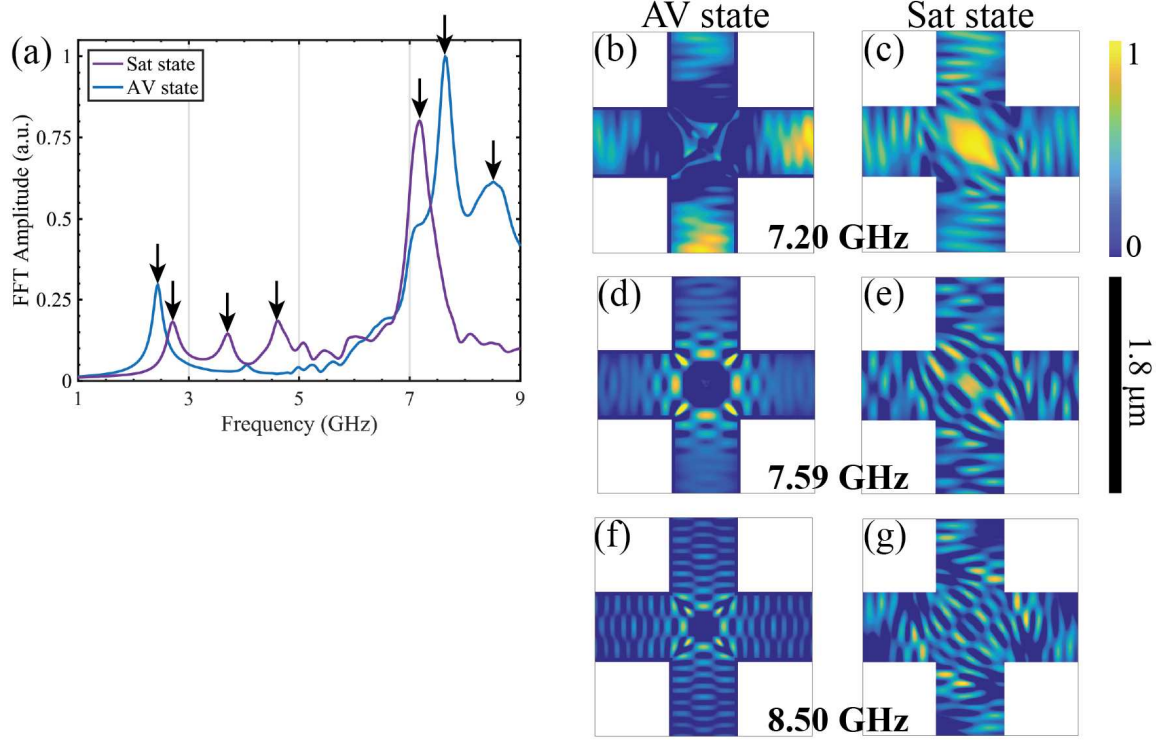


FIGURE 4.12. (a) Frequency spectra and (b)-(g) spatially resolved modes obtained from micromagnetic simulations for intersections that are in the AV (left) and Sat (right) states in response to an out-of-plane magnetic field. The frequency spectra shown in (a) represent the amplitude of the Fourier transform of the time-dependent out-of-plane component of the magnetization M_z in each cell, averaged over a $200 \times 200 \text{ nm}^2$ subregion within the intersection. The mode maps (b)-(g) show the normalized spectral amplitude of M_z for a $3 \times 3 \mu\text{m}^2$ region centered on the intersection.

which corresponds to the highest amplitude mode of the AV, we see a four-fold symmetric mode profile for the AV (Fig. 4.12d) with a combination of $n=1$ and $n=3$ quantization in the legs. At this frequency, the Sat state (Fig. 4.12e) has a complicated pattern in the intersection but couples to an $n=3$ width-quantized leg mode. Figs. 4.12f and 4.12g are mode maps for the frequency corresponding to the second most prominent mode in the AV spectrum. Again, we see a distinct four-fold symmetry in the intersection that couples to an $n=3$ mode in the legs. The Sat state does not have well-defined activity at this frequency but may have some weak coupling to an $n=2$ leg mode. A closer look at the corresponding

phase maps for each mode reveals that a majority of the excited modes do have a radial-like symmetry in that the phase of the excitation is uniform around the intersection for a given distance from the intersection center. The shape of the frequency spectrum for the AV state and the four-fold symmetry observed for the most prominent mode are consistent with the experimental results. Furthermore, the shift in the peak frequencies found in the simulation and experiment for the peak Sat vs. AV modes are: 390 MHz and 400 MHz, respectively, which are similar in magnitude. The highest-amplitude mode for the Sat state has a lower order leg quantization ($n=2$) as compared to the highest-amplitude mode for the AV state which has a higher order leg quantization ($n=3$) that mirrors the symmetry of the AV intersection mode. Thus the order of quantization of the propagating spin waves can be controlled by toggling the magnetic state within the intersection. It was surprising that the lower frequency modes were not observed with the BLS measurements, however, most of the modes seen in the simulations for the AV from 2.5 - 6 GHz are very low amplitude. Below 2.5 GHz the background is larger and hence small signals are more difficult to detect.

4.5. SUMMARY

In summary, micro-BLS measurements of the dynamics of a magnetic AV stabilized in a patterned microstructure show a rich excitation spectrum. Micromagnetic simulations indicate that AVs exhibit modes that have both standing and propagating characteristics, and that the seamless transition from the AV spin configuration into the saturated legs of the structures used for this study leads to modes that originate in the AV region and propagate along the legs. The in-plane excitation showed that one of the leg-coupled azimuthal modes found in the simulations occurs at a similar frequency and possesses a similar spatial amplitude profile as compared to a strong resonance observed experimentally for the AV

state. The out-of-plane excitation showed a frequency shift between the peak modes of the AV and Sat states that had almost perfect agreement with the simulations. With these structures, it is possible to toggle the magnetic state to shift the absorptive frequency of the magnet which could be useful as a filter device. Both the simulations and experiments show that the dynamic modes of an AV are more complex than those of a vortex, but the unique topology of the AV state shows an intriguing potential for the generation of propagating short-wavelength spin waves that may be of interest for magnonics applications. Portions of the in-plane AV data presented in this chapter have been published in Physical Review B [134] and the out-of-plane data is in preparation for publication at the time of this writing.

THERMAL CONTROL OF SPIN WAVES

5.1. MOTIVATION

Recent progress in spin caloritronics has motivated the study of the interplay between spin waves and non-uniform thermal profiles [135–138]. Previous studies on the behavior of spin waves in the backward volume geometry [139] showed that the wavelength of spin waves propagating in a yttrium iron garnet (YIG) film becomes progressively shorter as the waves travel into a cooler region of the sample. The observed wavelength shift, measured using phase-resolved Brillouin light scattering (BLS), agrees well with a model that assumes that the primary effect is that of an increase in the saturation magnetization M_S of the YIG with decreasing temperature [140]. As the spin waves propagate, the frequency remains constant but the component of the wavevector along the direction of the thermal gradient changes to accommodate the change in M_S , much the same as what happens with light in an optical element with a graded index of refraction.

Strategies for controlling spin wave propagation by using a spatially varying dispersion may be useful in devices. In one case a spin wave interferometer was realized by utilizing a gradient in the magnetic field [141]. More recent experiments have also shown, again demonstrated in YIG, that thermal effects can be used to create reconfigurable lenses that can focus, defocus, or redirect spin waves depending on whether the spin waves are surface waves, backward volume waves, or caustic beams [142, 143] and spatially-resolved measurements made using an inductive probe in a surface wave configuration showed increased amplitude for a spin wave pulse that traveled towards a warmer region, which was attributed to a slowing of the group velocity at the pulse leading edge and consequently a compressional

gain effect [144]. These studies highlight the fact that the interplay between thermal effects and spin waves can lead to unusual and potentially useful effects.

5.2. EFFECTS OF THERMAL PROFILES ON SPIN WAVE DYNAMICS

If we consider spin waves that travel through a changing thermal profile without being annihilated by one of many possible damping mechanisms, the energy must be conserved and therefore the frequency will remain constant. The saturation magnetization will decrease with increasing temperature, which causes a downward shift of the entire dispersion manifold. Taking iso-frequency cuts through the dispersion surfaces at each temperature then gives the allowed wavevectors at a given frequency. If a linear thermal gradient is used, we expect the component of the wavevector pointing along the direction of the gradient to be modified with temperature. However there is nothing to break the symmetry in the direction perpendicular to the gradient so momentum and therefore also the component of the wavevector perpendicular are conserved. This gives a straightforward method for determining the predicted wavelength change from the dispersion surfaces. First obtain the slowness curves, or allowed wavevectors, by taking iso-frequency cuts of the dispersion surfaces at each temperature. Then for each value of the wavevector perpendicular to the thermal gradient, in this example k_y , it is possible to follow the shift in k_x in the slowness curves. From this we can calculate the predicted change in wavelength for a given distribution of wavevectors.

In this chapter we present time resolved-Brillouin light scattering (TR-BLS) measurements to explore the interplay between a thermal gradient and pulsed spin wave beams traveling in a surface wave geometry in a thin YIG film. Spatially resolved TR-BLS measurements show that even modest thermal gradients can lead to observable changes to the beam angle, pulse shape, and 2D mode profiles. Interestingly, even though the thermal

gradient applied was linear, the modifications imposed by the changing temperature were notably non-uniform as a function of distance.

5.3. EXPERIMENTAL SETUP

In this work, we demonstrate the possibility of controlling spin wave propagation in a magnetic insulator under the influence of a non-uniform thermal profile. The material under study is yttrium iron garnet, $\text{Y}_3\text{Fe}_5\text{O}_{12}$ (YIG), a common material used to study spin wave dynamics because of its very low intrinsic damping, which allows spin wave signals to propagate over long distances (centimeters) before they decay [145]. This sample was grown via liquid phase epitaxy atop a gadolinium gallium garnet a $\text{Gd}_3\text{Ga}_5\text{O}_{12}$ (GGG) substrate that was 0.4 mm thick. The dimensions of the sample were 1.9 mm wide by about 4 cm long and with a thickness of 6.3 μm . All of the measurements were performed with the magnetization of the film saturated parallel to the excitation antenna and perpendicular to the long axis of the film (as shown in Figure 5.1) in the Damon-Eshbach geometry.

The spin waves were generated using CW microwave pulses in order to perform time-resolved Brillouin light scattering analysis in a pump-probe style measurement. The microwave excitation was delivered through a surface-mount microstrip antenna in order to provide a dynamic excitation field in the plane of the sample and oriented parallel to the long axis of the film. In this configuration, the most significant portion of the dynamic field is perpendicular to the static magnetization and thus provides the maximum amount of torque to drive precession of the magnetic moments under the antenna and initiate oscillation. Two such microstrip antennas were used in a delay-line configuration, one as the input transducer and one after the BLS scan range and also after the heat source to analyze the final microwave output as shown in Figure 5.1. Both antennas had a width of $d = 50 \mu\text{m}$, which

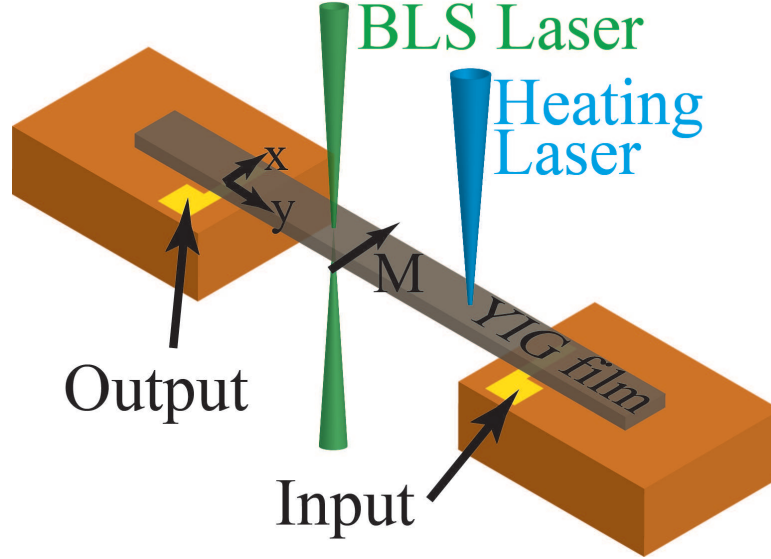


FIGURE 5.1. Illustration of the experimental setup used in this study. The YIG sample was saturated in the DE geometry and spin waves were generated by an input microstrip antenna. The thermal gradient was generated by a blue (445 nm) CW diode laser focused just outside the BLS scan range. The BLS probe was focussed on the YIG layer and raster scanned over the surface.

allows for efficient excitation and detection of magnetostatic spin waves with wavevectors of up to approximately $|\mathbf{k}_{max}| = \pi/d = 630$ rad/cm and spin waves are excited up to 1200 rad/cm with diminishing efficiency.

A temperature profile was generated using a blue (445 nm) CW laser with an elliptical spot size of 1 mm \times 2 mm incident on the surface of the film 8 mm away from the input antenna as shown in Fig. 5.1, which is just outside the BLS scan region. This wavelength was chosen because it corresponds to a region of strong optical absorption in YIG [7]. The power of the heating laser at the sample surface was approximately 80 mW, which provided an almost linear thermal gradient along the long axis of the film with a difference of 4 K over

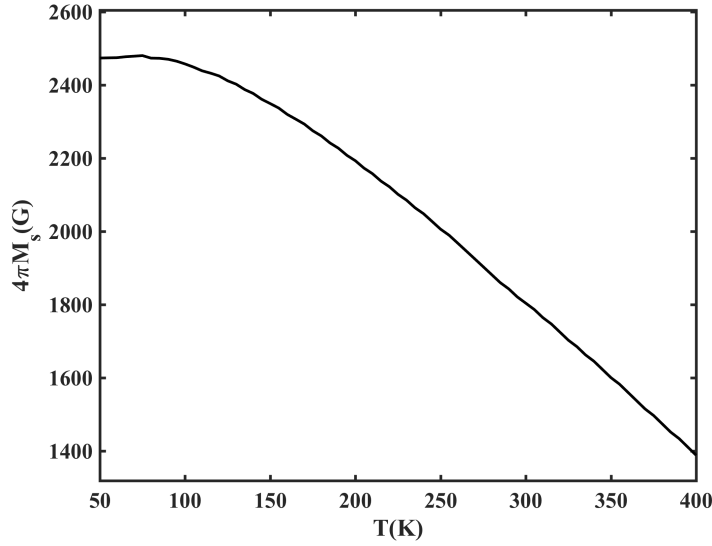


FIGURE 5.2. $4\pi M_S$ measured as a function of the temperature using SQUID magnetometry with a field of $H = 200$ Oe used to saturate the sample in plane.

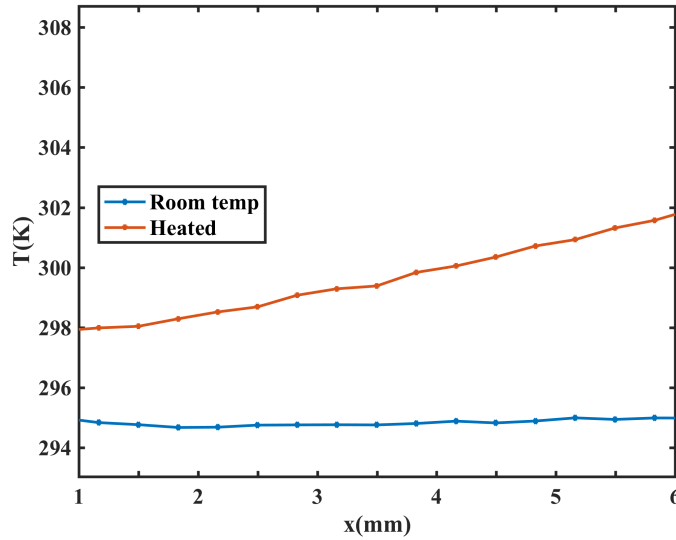


FIGURE 5.3. The width-averaged temperature profile of the film as a function of distance from the input antenna x , measured with a FLIR A300 thermal camera assuming an emissivity of 0.75 for YIG. A linear change in temperature with a difference of 4 K for the heated sample over the BLS scan range was observed.

the BLS scan range as measured with a thermal camera (data shown in Fig. 5.5 leading to a thermal gradient of $\nabla_x T = 0.8$ K/mm within the scan region. The temperature was relatively uniform across the width of the film with a mean variation 0.8 K in the y direction. The

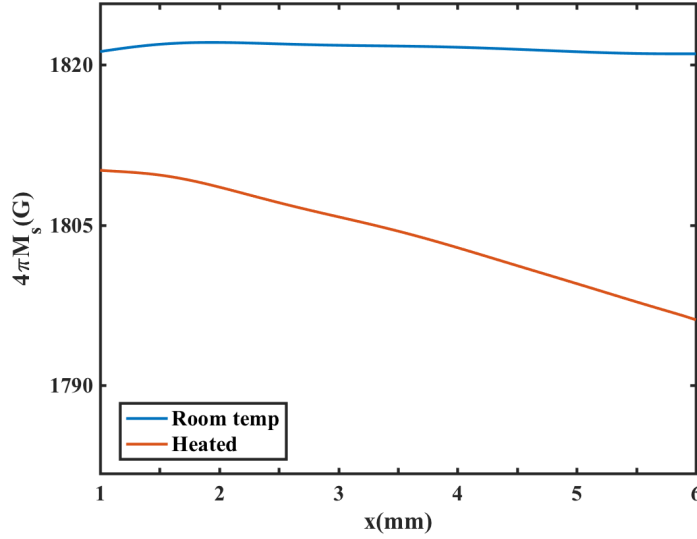


FIGURE 5.4. $4\pi M_S$ as a function of distance from the input antenna.

laser was cycled on and off more than three times while recording a video with the thermal camera. About 5 minutes were required for the sample to reach a steady state temperature profile. The steady state thermal gradient was identical after each heating cycle, hence the temperature profile was repeatable. Fits to ferromagnetic resonance measurements [14] made at frequencies from 13 to 17 GHz with the field applied in-plane yield a saturation magnetization of $4\pi M_S = 1821 \pm 3$ G at room temperature ($T = 295$ K). Figure 5.3 shows the temperature dependence of $4\pi M_S$, which was measured by SQUID magnetometry where the magnetic moment of the GGG substrate was subtracted from the data. Figure 5.4 shows $4\pi M_S$ as a function of position for the heated sample, obtained by combining the data shown in Fig. 5.2 and 5.4.

Brillouin light scattering was used to detect spin waves in the region between the antenna and heating laser in a forward scattering geometry. A Coherent Verdi V5 DPSS laser with a wavelength of 532 nm was used for the BLS measurements. In BLS spectroscopy the light scatters inelastically from spin waves in the sample and the resulting frequency shift of the

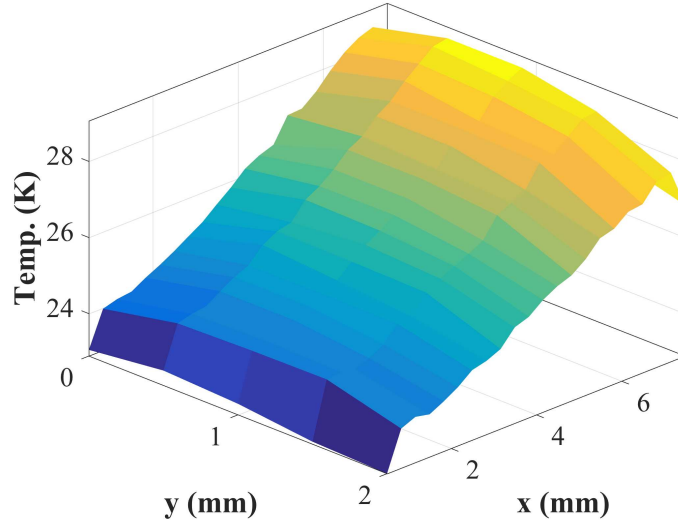


FIGURE 5.5. Temperature profile of the film as measured by a thermal camera. A 4 K temperature increase was observed along the length of the scan region. The temperature is lower on the sample edges by < 0.8 K.

light, measured using a six-pass tandem Fabry-Perot interferometer, is equal to the frequency of the spin waves within the probe laser spot as discussed in Chapter 3. The intensity of the inelastically scattered light is proportional to the square of the out-of-plane component of the dynamic magnetization averaged over the laser spot size, which is approximately $50 \mu\text{m}$ in diameter for these measurements. BLS measurements were made at a fixed position with respect to the antenna as a function of the external static field H and pumping frequency f_p using a CW microwave source, and spatial maps were obtained at selected H/f_p values that correspond to off-axis beam formation by scanning the sample with respect to the probe laser. For the latter, a TTL switch was used to generate a pulse train of microwaves (typically 3-4 GHz) with 100 ns duration and a repetition rate of 500 kHz, chosen to avoid any additional heating effects. The arrival times of the scattered photons with respect to a trigger pulse were measured with a time resolution of 250 ps in a time-of-flight setup. While the time-averaged microwave power was only $p = 0$ dBm for the time-resolved measurements, the

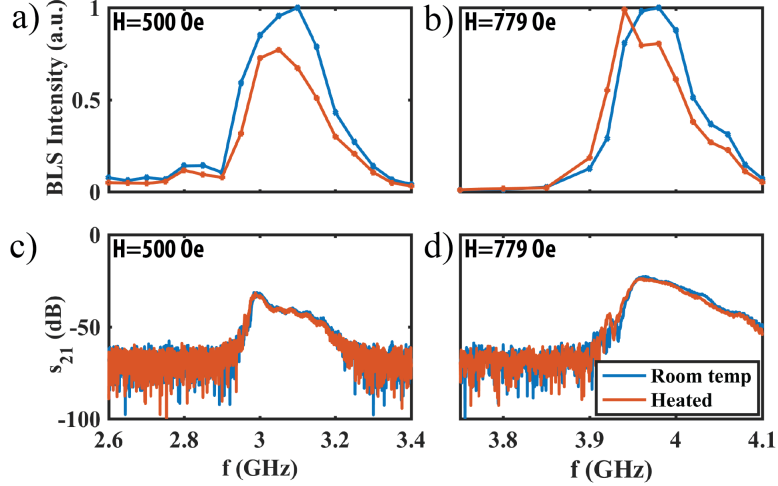


FIGURE 5.6. The BLS intensities at $x = 1$ mm (a and b) and transmitted amplitude measured at the output antenna (c and d) are shown as a function of f for the heated and unheated sample for Oe in a) and c), respectively, and for $H = 779$ Oe in b) and d). The BLS data were collected in the center of the film width and at $x = 1.0$ mm and the BLS intensities were normalized to the peak value of the room temperature BLS intensities. The microwave transmission measurements were made with a separation of 11.2 mm between the input and output antennas.

microwave power during the pulse was $p = 13$ dBm but three-wave nonlinear processes only occur at frequencies below 3.3 GHz for YIG and above this frequency the dispersion curves only permit four-wave nonlinear processes that have a much higher power threshold [146], hence a linear response is expected. The single-position BLS data and time-resolved spatial images were obtained with and without the heating laser. Microwave measurements of the spin wave transmission from the input antenna to the receiver antenna were also conducted and compared to the BLS measurements.

5.4. RESULTS AND DISCUSSION

5.4.1. SPECTRAL PROFILE. Figure 5.6a and 5.6b show the BLS intensity measured with the laser focused at a fixed position of $x = 1$ mm from the input antenna and at the center of the sample width as a function of f_p for $H = 500$ and 779 Oe , respectively, and Figures

5.6c and 5.6d show the corresponding microwave measurements made at the output antenna. The heating leads to noticeable shifts of the BLS intensity profiles toward lower frequencies for the heated sample of approximately 10-20 MHz that are visible in Figs. 5.6a and 5.6b. The observed frequency shift is expected for a slight lowering of the average M_S value due to the heating. At this particular location, the BLS intensity is lower for most of the pumping frequencies when the heating laser is turned on as compared to the unheated case for both H , except for several data points at low frequencies for $H = 779$ Oe where the opposite is true. It will later be shown that even small changes in M_S can lead to significant changes in the beam shape propagation profile indicating that studying just one isolated position can result in drastic changes in intensity and highlighting the need for two-dimensional measurements. The microwave transmission profiles in Figs 5.6c and 5.6d were taken after the focus of the heating laser and integrate the signal across the width of the film. These measurements have the typical profile for a surface wave configuration: an abrupt rise in the transmitted amplitude that corresponds to the frequencies on dispersion manifold with a rapidly increasing number of accessible wavevectors to the peak amplitude slightly above the FMR mode followed by a more gradual decline as the frequency increases that occurs due to the diminishing excitation efficiency of the antenna with increasing wavevector. Microwave measurements on the heated sample show a smaller shift to lower frequencies than in the BLS data but no noticeable change in amplitude. The smaller shift to lower frequencies is expected because the output antenna is measuring the spin waves after they have travelled through the focus of the heating laser into the reversed thermal gradient where the magnitude of M_S increases again but not quite to the level at the input antenna. Previous work has shown that large thermal gradients will lead to an overall reduction in microwave transmission

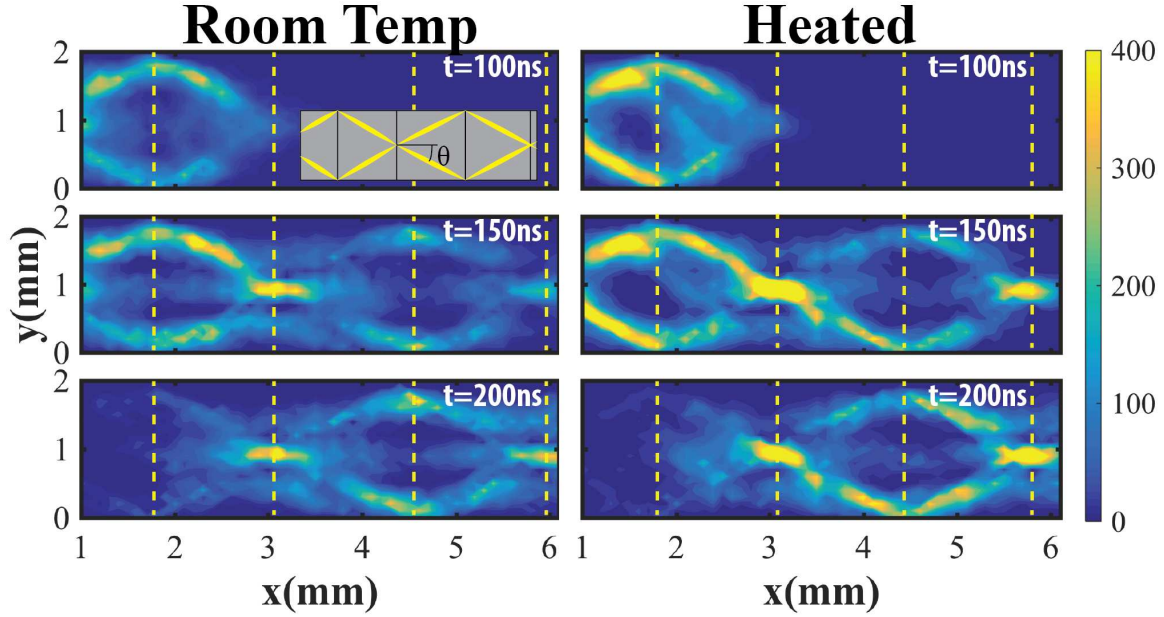


FIGURE 5.7. Two-dimensional TR-BLS scans are shown for selected times at room temperature and with a thermal gradient applied (heated) for a microwave pulse with $f_p = 3.925$ GHz and 100 ns duration with $H = 779$ Oe, conditions chosen to correspond to the largest change in intensity under heating. The intensity scale represents the BLS intensity as the number of integrated counts where the measurement time was the same for all plots. The vertical dashed lines highlight the location of the nodes and turning points in the spin wave propagation profile. The inset shows the definition of the beam propagation angle.

due to spin wave reflection caused by extensive shifts in the dispersion surface that forbid further propagation [139, 144] but in Figs. 5.6c and 5.6d little, if any, change in transmission amplitude is detected for such a small thermal gradient. The fact that the amplitude profile is preserved indicates that almost all the spin waves are able to travel through the hot spot without modified attenuation or reflection.

5.4.2. 2D BLS SCANS. To gain insight into the effects of the thermal gradient on the shape of the propagation profile and intensity variation, two-dimensional TR-BLS scans were performed on spin wave pulses as they travel along the film into the hot region. Figure 5.7 shows TR-BLS scans conducted for $H = 779$ Oe and $f_p = 3.925$ GHz, a frequency that is

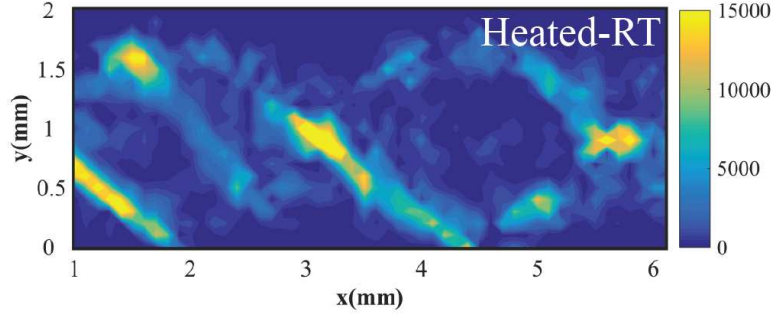


FIGURE 5.8. The difference between TR-BLS data obtained from the heated and room temperature samples at $H = 779$ Oe and $f_p = 3.925$ GHz, integrated over all time for the entire 2D scanned region. The data show differences in intensity at the crossing points of the diamond-shaped propagation pattern and on some of the downward-traveling beam paths, where the heated sample generally shows higher intensities.

just below frequency of maximum signal amplitude in Fig. 5.6b, with and without heating at three time delays. The amplitude represents total photon counts integrated over a frequency range of 1 GHz centered on f_p , normalized to the reference peak. With the time-of-flight detection method, the photons are binned based on their arrival times with respect to a trigger pulse, which provides a means to track the temporal progress of spin waves as they travel through the film. The stages controlling the location of the film under the BLS probe were raster scanned with a step size of 100 μm and the TR-BLS response was recorded at each position. The data shown in Fig. 5.7 were integrated over a time range of $dt = 8$ ns centered on the delay time to increase the signal to noise, which has the effect of smoothing the intensities at the pulse edges but does not affect the observed propagation pattern.

The TR-BLS scans in Fig. 5.7 reveal an intricate diamond-shaped spin wave propagation pattern. The general pattern shape is largely unaffected by the sample heating but there are significant differences in the spin wave intensities at key points in the propagation pattern and the BLS intensities are generally higher for the spin waves that travel into the thermal gradient. It is possible to identify specific points in the 2D spectrum which will have a

dramatic decrease in BLS intensity under heating and other locations with the opposite effect at this frequency, yet the intensity of the shifted diamond pattern is clearly increased and the BLS signal integrated over the film width shows an increase as well. Furthermore, the spacing between crossing points and turning points, which are marked by vertical yellow dashed lines in Fig. 5.7, is reduced for spin waves traveling into the hot region of the heated film. The propagation angle of the spin wave as measured from the long axis of the film, $\theta = \tan y/x$, is $\theta = 36^\circ$ for the room temperature sample and gradually increased from $\theta = 36^\circ$ to 40° in the heated sample. Figure 5.8 shows the 2D BLS intensity profile for the sample at room temp subtracted from the intensity profile for the sample with an applied temperature gradient, where the scans were first integrated over the whole period of the pulse. This plot highlights the strong intensity differences at the crossing points, and it also reveals differences in intensity that occur preferentially along the downward-slanted directions where the spin wave populations are higher when the sample is heated. Defects have previously been observed to lead to the regeneration of caustic spin wave beams in the absence of heating [147, 148] so the downward-slanted beam at $x = 1.5$ mm may be related to the presence of a defect, where the heating has caused enough of a change in beam angle that the beam scatters from a defect that it previously avoided. In the following discussion it will be shown that caustic beams are permitted by the dispersion manifolds for our excitation conditions however this consideration is beyond the scope of this thesis.

5.5. CALCULATED DISPERSION RELATIONS

The diamond-shaped spin wave propagation pattern observed in the 2D BLS data is a consequence of the shape of the dispersion surfaces at the chosen combination of H and f_p . Figure 5.9a shows the dispersion surfaces for the YIG film, calculated following Kalinikos

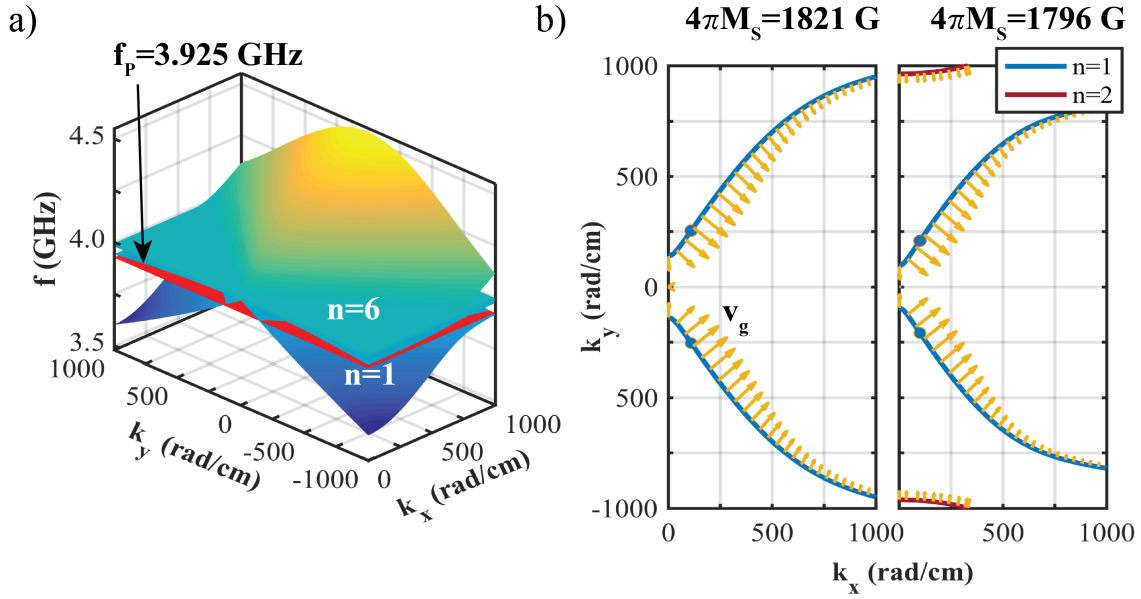


FIGURE 5.9. (a) Dispersion surfaces calculated for $H = 779$ Oe and $4\pi M_S = 1821$ G for spin waves with wavevectors at all angles between parallel (DE) and perpendicular (BV) to the long axis of the film. The solid red plane indicates the pumping frequency. (b) The allowed wavevectors and the associated group velocities, found by taking a cut of the dispersion surfaces at the pumping frequency ($f_p = 3.925$ GHz), are shown for two values of $4\pi M_S$. The arrows represent the group velocity magnitude and direction, where the maximum group velocity is $73 \mu\text{m/ns}$.

1986 [20], assuming a gyromagnetic ratio of $\gamma/2\pi = 2.80$ MHz/Oe and an exchange constant of $\alpha = 3.1 \times 10^{-12}$ cm², where k_x and k_y are the wavevector components along the film length and width, respectively. Since the film is relatively thick there are a number of perpendicular standing spin wave (PSSW) modes. The allowed wavevectors can be found by taking a cut of the dispersion surfaces at a frequency of $f = f_p$ (red shaded plane). The allowed wavevectors and the associated group velocities \mathbf{v}_g , obtained by taking the gradient of the dispersion surfaces [6], are shown in Fig. 5.9b for $f_p = 3.925$ GHz. There is a difference between the wavevectors that are allowed by the dispersion curves and those which

can be efficiently excited by the antenna. Unwrapped phase measurements made with the network analyzer indicate efficient enough excitation to see transmission amplitude for k_x wavenumbers between 80 and 1060 rad/cm. Comparing with the slowness curves presented in Fig. 5.9b we see that we are exciting a wide range of k_y wavenumbers.

The dispersion calculations predict that the excited spin waves will propagate at appreciable angles from the direction of the static field, thus they are of mixed DE and BV character. The direction in which the spin wave beam energy will propagate is given by the direction of the group velocity vector, as shown in Fig. 5.9b. Under these excitation conditions there is a point (indicated by a solid blue dot) on each slowness curve where there is an inflection in the curvature ($\partial^2 k_y / \partial k_x^2 = 0$). Spin waves excited near points of inflection are referred to as caustic beams [147]. Given the fact that our microstrip antenna is able to excite spin waves with wavevectors well above 630 rad/cm, as verified by phase measurements made by the network analyzer, we know we are exciting spin waves with a range of group velocities. Thus even though we expect two dominant directions of propagation, as observed in the BLS data, we know that this grouping of spin waves does not form a true caustic beam and may be referred to as a semi-caustic beam or just a spin wave beam. Most studies of caustics use a constriction or antidot to act as a point source of true caustic spin wave beams [144, 142, 149]. Diamond-shaped propagation patterns, usually completely filled in rather as opposed to only the outline that is observed here, have been imaged previously in extended films in a surface wave geometry where the diamond pattern is attributed to the fact that a microstrip antenna will produce a range of values that constructively interfere near the center of the film [150]. In Fig. 5.9b the group velocity directions are nearly the same for a broad range of excited wavevectors, which leads to the formation of spin wave

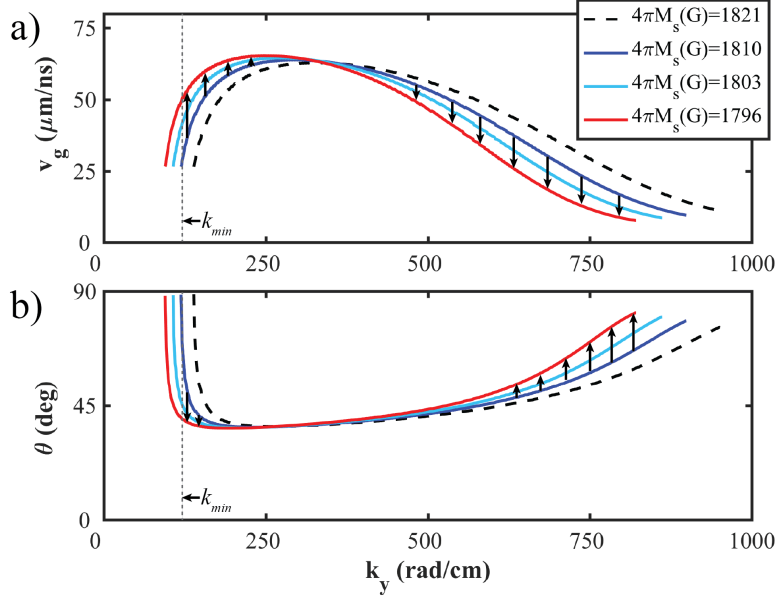


FIGURE 5.10. Calculated v_g (a) and θ (b) for $H = 779$ Oe and over the excited wavevector range three $4\pi M_S$ values that correspond to $x = 1.0, 4.0,$ and 5.5 mm for the heated sample. Only the thickness mode with the highest group velocity is shown for each k_y . The black arrows show the expected changes in v_g and θ .

beams at two well-defined propagation angles [151] even in the absence of a constriction, where the beams originate from a region at the center of the film width at the antenna. The dominant angles predicted from the dispersion calculations correspond well to the beam angles observed in the 2D BLS data.

In warmer regions $4\pi M_S$ is lower, which shifts the dispersion manifolds downward and also increases the density of the thickness modes. Notably, the positions of the gaps in the spin wave surfaces that arise due to the PSSW modes shift appreciably with a relatively small change in $4\pi M_S$. Figure 5.10 shows the calculated group velocity magnitudes v_g and angles θ as a function the component of the wavevector along the width of the film, k_y , for several different $4\pi M_S$ values. Here we assume that as the spin waves travel into progressively hotter regions, $4\pi M_S$ is reduced according to the curve shown in Fig. 5.2. As the spin waves travel into the hotter region both the frequency and the component of the wavevector along the

width, k_y , will be conserved whereas the component of the wavevector along the length of the film, k_x , will evolve according to the dispersion curves and there will be an associated change in v_g and θ . One can think of dividing the length of the film into many sections, each with a different value of $4\pi M_S$. Then at the boundary of each section there will be a Snell's law type refraction [152] leading to a gradual steering of the beam as observed here.

The expected changes in v_g and θ are illustrated in Fig. 5.10a and 5.10b, respectively, for spin waves that travel into a thermal gradient where the black arrows are used to illustrate the expected changes from the cool (blue) to hotter (red) regions of the sample. Given that it is mainly the spin waves with appreciable v_g at the antenna that propagate into the BLS scan region, there is a minimum k_y , imposed by the dispersion curves when the spin waves are excited (shown as the k_y corresponding to $k_x = 0$ in Fig. 5.9) and marked as k_{min} in Fig. 5.10. For $k_{min} < k_y < 350$ rad/cm a slight increase in v_g is expected, whereas for $k_y > 350$ rad/cm an overall reduction in v_g is predicted such that the spin waves with high wavenumber are significantly slowed or even stopped within the thermal gradient. This can result in an increase in spatial energy density as the spin waves will tend to pile up within the heated regions. While this effect may be partially compensated by higher damping in the hotter film, a stronger overall BLS signal was observed as shown in Figure 5.7. We note that a decrease in M_S with increasing T (and hence x) should also result in progressively larger oscillation amplitude as the spin waves travel towards the warmer end of the sample, although the latter would lead to a spatially uniform increase in intensity, whereas the BLS scans show changes in intensity that are spatially more complex. Fig. 5.10b shows a wide range of k_y (200 rad/cm $< k_y < 400$ rad/cm) for which θ is approximately equal to 40° , which is consistent with the experimentally observed beam angle. Heating is expected to

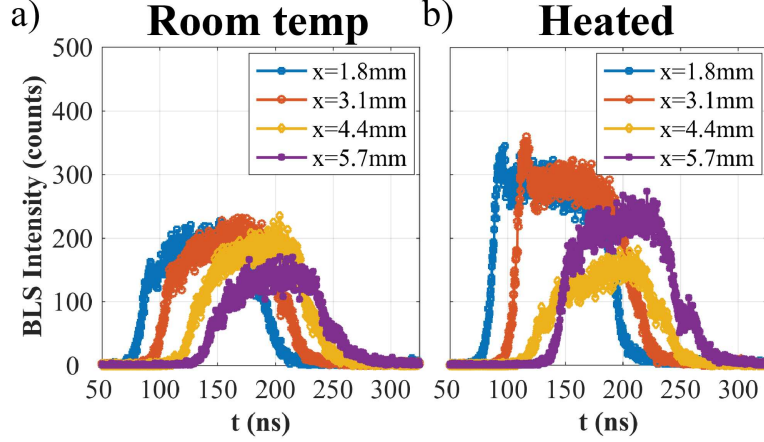


FIGURE 5.11. TR-BLS data integrated over the width of the film are shown at selected x for spin wave pulses traveling through the film a) at room temperature and b) with a thermal gradient applied. These positions correspond to the locations of the nodes and turning points of the heated sample, indicated by the dashed vertical lines in Fig. 5.7b.

only affect spin waves with k_y that are close to the PSSW mode crossings but small increases in θ on the order of up to a few degrees with increasing T are predicted for $k_y > 400$ rad/cm through the range of maximum excitation efficiency ($k_y < 630$ rad/cm), which is consistent with the experimental observations.

Changes in v_g should lead to changes in the time-domain profile of a spin wave pulse as a function of position for the heated sample. Plots of the width-averaged TR-BLS intensity at five distances from the input antenna are shown in Fig. 5.11. For the room temperature sample the TR-BLS pulse is shifted in time at the various locations by a time delay that is consistent with a constant average velocity and the pulse shape is essentially the same at all x , apart from a gradual overall reduction in the signal intensity with increasing x that can be attributed to normal spin wave propagation losses. In contrast, the pulse intensities for the heated sample show more dramatic changes as a function of x . The signal intensity is generally higher for the heated sample, which may, in part, be due to the fact that the pumping frequency is slightly higher on the dispersion curve and hence it is possible to excite

spin waves more efficiently. More importantly, as shown in Fig. 5.11, the signal is small at $x = 4.4$ mm and then increases at 5.7 mm and the pulse shape evolves from a relatively flat pulse in time with a small spike at the beginning ($x = 1.8$ mm and 3.1 mm) to a pulse that shows an increase in intensity as a function of time ($x = 4.4$ mm and 5.7 mm), where the pulse at the farthest position shows an additional trailing edge. This suggests that some wavevector components of the spin wave pulse travel at a slower rate. The group velocity calculations shown in Fig. 5.10a predict that the dominant effect of the heat will be that spin waves with large wavenumbers ($k > 300$ rad/cm) will slow down as they travel into a hot region which would appear as a reduction in intensity in the first part of the pulse (during and immediately after the rise) and an extension of the pulse in time corresponding to more spin waves arriving at a later time (during and after the fall) for pulses detected at larger x . The dispersion curves suggest that high- k spin waves, which constitute an appreciable portion of the pulse, will be slowed down as much as $18 \mu\text{m}/\text{ns}$ as they are heated. If on average, the high- k spin waves slowed down by $10 \mu\text{m}/\text{ns}$, they would arrive about 20 ns later than the low- k spin waves, which is consistent with the data shown in Fig. 5.11b. The development of a trailing pulse edge and the observed change in beam angle, which should only occur if high- k spin waves are involved, suggest that the high- k spin waves are an important consideration. The observed reduction and then increase in the width-averaged signal further suggests that interference effects due to the changing spin wavelengths may play a role in determining the local spin wave intensity.

5.6. SHORT PULSE EXCITATION

It is evident, as demonstrated by the middle plots of Fig. 5.7 for instance, that the 100 ns pulse duration used in this study spans a region wider than the two-dimensional BLS

scan region. To better understand the effects of the thermal gradient on spin waves similar measurements were performed using a shorter pulse ($dt = 20$ ns) in order to see the entire pulse within the scan window at one time. A larger thermal gradient was achieved using two thermoelectric heating elements mounted over the input and output antennas instead of the blue heating laser. The temperature at the surface of each heater was continuously monitored by thermocouples and controlled by the voltage using a feedback loop. The surface temperatures of the heaters were 30°C at the input antenna and 80°C at the output antenna with separation of 10 mm between the heaters which corresponds to a 24 K over the BLS scan range used here or a thermal gradient of $\nabla_x T = 4.5$ K/mm as shown in Fig. 5.12a. The actual thermal gradient on the YIG film may be slightly lower due to inefficient heat transfer through thermal grease contact. Even so, the thermal gradient should be significantly larger than the 4 K gradient observed using the blue laser, which will result in a much larger change in $4\pi M_S$ as shown in Fig. 5.12b. The measurements were performed in the surface wave geometry under the same conditions used for the long pulses, $H = 779$ Oe and $f_p = 3.925$ GHz. The short CW microwave pulses were supplied by a microwave generator and TTL switch with a pulse duration of 20 ns, rise time of 5 ns, and a repetition rate of 1 MHz chosen to avoid nonlinear and additional heating effects.

The results of the two-dimensional TR-BLS measurements are shown in Fig. 5.13. First we notice a diamond-like pattern of spin wave propagation similar to that observed with long pulse excitation. This time the diamond shape appears slightly more filled, especially in the heated sample. The amount that the diamond is filled depends on the precise excitation conditions. The microwave switch used in the short pulse data had a longer rise time 5 ns compared with the rise time of the switch used for the long pulse data 1 ns. It is possible

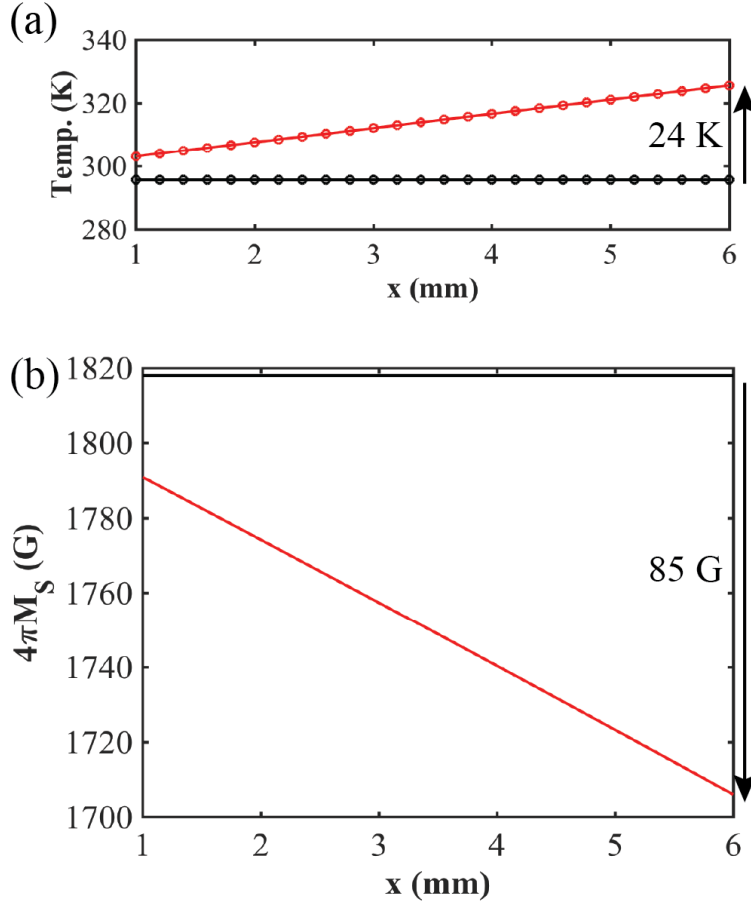


FIGURE 5.12. (a) The calculated temperature profile of the YIG film as a function of distance from the input antenna x . Endpoint temperatures were controlled using two thermocouples on the surfaces of the thermoelectric heaters. The expected linear profile was confirmed by thermal camera measurements. (b) Saturation magnetization of the YIG film as a function of the distance from the input antenna for the temperature range shown in (a).

that the difference in rise time corresponds to a different spectral width, i.e. the range of frequencies excited around the central f_p peak, which could help explain the difference in the diamond pattern. The BLS intensity is generally higher in the 2D scan of the heated sample, where the difference is especially pronounced between $x = 1.8$ and 2.1 mm. The nodes and antinodes of the diamond shape appear to be lengthened along the x -direction in the heated case but the effect is subtle and is difficult to discern given the limited BLS intensity past $x = 3$ mm.

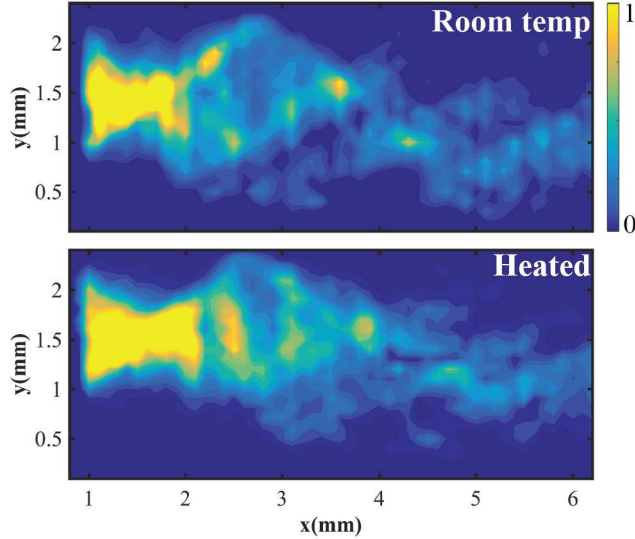


FIGURE 5.13. TR-BLS data integrated over a time period longer than the pulse is shown for the sample at room temperature (top) and with a thermal gradient applied using thermoelectric heaters (bottom). For these measurements the film was saturated in the DE geometry by a field of $H = 779$ Oe oriented in the $+y$ direction and $f_p = 3.925$ GHz.

The BLS intensity integrated over the width of the film and over the period of the pulse provides a reliable method to compare intensities and measure the spin wave decay length. Figure 5.14 shows the width-integrated BLS intensity for the film at room temperature and with the thermal gradient. While there is some local variation in intensity, the intensity of the spin waves traveling into the thermal gradient is generally higher than in the sample at room temperature. The exponential fits show that there is no statistically significant difference in the decay lengths for the two different heating conditions: $\lambda_H = 2.5 \pm 0.1$ mm and $\lambda_{RT} = 2.4 \pm 0.2$ mm.

It has been shown [144] that spin wave pulses traveling into strong thermal gradients can undergo a spatial compression effect such that as the pulse travels into a progressively hotter region, the spatial extent of the pulse is progressively reduced resulting in an increase in the local energy density. For pulses as short as the ones used here a spatial compression would

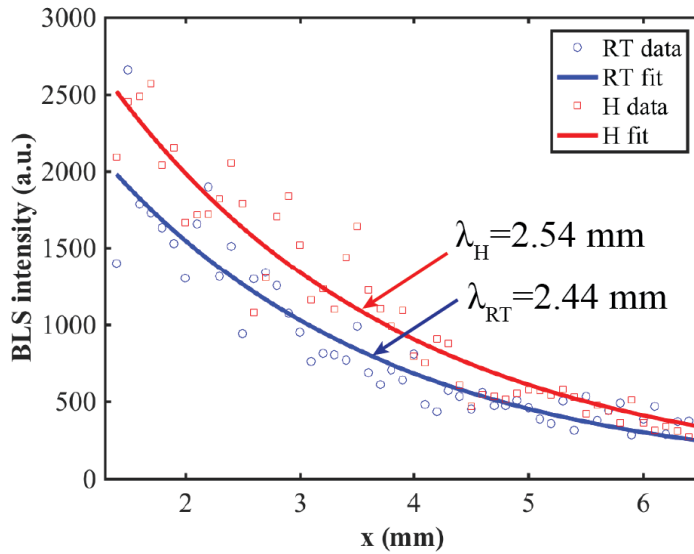


FIGURE 5.14. TR-BLS data integrated over the width of the film and fit with an exponential function for the sample at room temperature and with a thermal gradient. The decay lengths extracted from the fits are shown.

be evident. Figure 5.15 shows the spatial pulse width as a function of the distance from the antenna. These curves were obtained by fitting the width-averaged BLS intensity vs. x with a Gaussian function and extracting the FWHM at each time. The FWHM of the pulse is reported when the center of the pulse passes position x as shown in Fig. 5.15. If there are any spatial compression effects they should show up as a progressive decrease in pulse width as a function of increasing x . The spatial pulse width for the heated sample is lower than the pulse width in the sample at room temperature. This can be attributed to the fact that the average temperature of the heated film is higher than that of the room temperature film. However, the thermal gradient is not strong enough to observe any spatial compression over the length of the BLS scan range. One is then left with the question of why the BLS intensity of the heated sample is noticeably stronger overall if there is not an appreciable increase in energy density from spatial compression. We recall that the pumping conditions were chosen to maximize the transmission of the film for the heated case. As a result the

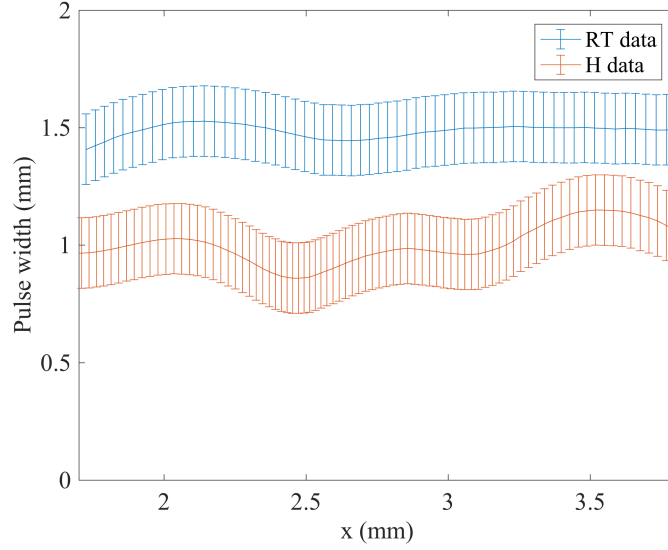


FIGURE 5.15. Spatial extent of a pulse traveling into a thermal gradient compared with room temperature. The spatial pulse width is lower for the heated sample, which is due to the fact that the spin waves travel slower in the heated sample, primarily due to the higher average temperature. The vertical bars represent the uncertainty in the pulse width.

spin wave pulse is generated with a higher efficiency at the start. Thus, the overall difference in intensity is not related to the thermal profile for even this larger thermal gradient.

Surface spin waves traveling into a thermal gradient are expected to exhibit a deceleration. In order to look for such an effect the time-domain profile of the pulse at each measured distance from the input antenna was fit with a Gaussian profile to track the arrival time of the pulse as well as the temporal pulse width, both shown in Fig. 5.16. The arrival times appear to increase linearly with increasing x . Linear fits to t vs. x show that the pulse travels slower into the thermal gradient with an average speed of $v_{g,H} = 51 \mu\text{m}/\text{ns}$ compared with the room temperature average speed of $v_{g,RT} = 65 \mu\text{m}/\text{ns}$. The linear fit provides an excellent fit to the arrival time data for the room temperature case, however, deviations from linearity are apparent for the heated case. Plots of the pulse duration as a function of x are shown in the bottom plot. These data show little variation in pulse width for the room

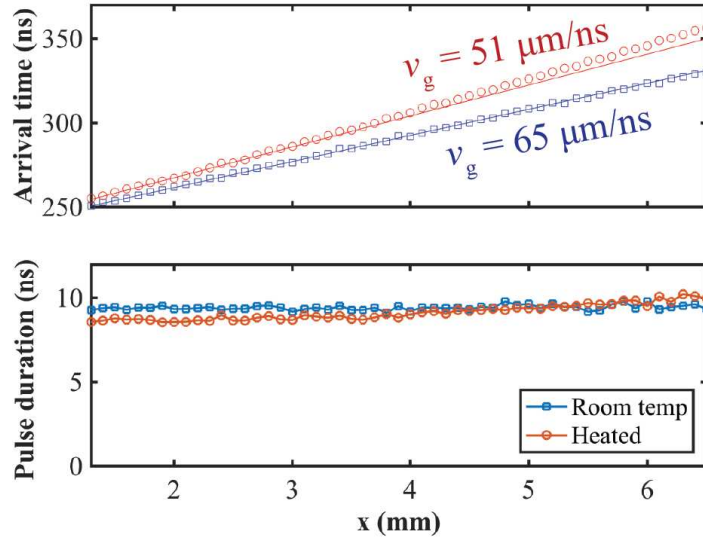


FIGURE 5.16. Arrival times and pulse widths of the spin wave pulses traveling through the BLS scan region. The arrival times for the heated film make a significant departure from a linear fit to the first portion of the data indicating a decrease in velocity. Not much difference in temporal pulse duration is observed.

temperature case around 9.3 ns, whereas the pulse duration for the heated case goes from 8.6 ns to 10.1 ns indicating some heat-induced pulse broadening in the time domain.

As mentioned above, in Fig. 5.16a there is a curvature to the arrival times vs. x for the heated sample. The temporal pulse shape vs x (Fig. 5.17) shows that the pulse traveling through the heated sample travels slower but does not provide much information on a possible acceleration. In order to look for a shift in group velocity over the scan range, linear fits were used to obtain the slope over short ranges of the arrival times to extract the deceleration. Figure 5.18 shows the change in speed of a pulse travel in both thermal conditions using a sliding fit range of $x = 1$ mm. We see that the pulse traveling into a thermal gradient undergoes a reduction in speed from $v_{gH} = 57 \mu\text{m}$ down to $48 \mu\text{m}$. This corresponds to a 16 percent reduction in group velocity over the BLS scan region (5 mm) due to the non-uniform thermal profile, which is similar in magnitude to what is predicted using the approximate

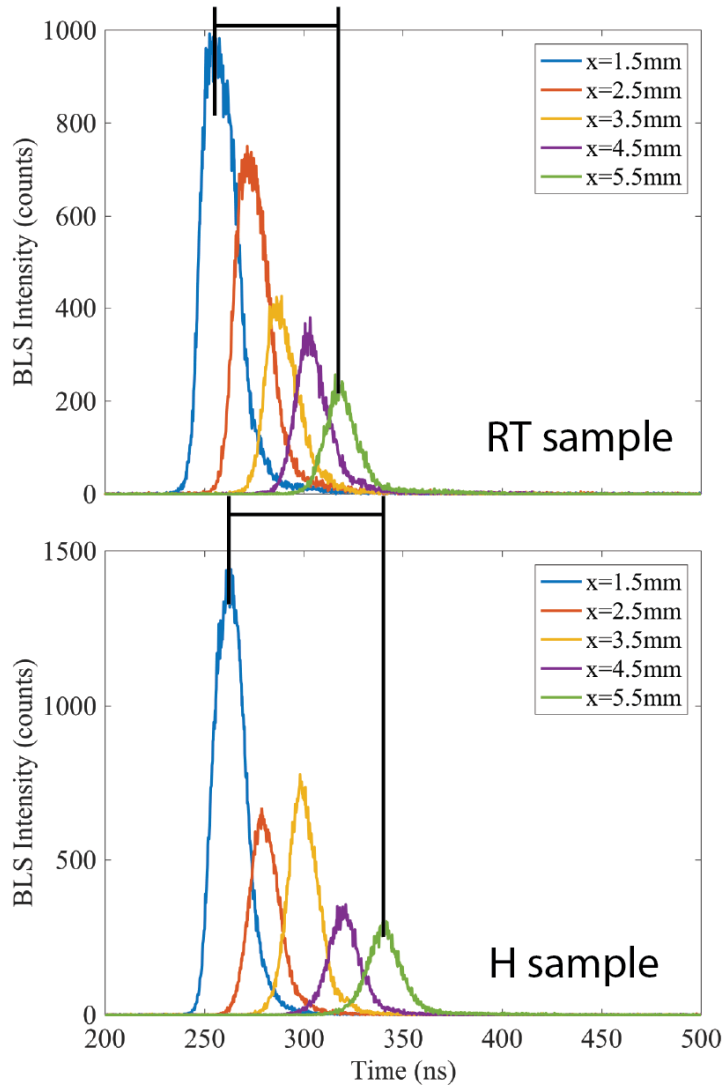


FIGURE 5.17. Pulse shape in time as it travels along the length of the film. While the initial times are not identical, a spreading in the pulses of the heated film indicate later and later arrival times of the pulse as it travels into progressively hotter regions.

dispersion relation for surface spin waves (equation 2.37) in conjunction with a reduction in M_S with distance that is consistent with the imposed thermal gradient. These results are potentially important for thermally controlled delay lines, for instance, where waste heat could be used to affect the speed of the transmitted signal. The room temperature case shows a gradual reduction in pulse amplitude in Fig. 5.17 as a function of increasing distance, whereas the amplitudes fluctuate as a function of distance in the case of a thermal

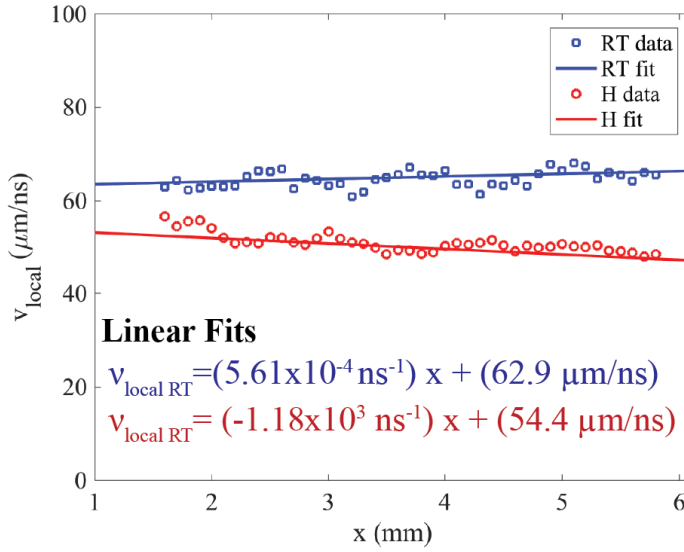


FIGURE 5.18. Local group velocities of spin wave pulses traveling through the BLS scan region under both temperature profiles. The pulses traveling into the thermal gradient experience a slowdown of around 16 percent within the scan range.

gradient. This result is qualitatively similar to what was observed for the smaller thermal gradient (Fig. 5.11) and again, indicates that interference effects may play a role.

5.7. PROJECT SUMMARY

In summary, we have examined the effect of a thermal gradient on the propagation characteristics of spin waves in a surface wave configuration. BLS measurements show that even for a small thermal gradient where the width-averaged transmission characteristics detected at an output antenna are largely unaffected by the heat there are significant changes in the local spin wave propagation characteristics. Spatial BLS scans, performed using a pumping frequency just below the ferromagnetic resonance frequency, show two spin wave beams at distinct angles ($\theta = \pm 36^\circ$) from the long axis of the film that lead to a diamond-shaped propagation pattern. The imposed thermal gradient leads to a shift in the beam angle from $\theta = 36^\circ$ to 40° , noticeable increases in spin wave intensity that are highly position

dependent, and to significant modification to the temporal pulse shape that are consistent with a $10 \mu\text{m}/\text{ns}$ reduction in group velocity on average for the high- k wavevectors. Short pulse spin waves traveling into an even larger thermal gradient shown a reduction in velocity by 16% accompanied by a large increase in BLS intensity and an increase in the spin wave decay length. These effects are a consequence of the proximity of the propagating spin waves to the perpendicular standing spin wave modes that provides a mechanism for large changes in the spin wave dispersion characteristics even for small changes in temperature. This will be important for microwave device development and also suggests a new approach to the control of beam angle and intensity in spin wave logic device using small thermal gradients. This work has been submitted to Physical Review B and significant portions of that article are reproduced and/or expanded upon in this chapter.

CHAPTER 6

SUMMARY

This thesis presented two experimental studies focussing on the potential to harness spin wave dynamics using heat and structural geometry. Both studies were performed predominantly with the Brillouin light scattering (BLS) technique which is a versatile and powerful technique in modern magnetics research. The importance of dispersion relations as a tool for understanding spin waves in microstrips and continuous thin films was presented. Calculated dispersion relations were used to fit and analyze important spin wave metrics including frequencies, group velocities, and propagation angles observed in the experimental data. Not only are spin waves a great testbed for fundamentally interesting physics, but a fuller understanding of spin wave behavior will deepen knowledge of magnetic materials and provide unforeseen applications for years to come.

The high-frequency dynamics of an antivortex (AV) were studied experimentally. Several high-frequency modes of the AV were observed under both in- and out-of-plane excitation. Spatial profiles of the AV modes were mapped using micro-BLS. Dynamics were compared with micromagnetic simulations that revealed that the most prominent modes of the AV correspond directly to width-quantized propagating spin wave modes in the adjacent legs. Given the short wavelength of the AV-generated spin waves, we believe that such a structure could be used as a short spin wave source as this range of spin waves is often difficult to generate through traditional methods. An unfathomable amount of literature regarding magnetic vortices and their potential for applications exists and is still growing. The antivortex may be even more useful than the vortex because of its intrinsic topologic and the ability to couple smoothly to nearby continuous films or microwires, yet not many groups

pursue research on AVs because they are difficult to stabilize. I am grateful that I had the opportunity to study such a rare area of science.

Even after the author was warned of the complexity of any kind of research involving the effects of heat, the potential to control spin wave propagation with waste heat seemed too tantalizing to resist with such obvious applications to spin caloritronics. BLS measurements of spin waves traveling into a thermal gradient were presented. An intricate diamond shaped propagation pattern was observed that is the direct result of exciting a wide range of wavevectors. The dispersion manifold for arbitrary propagation angles was calculated and used to predict the range of wavevectors excited by a microstrip antenna in a YIG film and calculated group velocities and beam angles were compared with those measured by BLS. The experimental work presented here showcases the possibility of using even a modest thermal gradient to significantly alter the speed and steer a beam of propagating spin waves. These results could potentially have applications for signal modification and control in the new field of spintronics.

6.1. FUTURE DIRECTIONS

In spite of drastically changing directions in the magnetics industry, fundamental magnetics research is a productive and actively growing field with many exciting possibilities on the horizon. If I had the opportunity to explore further research directions in the Nanomagnetism Lab at CSU, I would delve deeper into the field of spintronics. As an information carrier, spin waves have so many desirable features. They can propagate a signal not only in metallic materials, but also semiconductors and insulators. They can carry information without considerable Joule heating as with conventional electronics. Spin waves are also highly scalable with exchange spin waves having length scales at atomic levels. Lastly, as a

wave phenomena, spin waves have the potential to carry more information and participate in wave-based logic operations. The future of spin wave research is bright and exciting.

BIBLIOGRAPHY

- [1] A. Haldar and K. S. Buchanan, “Magnetic antivortex formation in pound-key-like nanostructures,” *Applied Physics Letters*, vol. 102, no. 11, p. 112401, 2013.
- [2] M. Asmat-Uceda, L. Li, A. Haldar, B. Shaw, and K. S. Buchanan, “Geometry and field dependence of the formation of magnetic antivortices in pound-key-like structures,” *Journal of Applied Physics*, vol. 117, no. 17, p. 173902, 2015.
- [3] M. A. Asmat-Uceda, *Investigation of the dynamics of magnetic vortices and antivortices using micromagnetic simulations*. PhD thesis, Colorado State University. Libraries, 2017.
- [4] D. J. Griffiths, *Introduction to Electrodynamics*. Upper Saddle River, NJ: Prentice-Hall, Inc., 3th ed., 1999.
- [5] J. D. Jackson, *Classical Electrodynamics*. New York, NY: John Wiley and Sons, Inc., 3th ed., 1999.
- [6] D. D. Stancil and A. Prabhakar, *Spin waves: theory and applications*. New York: Springer, 2009.
- [7] Y. Zhu, *Modern techniques for characterizing magnetic materials*. Springer Science & Business Media, 2005.
- [8] C. Kittel, *Introduction to Solid State Physics*. Hoboken, NJ: John Wiley and Sons, Inc., 8th ed., 2005.
- [9] H. N. Russell and F. A. Saunders, “New regularities in the spectra of the alkaline earths,” *Astrophysical Journal*, vol. 61, p. 38, Jan 1925.
- [10] A. G. Gurevich and G. A. Melkov, *Magnetization oscillations and waves*. Boca Raton: CRC Press, 1996.

- [11] W. Commons, “File:magnetic hysteresis.png — wikimedia commons, the free media repository,” 2016.
- [12] L. Landau and E. Lifshitz, “To the theory of the dispersion of the ferromagnetic-body permeability,” *Collected paper. Ed. Pergamon*, 1965.
- [13] T. L. Gilbert, “A phenomenological theory of damping in ferromagnetic materials,” *IEEE Transactions on Magnetics*, vol. 40, no. 6, pp. 3443–3449, 2004.
- [14] C. Kittel, “On the theory of ferromagnetic resonance absorption,” *Phys. Rev.*, vol. 73, pp. 155–161, Jan 1948.
- [15] S.-K. Kim, “Micromagnetic computer simulations of spin waves in nanometre-scale patterned magnetic elements,” *Journal of Physics D: Applied Physics*, vol. 43, no. 26, p. 264004, 2010.
- [16] R. W. Damon and J. R. Eshbach, “Magnetostatic modes of a ferromagnet slab,” *Journal of Physics and Chemistry of Solids*, vol. 19, no. 3-4, pp. 308–320, 1961.
- [17] G. Rado and J. Weertman, “Spin-wave resonance in a ferromagnetic metal,” *Journal of Physics and chemistry of solids*, vol. 11, no. 3-4, pp. 315–333, 1959.
- [18] B. Hillebrands, “Spin-wave calculations for multilayered structures,” *Physical Review B*, vol. 41, no. 1, p. 530, 1990.
- [19] F. Hoffmann, A. Stankoff, and H. Pascard, “Evidence for an exchange coupling at the interface between two ferromagnetic films,” *Journal of Applied Physics*, vol. 41, no. 3, pp. 1022–1023, 1970.
- [20] B. A. Kalinikos and A. N. Slavin, “Theory of dipole-exchange spin wave spectrum for ferromagnetic films with mixed exchange boundary conditions,” *Journal of Physics C: Solid State Physics*, vol. 19, no. 35, p. 7013, 1986.

- [21] B. A. Kalinikos, *Linear and Non-linear Spin Waves in Magnetic Films and Superlattices*, ch. Dipole-exchange spin-wave spectrum of magnetic films. Singapore: World Scientific Publishing Company, 1994.
- [22] O. Vendik and D. Chartorizhskii *Sov. Phys.-Solid State*, vol. 11, 1970.
- [23] B. A. Kalinikos. personal communication.
- [24] B. Kalinikos, “Excitation of propagating spin waves in ferromagnetic films,” in *IEE Proceedings H (Microwaves, Optics and Antennas)*, vol. 127, pp. 4–10, IET, 1980.
- [25] J. Griffiths, “Anomalous high-frequency resistance of ferromagnetic metals,” *Nature*, vol. 158, no. 4019, p. 670, 1946.
- [26] R. Krishnan, K. V. Rao, and H. H. Liebermann, “Magnetization and FMR studies in amorphous Fe₉₀Zr₁₀ and Fe₇₀Ni₂₀Zr₁₀ ribbons,” *Journal of Applied Physics*, vol. 55, no. 6, pp. 1823–1825, 1984.
- [27] M. Dominguez, S. Lofland, S. Bhagat, A. Raychaudhuri, H. Ju, T. Venkatesan, and R. Greene, “Are single phase manganite samples truly homogeneous? A magnetic resonance study,” *Solid state communications*, vol. 97, no. 3, pp. 193–196, 1996.
- [28] J. Das, S. S. Kalarickal, K.-S. Kim, and C. E. Patton, “Magnetic properties and structural implications for nanocrystalline Fe-Ti-N thin films,” *Phys. Rev. B*, vol. 75, p. 094435, Mar 2007.
- [29] R. C. Taylor and A. Gangulee, “Magnetization and magnetic anisotropy in evaporated GdCo amorphous films,” *Journal of Applied Physics*, vol. 47, no. 10, pp. 4666–4668, 1976.

- [30] P. Röschmann, M. Lemke, W. Tolksdorf, and F. Welz, “Anisotropy fields and FMR linewidth in single-crystal Al, Ga and Sc substituted hexagonal ferrites with M structure,” *Materials research bulletin*, vol. 19, no. 3, pp. 385–392, 1984.
- [31] X. Liu, Y. Sasaki, and J. K. Furdyna, “Ferromagnetic resonance in Ga_{1-x}Mn_xAs: Effects of magnetic anisotropy,” *Phys. Rev. B*, vol. 67, p. 205204, May 2003.
- [32] M. J. Hurben, D. R. Franklin, and C. E. Patton, “Angle dependence of the ferromagnetic resonance linewidth in easy-axis and easy-plane single crystal hexagonal ferrite disks,” *Journal of Applied Physics*, vol. 81, no. 11, pp. 7458–7467, 1997.
- [33] J. C. Slonczewski, “Conductance and exchange coupling of two ferromagnets separated by a tunneling barrier,” *Phys. Rev. B*, vol. 39, pp. 6995–7002, Apr 1989.
- [34] B. Heinrich, J. Cochran, M. Kowalewski, J. Kirschner, Z. Celinski, A. Arrott, and K. Myrtle, “Magnetic anisotropies and exchange coupling in ultrathin fcc Co (001) structures,” *Physical Review B*, vol. 44, no. 17, p. 9348, 1991.
- [35] V. Kamberský, J. Cochran, and J. Rudd, “Anisotropic low-temperature FMR linewidth in nickel and the theory of anomalous damping,” *Journal of Magnetism and Magnetic Materials*, vol. 104, pp. 2089–2091, 1992.
- [36] R. Urban, G. Woltersdorf, and B. Heinrich, “Gilbert damping in single and multilayer ultrathin films: Role of interfaces in nonlocal spin dynamics,” *Phys. Rev. Lett.*, vol. 87, p. 217204, Nov 2001.
- [37] R. Yilgin, M. Oogane, Y. Ando, and T. Miyazaki, “Gilbert damping constant in polycrystalline CO₂MnSi heusler alloy films,” *Journal of Magnetism and Magnetic Materials*, vol. 310, no. 2, Part 3, pp. 2322–2323, 2007. Proceedings of the 17th International Conference on Magnetism The International Conference on Magnetism.

- [38] N. Mo, J. Hohlfield, M. Ul Islam, C. S. Brown, E. Girt, P. Krivosik, W. Tong, A. Rebei, and C. E. Patton, “Origins of the damping in perpendicular media: Three component ferromagnetic resonance linewidth in Co-Cr-Pt alloy films,” *Applied Physics Letters*, vol. 92, pp. 022506–022506–3, Jan 2008.
- [39] Z. Zhang, L. Zhou, P. E. Wigen, and K. Ounadjela, “Angular dependence of ferromagnetic resonance in exchange-coupled co/ru/co trilayer structures,” *Phys. Rev. B*, vol. 50, pp. 6094–6112, Sep 1994.
- [40] M. Hurben and C. Patton, “Theory of two magnon scattering microwave relaxation and ferromagnetic resonance linewidth in magnetic thin films,” *Journal of applied physics*, vol. 83, no. 8, pp. 4344–4365, 1998.
- [41] O. Yalçın, “Ferromagnetic resonance-theory and applications,” *InTech*, p. 48, 2013.
- [42] S. Foner, “Versatile and sensitive vibrating-sample magnetometer,” *Review of Scientific Instruments*, vol. 30, no. 7, pp. 548–557, 1959.
- [43] S. Foner, “Vibrating sample magnetometer,” *Review of Scientific Instruments*, vol. 27, no. 7, pp. 548–548, 1956.
- [44] J. Clarke and A. I. Braginski, *The SQUID handbook. Vol. 2. Applications of SQUIDs and SQUID systems*. New York: Wiley, 2006.
- [45] A. T. Young, “Rayleigh scattering,” *Physics Today*, vol. 35, pp. 42–48, 1982.
- [46] C. V. Raman, “A change of wave-length in light scattering,” *Nature*, vol. 121, p. 619, 1928.
- [47] P. H. Gammon, H. Kiefte, and M. J. Clouter, “Elastic constants of ice samples by Brillouin spectroscopy,” *The Journal of Physical Chemistry*, vol. 87, no. 21, pp. 4025–4029, 1983.

- [48] A. D. Alvarenga, M. Grimsditch, and R. J. Bodnar, “Elastic properties of water under negative pressures,” *The Journal of Chemical Physics*, vol. 98, no. 11, pp. 8392–8396, 1993.
- [49] M. Grimsditch, S. Popova, and A. Polian, “Test of the equation of state of water up to freezing at 100 and 200 degrees C,” *The Journal of Chemical Physics*, vol. 105, no. 19, pp. 8801–8803, 1996.
- [50] F. Li, Q. Cui, Z. He, T. Cui, J. Zhang, Q. Zhou, G. Zou, and S. Sasaki, “High pressure-temperature Brillouin study of liquid water: Evidence of the structural transition from low-density water to high-density water,” *The Journal of Chemical Physics*, vol. 123, no. 17, 2005.
- [51] E. Courtens, J. Pelous, J. Phalippou, R. Vacher, and T. Woignier, “Brillouin-scattering measurements of phonon-fracton crossover in silica aerogels,” *Physical review letters*, vol. 58, pp. 128–131, 1987.
- [52] J. D. Bass, “Elasticity of grossular and spessartite garnets by Brillouin spectroscopy,” *Journal of Geophysical Research: Solid Earth (1978–2012)*, vol. 94, no. B6, pp. 7621–7628, 1989.
- [53] S. V. Sinogeikin, J. Zhang, and J. D. Bass, “Elasticity of single crystal and polycrystalline MgSiO_3 perovskite by Brillouin spectroscopy,” *Geophysical research letters*, vol. 31, no. 6, 2004.
- [54] P. Dainese, P. S. J. Russell, N. Joly, J. Knight, G. Wiederhecker, H. L. Fragnito, V. Laude, and A. Khelif, “Stimulated Brillouin scattering from multi-GHz-guided acoustic phonons in nanostructured photonic crystal fibres,” *Nature Physics*, vol. 2, no. 6, pp. 388–392, 2006.

- [55] J. Ko, K. Roleder, and A. Bussmann-Holder, "Determination of elastic stiffness coefficients of lead zirconate single crystals in the cubic phase by Brillouin light scattering," in *Materials Science and Engineering Conference Series*, vol. 54, p. 2002, 2014.
- [56] S. Lees, N.-J. Tao, and S. Lindsay, "Studies of compact hard tissues and collagen by means of Brillouin light scattering," *Connective tissue research*, vol. 24, no. 3-4, pp. 187–205, 1990.
- [57] N. Berovic, N. Thomas, R. Thornhill, and J. Vaughan, "Observation of Brillouin scattering from single muscle fibres," *European Biophysics Journal*, vol. 17, no. 2, pp. 69–74, 1989.
- [58] V. Mathieu, K. Fukui, M. Matsukawa, M. Kawabe, R. Vayron, E. Soffer, F. Anagnostou, and G. Haiat, "Micro-Brillouin scattering measurements in mature and newly formed bone tissue surrounding an implant," *Journal of biomechanical engineering*, vol. 133, no. 2, p. 021006, 2011.
- [59] K. J. Koski, P. Akhenblit, K. McKiernan, and J. L. Yarger, "Non-invasive determination of the complete elastic moduli of spider silks," *Nature Materials*, vol. 12, no. 3, p. 262, 2013.
- [60] G. Scarcelli and S. H. Yun, "Confocal Brillouin microscopy for three-dimensional mechanical imaging," *Nature photonics*, vol. 2, no. 1, pp. 39–43, 2008.
- [61] S. Reiss, G. Bureau, O. Stachs, R. Guthoff, and H. Stolz, "Spatially resolved Brillouin spectroscopy to determine the rheological properties of the eye lens," *Biomedical optics express*, vol. 2, no. 8, pp. 2144–2159, 2011.

- [62] F. Palombo, M. Madami, N. Stone, and D. Fioretto, “Mechanical mapping with chemical specificity by confocal Brillouin and Raman microscopy,” *Analyst*, vol. 139, no. 4, pp. 729–733, 2014.
- [63] C. Sandweg, M. Jungfleisch, V. Vasyuchka, A. Serga, P. Clausen, H. Schultheiss, B. Hillebrands, A. Kreisel, and P. Kopietz, “Wide-range wavevector selectivity of magnon gases in Brillouin light scattering spectroscopy,” *Review of Scientific Instruments*, vol. 81, no. 7, p. 073902, 2010.
- [64] A. A. Serga, V. S. Tiberkevich, C. W. Sandweg, V. I. Vasyuchka, D. A. Bozhko, A. V. Chumak, T. Neumann, B. Obry, G. A. Melkov, A. N. Slavin, *et al.*, “BoseEinstein condensation in an ultra-hot gas of pumped magnons,” *Nature communications*, vol. 5, 2014.
- [65] V. E. Demidov, S. Urazhdin, and S. O. Demokritov, “Direct observation and mapping of spin waves emitted by spin-torque nano-oscillators,” *Nature materials*, vol. 9, no. 12, pp. 984–988, 2010.
- [66] M. Madami, S. Bonetti, G. Consolo, S. Tacchi, G. Carlotti, G. Gubbiotti, F. Mancoff, M. A. Yar, and J. Åkerman, “Direct observation of a propagating spin wave induced by spin-transfer torque,” *Nature nanotechnology*, vol. 6, no. 10, pp. 635–638, 2011.
- [67] V. E. Demidov, S. Urazhdin, V. Tiberkevich, A. Slavin, and S. O. Demokritov, “Control of spin-wave emission from spin-torque nano-oscillators by microwave pumping,” *Physical Review B*, vol. 83, no. 6, p. 060406, 2011.
- [68] V. E. Demidov, S. Urazhdin, H. Ulrichs, V. Tiberkevich, A. Slavin, D. Baither, G. Schmitz, and S. O. Demokritov, “Magnetic nano-oscillator driven by pure spin current,” *Nature materials*, vol. 11, no. 12, pp. 1028–1031, 2012.

- [69] K. An, D. R. Birt, C.-F. Pai, K. Olsson, D. C. Ralph, R. Buhrman, X. Li, *et al.*, “Control of propagating spin waves via spin transfer torque in a metallic bilayer waveguide,” *arXiv preprint arXiv:1308.6357*, 2013.
- [70] V. Naletov, G. de Loubens, S. Borlenghi, and O. Klein, “Spin-wave emission from spin-torque nano-oscillators and its control by microwave pumping,” in *Magnonics*, pp. 163–175, Springer, 2013.
- [71] V. Demidov, S. Urazhdin, A. Rinkevich, G. Reiss, and S. Demokritov, “Spin hall controlled magnonic microwaveguides,” *Applied Physics Letters*, vol. 104, no. 15, p. 152402, 2014.
- [72] G. Gubbiotti, S. Tacchi, G. Carlotti, N. Singh, S. Goolaup, A. Adeyeye, and M. Kostylev, “Collective spin modes in monodimensional magnonic crystals consisting of dipolarly coupled nanowires,” *Applied Physics Letters*, vol. 90, no. 9, p. 092503, 2007.
- [73] S. Tacchi, F. Montoncello, M. Madami, G. Gubbiotti, G. Carlotti, L. Giovannini, R. Zivieri, F. Nizzoli, S. Jain, A. Adeyeye, *et al.*, “Band diagram of spin waves in a two-dimensional magnonic crystal,” *Physical review letters*, vol. 107, no. 12, p. 127204, 2011.
- [74] G. Gubbiotti, M. Kostylev, S. Tacchi, M. Madami, G. Carlotti, J. Ding, A. Adeyeye, F. Zighem, A. Stashkevich, E. Ivanov, *et al.*, “Collective spin waves on a nanowire array with step-modulated thickness,” *Journal of Physics D: Applied Physics*, vol. 47, no. 10, p. 105003, 2014.

- [75] B. Van de Wiele and F. Montoncello, “Overcoming damping in spin wave propagation: A continuous excitation approach to determine time-dependent dispersion diagrams in 2d magnonic crystals,” *arXiv preprint arXiv:1403.2549*, 2014.
- [76] R. Zivieri, P. Malagò, and L. Giovannini, “Band structure and effective properties of binary magnonic crystals,” *Photonics and Nanostructures-Fundamentals and Applications*, 2014.
- [77] K. Vogt, F. Fradin, J. Pearson, T. Sebastian, S. Bader, B. Hillebrands, A. Hoffmann, and H. Schultheiss, “Realization of a spin-wave multiplexer,” *Nature Communications*, vol. 5, p. 3727, 04 2014.
- [78] A. Haldar, D. Kumar, and A. O. Adeyeye, “A reconfigurable waveguide for energy-efficient transmission and local manipulation of information in a nanomagnetic device,” *Nature nanotechnology*, vol. 11, no. 5, pp. 437–443, 2016.
- [79] A. Haldar, C. Tian, and A. O. Adeyeye, “Isotropic transmission of magnon spin information without a magnetic field,” vol. 3, no. 7, 2017.
- [80] S. Demokritov, B. Hillebrands, and A. Slavin, “Brillouin light scattering studies of confined spin waves: linear and nonlinear confinement,” *Physics Reports*, vol. 348, no. 6, pp. 441 – 489, 2001.
- [81] L. Landau and E. Lifshitz, “Electrodynamics of continuous media pergamon press oxford google scholar,” 1960.
- [82] W. Wettleing, M. G. Cottam, and J. R. Sandercock, “The relation between one-magnon light scattering and the complex magneto-optic effects in YIG,” *Journal of Physics C: Solid State Physics*, vol. 8, no. 2, p. 211, 1975.

- [83] J. Kerr, “Xliii. on rotation of the plane of polarization by reflection from the pole of a magnet,” *The London, Edinburgh, and Dublin Philosophical Magazine and Journal of Science*, vol. 3, no. 19, pp. 321–343, 1877.
- [84] A. Barman and A. Halder, *Solid State Physics*, vol. 65, ch. Time-Domain Study of Magnetization Dynamics in Magnetic Thin Films and Micro- and Nanostructures. Elsevier Inc., 2014.
- [85] L. Brillouin, “Diffusion of light and x-rays by a transparent homogeneous body,” *Ann. Phys.(Paris)*, vol. 17, p. 88, 1922.
- [86] H.-J. J. Liu, *Brillouin light scattering study of linear and nonlinear spin waves in continuous and patterned magnetic thin films*. PhD thesis, Colorado State University, 2014.
- [87] E. Hecht, *Optics*. San Francisco: Addison-Wesley, 4th ed.. ed., 2002.
- [88] J. R. Sandercock, *Tandem Fabry-Perot Interferometer TFP-1, Operator Manual*. JRS Scientific Instruments.
- [89] J. Sandercock, “Brillouin scattering study of SbSI using a double-passed, stabilised scanning interferometer,” *Optics Communications*, vol. 2, no. 2, pp. 73–76, 1970.
- [90] W. D. Wilber, *A Brillouin Light-Scattering Study of Parametric Magnons in Yttrium Iron Garnet at Microwave Frequencies*. CSU theses/dissertation, Colorado State University, 1987.
- [91] W. Wettling, W. D. Wilber, P. Kabos, and C. E. Patton, “Light scattering from parallel-pump instabilities in yttrium iron garnet,” *Phys. Rev. Lett.*, vol. 51, pp. 1680–1683, Oct 1983.

- [92] W. D. Wilber, W. Wettling, P. Kabos, C. E. Patton, and W. Jantz, “A wave-vector selective light scattering magnon spectrometer,” *Journal of Applied Physics*, vol. 55, no. 6, pp. 2533–2535, 1984.
- [93] C. E. Patton, “An idiots guide to tandem multi-pass Fabry-Perot alignment and operation,” Internal document.
- [94] K. S. Buchanan, “Companion to pattons idiot guide to BLS, updated for the TFP-DAS4,” Internal document.
- [95] H. Schultheiß and K. Vogt, “TFPDAS4 operator manual,” Hillebrands Group, University of Kaiserslautern.
- [96] V. E. Demidov, S. O. Demokritov, B. Hillebrands, M. Laufenberg, and P. P. Freitas, “Radiation of spin waves by a single micrometer-sized magnetic element,” *Applied physics letters*, vol. 85, no. 14, pp. 2866–2868, 2004.
- [97] H. Schultheiß and K. Vogt, “Micro-TFPDAS4 operator manual,” Hillebrands Group, University of Kaiserslautern.
- [98] R. P. Cowburn, D. K. Koltsov, A. O. Adeyeye, M. E. Welland, and D. M. Tricker, “Single-domain circular nanomagnets,” *Phys. Rev. Lett.*, vol. 83, pp. 1042–1045, Aug 1999.
- [99] T. Shinjo, T. Okuno, R. Hassdorf, †. K. Shigeto, and T. Ono, “Magnetic vortex core observation in circular dots of Permalloy,” *Science*, vol. 289, no. 5481, pp. 930–932, 2000.
- [100] V. L. Mironov, O. L. Ermolaeva, S. A. Gusev, A. Y. Klimov, V. V. Rogov, B. A. Gribkov, O. G. Udalov, A. A. Fraerman, R. Marsh, C. Checkley, R. Shaikhaidarov, and

- V. T. Petrashov, “Antivortex state in crosslike nanomagnets,” *Phys. Rev. B*, vol. 81, p. 094436, Mar 2010.
- [101] M. Pues, M. Martens, T. Kamionka, and G. Meier, “Reliable nucleation of isolated magnetic antivortices,” *Applied Physics Letters*, vol. 100, no. 16, p. 162404, 2012.
- [102] A. Fert, V. Cros, and J. Sampaio, “Skyrmions on the track,” *Nat Nano*, vol. 8, pp. 152–156, 03 2013.
- [103] K. L. Metlov and K. Y. Guslienko, “Stability of magnetic vortex in soft magnetic nano-sized circular cylinder,” *Journal of magnetism and magnetic materials*, vol. 242, pp. 1015–1017, 2002.
- [104] J. P. Park, P. Eames, D. M. Engebretson, J. Berezovsky, and P. A. Crowell, “Imaging of spin dynamics in closure domain and vortex structures,” *Phys. Rev. B*, vol. 67, p. 020403, Jan 2003.
- [105] S.-B. Choe, Y. Acremann, A. Scholl, A. Bauer, A. Doran, J. Stöhr, and H. A. Padmore, “Vortex core-driven magnetization dynamics,” *Science*, vol. 304, no. 5669, pp. 420–422, 2004.
- [106] V. Novosad, F. Y. Fradin, P. E. Roy, K. S. Buchanan, K. Y. Guslienko, and S. D. Bader, “Magnetic vortex resonance in patterned ferromagnetic dots,” *Phys. Rev. B*, vol. 72, p. 024455, Jul 2005.
- [107] K. Yamada, S. Kasai, Y. Nakatani, K. Kobayashi, H. Kohno, A. Thiaville, and T. Ono, “Electrical switching of the vortex core in a magnetic disk,” *Nat Mater*, vol. 6, pp. 270–273, 04 2007.
- [108] S. Pollard, L. Huang, K. Buchanan, D. Arena, and Y. Zhu, “Direct dynamic imaging of non-adiabatic spin torque effects,” *Nature communications*, vol. 3, p. 1028, 2012.

- [109] V. S. Pribiag, I. N. Krivorotov, G. D. Fuchs, P. M. Braganca, O. Ozatay, J. C. Sankey, D. C. Ralph, and R. A. Buhrman, “Magnetic vortex oscillator driven by d.c. spin-polarized current,” *Nat Phys*, vol. 3, pp. 498–503, 07 2007.
- [110] K. Perzlmaier, M. Buess, C. H. Back, V. E. Demidov, B. Hillebrands, and S. O. Demokritov, “Spin-wave eigenmodes of Permalloy squares with a closure domain structure,” *Phys. Rev. Lett.*, vol. 94, p. 057202, Feb 2005.
- [111] K. Vogt, O. Sukhostavets, H. Schultheiss, B. Obry, P. Pirro, A. A. Serga, T. Sebastian, J. Gonzalez, K. Y. Guslienko, and B. Hillebrands, “Optical detection of vortex spin-wave eigenmodes in microstructured ferromagnetic disks,” *Phys. Rev. B*, vol. 84, p. 174401, Nov 2011.
- [112] K. S. Buchanan, P. E. Roy, M. Grimsditch, F. Y. Fradin, K. Y. Guslienko, S. D. Bader, and V. Novosad, “Soliton-pair dynamics in patterned ferromagnetic ellipses,” *Nat. Phys.*, vol. 1, pp. 172–176, 12 2005.
- [113] S. Sugimoto, Y. Fukuma, S. Kasai, T. Kimura, A. Barman, and Y. Otani, “Dynamics of coupled vortices in a pair of ferromagnetic disks,” *Phys. Rev. Lett.*, vol. 106, p. 197203, May 2011.
- [114] B. Van Waeyenberge, A. Puzic, H. Stoll, K. W. Chou, T. Tyliczszak, R. Hertel, M. Fahnle, H. Bruckl, K. Rott, G. Reiss, I. Neudecker, D. Weiss, C. H. Back, and G. Schutz, “Magnetic vortex core reversal by excitation with short bursts of an alternating field,” *Nature*, vol. 444, pp. 461–464, 11 2006.
- [115] M. Sproll, M. Noske, H. Bauer, M. Kammerer, A. Gangwar, G. Dieterle, M. Weigand, H. Stoll, G. Woltersdorf, C. H. Back, and G. Schtz, “Low-amplitude magnetic vortex

- core reversal by non-linear interaction between azimuthal spin waves and the vortex gyromode,” *Applied Physics Letters*, vol. 104, no. 1, p. 012409, 2014.
- [116] S. Jain, V. Novosad, F. Fradin, J. Pearson, V. Tiberkevich, A. Slavin, and S. Bader, “From chaos to selective ordering of vortex cores in interacting mesomagnets,” *Nature communications*, vol. 3, p. 1330, 2012.
- [117] A. Kunz, E. C. Breitbach, and A. J. Smith, “Antivortex dynamics in magnetic nanostripes,” *Journal of Applied Physics*, vol. 105, no. 7, p. 07D502, 2009.
- [118] H. Wang and C. E. Campbell, “Spin dynamics of a magnetic antivortex: Micromagnetic simulations,” *Phys. Rev. B*, vol. 76, p. 220407, Dec 2007.
- [119] A. Drews, B. Krger, G. Meier, S. Bohlens, L. Bocklage, T. Matsuyama, and M. Bolte, “Current- and field-driven magnetic antivortices for nonvolatile data storage,” *Applied Physics Letters*, vol. 94, no. 6, p. 062504, 2009.
- [120] S. Gliga, M. Yan, R. Hertel, and C. M. Schneider, “Ultrafast dynamics of a magnetic antivortex: Micromagnetic simulations,” *Physical Review B*, vol. 77, no. 6, p. 4, 2008.
- [121] S. Gliga, R. Hertel, and C. M. Schneider, “Switching a magnetic antivortex core with ultrashort field pulses,” *Journal of Applied Physics*, vol. 103, no. 7, p. 3, 2008.
- [122] T. Kamionka, M. Martens, K. W. Chou, A. Drews, T. Tyliczszak, H. Stoll, B. Van Waeyenberge, and G. Meier, “Magnetic antivortex-core reversal by rotating magnetic fields,” *Phys. Rev. B*, vol. 83, p. 224422, Jun 2011.
- [123] A. Drews, B. Krüger, M. Bolte, and G. Meier, “Current- and field-driven magnetic antivortices,” *Phys. Rev. B*, vol. 77, p. 094413, Mar 2008.
- [124] A. Lyberatos, S. Komineas, and N. Papanicolaou, “Precessing vortices and antivortices in ferromagnetic elements,” *Journal of Applied Physics*, vol. 109, no. 2, p. 023911, 2011.

- [125] T. Kamionka, M. Martens, K. W. Chou, M. Curcic, A. Drews, G. Schütz, T. Tyliczszak, H. Stoll, B. Van Waeyenberge, and G. Meier, “Magnetic antivortex-core reversal by circular-rotational spin currents,” *Phys. Rev. Lett.*, vol. 105, p. 137204, Sep 2010.
- [126] M. Pues, M. Martens, and G. Meier, “Absorption spectroscopy of isolated magnetic antivortices,” *Journal of Applied Physics*, vol. 116, no. 15, p. 153903, 2014.
- [127] S. O. Demokritov and V. E. Demidov, “Micro-Brillouin light scattering spectroscopy of magnetic nanostructures,” *IEEE Transactions on Magnetism*, vol. 44, pp. 6–12, Jan 2008.
- [128] V. E. Demidov, S. O. Demokritov, B. Hillebrands, M. Laufenberg, and P. P. Freitas, “Radiation of spin waves by a single micrometer-sized magnetic element,” *Applied Physics Letters*, vol. 85, no. 14, pp. 2866–2868, 2004.
- [129] A. Vansteenkiste, J. Leliaert, M. Dvornik, M. Helsen, F. Garcia-Sanchez, and B. V. Waeyenberge, “The design and verification of MuMax3,” *AIP Advances*, vol. 4, no. 10, p. 107133, 2014.
- [130] M. P. Kostylev, G. Gubbiotti, J.-G. Hu, G. Carlotti, T. Ono, and R. L. Stamps, “Dipole-exchange propagating spin-wave modes in metallic ferromagnetic stripes,” *Phys. Rev. B*, vol. 76, p. 054422, Aug 2007.
- [131] C. E. Zaspel, B. A. Ivanov, J. P. Park, and P. A. Crowell, “Excitations in vortex-state Permalloy dots,” *Phys. Rev. B*, vol. 72, p. 024427, Jul 2005.
- [132] K. Y. Guslienko and A. N. Slavin, “Magnetostatic Greens functions for the description of spin waves in finite rectangular magnetic dots and stripes,” *Journal of Magnetism and Magnetic Materials*, vol. 323, no. 18, pp. 2418 – 2424, 2011.

- [133] V. E. Demidov, J. Jersch, S. O. Demokritov, K. Rott, P. Krzysteczko, and G. Reiss, “Transformation of propagating spin-wave modes in microscopic waveguides with variable width,” *Phys. Rev. B*, vol. 79, p. 054417, Feb 2009.
- [134] G. A. Riley, H. J. Liu, M. A. Asmat-Uceda, A. Haldar, and K. S. Buchanan, “Observation of the dynamic modes of a magnetic antivortex using Brillouin light scattering,” *Physical Review B*, vol. 92, no. 6, p. 064423, 2015.
- [135] G. E. W. Bauer, E. Saitoh, and B. J. van Wees, “Spin caloritronics,” *Nature Materials*, vol. 11, no. 5, pp. 391–399, 2012.
- [136] K. Uchida, J. Xiao, H. Adachi, J. Ohe, S. Takahashi, J. Ieda, T. Ota, Y. Kajiwara, H. Umezawa, H. Kawai, G. E. Bauer, S. Maekawa, and E. Saitoh, “Spin Seebeck insulator,” *Nat Mater*, vol. 9, no. 11, pp. 894–7, 2010.
- [137] J. Xiao, G. E. W. Bauer, K.-c. Uchida, E. Saitoh, and S. Maekawa, “Theory of magnon-driven spin Seebeck effect,” *Physical Review B*, vol. 81, no. 21, 2010.
- [138] K.-i. Uchida, H. Adachi, T. Ota, H. Nakayama, S. Maekawa, and E. Saitoh, “Observation of longitudinal spin-Seebeck effect in magnetic insulators,” *Applied Physics Letters*, vol. 97, no. 17, p. 172505, 2010.
- [139] B. Obry, V. I. Vasyuchka, A. V. Chumak, A. A. Serga, and B. Hillebrands, “Spin-wave propagation and transformation in a thermal gradient,” *Applied Physics Letters*, vol. 101, no. 19, p. 192406, 2012.
- [140] H. A. Algra and P. Hansen, “Temperature-dependence of the saturation magnetization of ion-implanted YIG-films,” *Applied Physics a-Materials Science and Processing*, vol. 29, no. 2, pp. 83–86, 1982.

- [141] S. V. Vasiliev, V. V. Kruglyak, M. L. Sokolovskii, and A. N. Kuchko, “Spin wave interferometer employing a local nonuniformity of the effective magnetic field,” *Journal of Applied Physics*, vol. 101, no. 11, p. 113919, 2007.
- [142] O. Dzyapko, I. V. Borisenko, V. E. Demidov, W. Pernice, and S. O. Demokritov, “Reconfigurable heat-induced spin wave lenses,” *Applied Physics Letters*, vol. 109, no. 23, 2016.
- [143] C. S. Davies, A. V. Sadovnikov, S. V. Grishin, Y. P. Sharaevskii, S. A. Nikitov, and V. V. Kruglyak, “Generation of propagating spin waves from regions of increased dynamic demagnetising field near magnetic antidots,” *Applied Physics Letters*, vol. 107, no. 16, p. 162401, 2015.
- [144] O. Kolokoltsev, I. Gómez-Arista, N. Qureshi, A. Acevedo, C. L. Ordóñez-Romero, and A. Grishin, “Compression gain of spin wave signals in a magnonic YIG waveguide with thermal non-uniformity,” *Journal of Magnetism and Magnetic Materials*, vol. 377, pp. 1–5, 2015.
- [145] M. J. Hurben and C. E. Patton, “Theory of magnetostatic waves for in-plane magnetized anisotropic films,” *Journal of Magnetism and Magnetic Materials*, vol. 163, no. 1-2, pp. 39–69, 1996.
- [146] V. Synogach, Y. Fetisov, C. Mathieu, and C. E. Patton, “Ultrashort microwave pulses generated due to three magnon interactions,” *Physical Review Letters*, vol. 85, no. 10, pp. 2184–2187, 2000.

- [147] T. Schneider, A. A. Serga, A. V. Chumak, C. W. Sandweg, S. Trudel, S. Wolff, M. P. Kostylev, V. S. Tiberkevich, A. N. Slavin, and B. Hillebrands, “Nondiffractive sub-wavelength wave beams in a medium with externally controlled anisotropy,” *Phys Rev Lett*, vol. 104, no. 19, p. 197203, 2010.
- [148] O. Buttner, M. Bauer, S. O. Demokritov, B. Hillebrands, Y. S. Kivshar, V. Grimalsky, Y. Rapoport, and A. N. Slavin, “Linear and nonlinear diffraction of dipolar spin waves in yttrium iron garnet films observed by space- and time-resolved Brillouin light scattering,” *Physical Review B*, vol. 61, no. 17, pp. 11576–11587, 2000.
- [149] R. Gieniusz, H. Ulrichs, V. D. Bessonov, U. Guzowska, A. I. Stognii, and A. Maziewski, “Single antidot as a passive way to create caustic spin-wave beams in yttrium iron garnet films,” *Applied Physics Letters*, vol. 102, no. 10, p. 102409, 2013.
- [150] V. E. Demidov, P. Rekers, B. Mahrov, and S. O. Demokritov, “Nonlinear transverse stabilization of spin-wave beams in magnetic stripes,” *Applied Physics Letters*, vol. 89, no. 21, p. 212501, 2006.
- [151] V. Veerakumar and R. E. Camley, “Magnon focusing in thin ferromagnetic films,” *Physical Review B*, vol. 74, no. 21, 2006.
- [152] J. Stigloher, M. Decker, H. S. Körner, K. Tanabe, T. Moriyama, T. Taniguchi, H. Hata, M. Madami, G. Gubbiotti, K. Kobayashi, *et al.*, “Snells law for spin waves,” *Physical review letters*, vol. 117, no. 3, p. 037204, 2016.

APPENDIX A

CATALOG OF MODES

A.1. LIST OF MODES TO ACCOMPANY CHAPTER 4

In this section we enumerate all the modes discussed in the antivortex project to aid the reader. The modes are separated by the orientation of the driving field and by whether they represent experimental data or simulated data as discussed further in Chapter 4.

TABLE A.1. List of modes for experimental data in-plane excitation

f_{AV} (GHz)	$f_{Sat_{\parallel}}$ (GHz)	$f_{Sat_{\perp}}$ (GHz)
2.8	4.1	2.3
3.4	4.7	4.6
4.0	5.7	5.1
4.3		5.7
5.2		
5.9		
6.2		

TABLE A.2. List of modes for simulation data for in-plane excitation

f_{AV} (GHz)	$f_{Sat_{\parallel}}$ (GHz)
1.90	4.32
2.22	5.44
3.08	5.70
3.27	
3.74	
5.44	
6.30	

TABLE A.3. List of modes for experimental data for out-of-plane excitation

f_{AV} (GHz)	f_{Sat} (GHz)
6.3	6.2
6.6	
6.8	

TABLE A.4. List of modes for simulation data for out-of-plane excitation

f_{AV} (GHz)	f_{Sat} (GHz)
2.40	2.70
7.20	3.70
7.59	4.60
8.50	7.20

APPENDIX B

DISPERSION CALCULATOR

B.1. HOW TO USE THE CODE

Below is a MATLAB script and function that can be used to calculate the dispersion relations for arbitrary wavevector combinations which allows for off axis propagation. This is useful when the antenna excites spin waves that are a hybrid of backward volume and surface wave character. It follows the theory in Ref. [20], which is outlined in Chapter 2. To use this code, the user must first enter a selection of material and experimental parameters into the interface script. The material parameters include the film thickness, saturation magnetization, gyromagnetic ratio, exchange coupling constant, Gilbert damping parameter, and pinning parameter. The experimental parameters are the external field and the angles that give the orientation of the field with respect to the film normal (θ) and with respect to the wavevector (ϕ). Lastly, the wavevector range and step size is set (where k_{DE} (kBV) indicates the wavevector component that is perpendicular (parallel) to the external field) and the number of thickness modes is selected. Typically the number of modes calculated should exceed the number of reported modes by 3. Finally, there is an option to perform the calculation without mode interaction by setting “approx” to “true”. This mode is useful when quick and rough calculations are needed or in thick films where the density of PSSW modes obscure the propagating DE mode. The script is set up to save the input parameters, that is, the variable “ui” and the output dispersion surface variable “data”, both of which are structure variables, in a MATLAB “.mat” output file. The “data” structure variable contains the dispersion surface matrices, where one matrix corresponds to one thickness mode, and the axes are the wavevector components (k_{DE} and k_{BV}).

B.1.1. THE INTERFACE SCRIPT. This MATLAB script is where the user will enter all the parameters discussed above.

```

1 %Script to calculate dispersion surfaces and group velocities
2 %Green' s function approach for spin wave manifold following
3 %Kalinikos, Slavin, J. Phys. C : Solid State Phys. 19 (1986) 7013 - 7033
4 %Main goal - to construct the L matrix (equation 37) and
5 %find its eigenvalues
6 %Written by Grant Riley in March 2017
7
8 close all;clear all;clc;
9
10
11 %%User Input
12 ui.L = 6.3e-4;
13 ui.H = 352;
14 ui.Ms = 1750; %1821 1810 1803 1796
15 ui.gamma = 2.8/1000;
16 ui.alpha = 3e-12;
17 ui.alphaG = 1e-5;
18 ui.pinned = false;
19 ui.theta = pi/2;
20 ui.terms = 6;
21 ui.kDErange = 0:1000:150000; %must use positive values
22 ui.kBVRrange = 0:1000:150000; %must use positive values
23 % ui.mirrorDE = false; %mirror over BV axis
24 % ui.mirrorBV = false; %mirror over DE axis
25 ui.dkint = 1000; %interpolation mesh step size
26 ui.approx = false;
27 %Sanity plots
28 plotsurfs=false;
29 plotints=false;
30
31 %%Call function
32 dat=fcn_dispersion(ui);
33
34
35 %%Pass out data
36 %Extract variables
37 freqs=dat.freqs;
38 intDErange=dat.intDErange;
39 intBVRrange=dat.intBVRrange;
40 intfreqs=dat.intfreqs;
41 vgDE=dat.vgDE;
42 vgBV=dat.vgBV;
43 vg=dat.vg;
44 %Create output structure
45 alldat.ui=ui;
46 alldat.dat=dat;
47
48 %%Plot dispersion surfaces to check appearance
49 if plotsurfs

```

```

50     figure;hold on;
51     for n=1:ui.terms
52         h(n)=surf(dat.kDErange,dat.kBVrange,freqs(:, :, n));
53         set(h(n), 'linestyle', 'none');
54     end
55     %plot styling
56     xlabel('k_D_E (rad/cm)', 'fontweight', 'bold');
57     ylabel('k_B_V (rad/cm)', 'fontweight', 'bold');
58     zlabel('Freq (GHz)', 'fontweight', 'bold');
59     fixplot(20);
60     view([-2 -2 1.5]);
61     hx=get(gca, 'xlabel');hy=get(gca, 'ylabel');
62     set(hx, 'rotation', 23);set(hy, 'rotation', -23);
63     set(gca, 'TickDir', 'in');
64     box on;grid on;
65 end
66
67 %%Plot interpolation surfaces to check appearance
68 if plotints
69     figure;hold on;
70     for n=1:ui.terms
71         h(n)=surf(intDErange,intBVrange,intfreqs(:, :, n));
72         set(h(n), 'linestyle', 'none');
73     end
74     %plot styling
75     xlabel('k_D_E (rad/cm)', 'fontweight', 'bold');
76     ylabel('k_B_V (rad/cm)', 'fontweight', 'bold');
77     zlabel('Freq (GHz)', 'fontweight', 'bold');
78     fixplot(20);
79     view([-2 -2 1.5]);
80     hx=get(gca, 'xlabel');hy=get(gca, 'ylabel');
81     set(hx, 'rotation', 23);set(hy, 'rotation', -23);
82     set(gca, 'TickDir', 'in');
83     box on;grid on;
84 end
85
86
87 %%Save output
88 myfolder='/Users/grant/Desktop/MATLAB disp calc pkg/';
89 filename=[myfolder, 'disp_YIG_Ms=', num2str(ui.Ms), 'G.H=', ...
90     num2str(ui.H), 'Oe_t=', num2str(ui.L*10^4), 'microns_terms=', ...
91     num2str(ui.terms), '_kmax=150000.mat'];
92 save(filename, 'alldat');

```

B.1.2. THE CALCULATING FUNCTION. This is the MATLAB function that is called to perform the actual computation. This function should not typically need to be changed by the user.

```

1 function [outdat] = fcn_dispersion(ui)
2
3

```

```

4 %Green' s function approach for spin wave manifold following
5 %Kalinikos, Slavin, J. Phys. C : Solid State Phys. 19 (1986) 7013 - 7033
6 %Main goal - to construct the L matrix (equation 37)
7 %and find its eigenvalues
8 %Written by Grant Riley in March 2017
9
10
11 %%User Input
12 L      =   ui.L;
13 H      =   ui.H;
14 Ms     =   ui.Ms;
15 gamma  =   ui.gamma;
16 alpha  =   ui.alpha;
17 alphaG =   ui.alphaG;
18 pinned =   ui.pinned;
19 theta  =   ui.theta;
20 terms  =   ui.terms;
21 kDErange = ui.kDErange;
22 kBVrange = ui.kBVrange;
23 %mirrorDE = ui.mirrorDE;
24 %mirrorBV = ui.mirrorBV;
25 dkint  =   ui.dkint;
26 approx =   ui.approx;
27
28
29 %%Initialization
30 freqs = zeros(length(kBVrange),length(kDErange),terms);
31 omegaM = gamma*Ms;
32 omegaH = gamma*H;
33 M=zeros(2*terms,2*terms);
34 Lmat=M;
35
36
37 %%Calculation
38 %Note - these coefficients are taken from Boris, Slavin 1986
39 %Boris' book chapter shows different B and C
40
41 %Output structure is:
42 %one kDEval per row increasing with index
43 %one KBVval per column increasing with index
44
45
46 for col=1:length(kDErange)
47 for row=1:length(kBVrange)
48     qDE=kDErange(col); qBV=kBVrange(row);
49     if abs(qBV) > 1
50         phi=atan(qDE/qBV); %phi is defined such that phi=0 along ...
51         % +kDE axis and phi=pi/2 along +kBV axis
52     else
53         phi=pi/2;
54     end
55     kz=sqrt(qDE^2 + qBV^2);
56     M=zeros(2*terms,2*terms);
57     Lmat=M;

```

```

57     for nn1=1:terms
58         if pinned
59             n1=nn1;
60         else
61             n1=nn1-1;
62         end
63         %first solve n1 == n2 terms to construct the non-interacting ...
           matrix Dnn
64         n2=n1;
65         kappa1=n1*pi/L;kappa2=n2*pi/L;
66         k1=sqrt(kz^2+kappa1^2);k2=sqrt(kz^2+kappa2^2);
67         if kz==0
68             F=0;
69         else
70             F=2/kz/L*(1-(-1)^n1*exp(-kz*L));
71         end
72         omegaN=omegaH/omegaM+alpha*k1^2;
73         if kz==0
74             p=0;
75         else
76             if pinned
77                 p=kz^2/k2^2*(n1==n2)+kz^2/k1^2*(kappa1*kappa2/k2^2) ...
78                   *F*((1+(-1)^(n1+n2))/2); %eq A10
79             else
80                 p=kz^2/k2^2*(n1==n2)-kz^4/k1^2/k2^2 ...
81                   *F/sqrt((1+(n1==0))*(1+(n2==0))) ...
82                   *((1+(-1)^(n1+n2))/2); %eq A12
83             end
84         end
85         q=0; %Solve equation 26 with n1 == n2
86         T=1; %Solve equation 27 with n1 == n2
87         AA=omegaN+1/2*(sin(theta)^2 ...
88           -(sin(theta)^2*cos(phi)^2-cos(theta)^2)*p); %eq 16a from ...
           Kalinikos 1989
89         BB=1/2*sin(theta)^2-1/2*(sin(theta)^2 ...
90           +(sin(phi)+i*cos(theta)*cos(phi))^2)*p; %eq 16b from Kalinikos ...
           1989
91         d11=AA;d22=AA;
92         d12=BB;d21=conj(BB);
93         Dmat=[d11,d12;d21,d22];
94         M(2*nn1-1:2*nn1,2*nn1-1:2*nn1)=Dmat;
95         Hmat=det(Dmat)*eye(2);
96         Lmat(2*nn1-1:2*nn1,2*nn1-1:2*nn1)=Hmat;
97         %now solve n1 != n2 terms to construct the off-diagonal ...
           compnents of the matrix L
98     for nn2=1:terms
99         if pinned
100             n2=nn2;
101         else
102             n2=nn2-1;
103         end
104         if n1==n2
105             continue
106         else

```

```

107     kappa2=n2*pi/L;
108     k2=sqrt(kz^2+kappa2^2);
109
110     if kz==0
111         p=0;
112     else
113         if pinned
114             p=kz^2/k2^2*(n1==n2)+kz^2/k1^2 ...
115             .* (kappal*kappa2/k2^2)*F*(1+(-1)^(n1+n2))/2; ...
116             %eq A10
117         else
118             p=kz^2/k2^2*(n1==n2)-kz^4/k1^2/k2^2*F/ ...
119             sqrt((1+(n1==0))*(1+(n2==0))) ...
120             *(1+(-1)^(n1+n2))/2;
121         end
122     end
123     if kz==0
124         q=0;
125     else
126         if pinned
127             q=kz^2/k2^2*(kappal*kappa2/(kappa2^2-kappal^2) ...
128             *2/kz/L+kappal*kappa2/2/k1^2*F) ...
129             *(1-(-1)^(n1+n2)); %eq A11
130         else
131             %eq 19 in Kalinikos 1981 - "Spectrum and Linear ...
132             Excitation of Spin Waves in Ferromagnetic Films"
133             %difference is the square root
134             q=kz^2/k2^2*(kappa2^2/(kappa2^2-kappal^2) ...
135             *2/kz/L-kz^2/2/k1^2*F)*(1-(-1)^(n1+n2)) ...
136             /sqrt((1+(n1==0))*(1+(n2==0)));
137         end
138     end
139     %Note - these (Pnn and Qnn) are taken from Boris, ...
140     Slavin 1986
141     %Both Pnn and Qnn are slightly different in Boris' 1981 ...
142     paper "Spectrum and Linear Excitation of Spin Waves ...
143     in Ferromagnetic Films"
144     if approx
145         M(2*nn1-1:2*nn1,2*nn2-1:2*nn2)=[0,0;0,0];
146         Lmat(2*nn1-1:2*nn1,2*nn2-1:2*nn2)=[0,0;0,0];
147     else
148         CC=-1/2*(sin(theta)^2*cos(phi)^2-cos(theta)^2)*p ...
149         -1i*sin(theta)*cos(theta)*cos(phi)*q;
150         DD1=-1/2*(sin(theta)^2+(sin(phi) ...
151         +1i*cos(theta)*cos(phi))^2)*p;
152         DD2=-sin(theta)*(sin(phi)+1i*cos(theta)*cos(phi))*q;
153         r11=CC;r22=CC;
154         r12=DD1+DD2;r21=conj(DD1-DD2);
155         Rmat=[r11,r12;r21,r22];
156         M(2*nn1-1:2*nn1,2*nn2-1:2*nn2)=Rmat;
157         Wmat=1\Dmat*Rmat*det(Dmat);
158         Lmat(2*nn1-1:2*nn1,2*nn2-1:2*nn2)=Wmat;
159     end

```

```

156         end
157     end
158 end
159 for n = 1:2*terms
160     u(n)=(-1)^(n-1);
161 end
162 W=(diag(u)-1i*alphaG*eye(2*terms))\M;
163 eigvals=sort(abs(real(eig(W))*omegaM));
164 for tmode=1:terms
165     freqs(row,col,tmode)=eigvals(2*tmode);
166 end
167 end
168 end
169
170
171 %%Interpolate the surfaces
172 intBVrange=min(kBVrange):dkint:max(kBVrange);
173 intDRange=min(kDRange):dkint:max(kDRange);
174 intfreqs=zeros(length(intBVrange),length(intDrange),terms);
175 vg=zeros(size(intfreqs));vgBV=vg;vgDE=vg;
176
177 [DEq,BVq]=meshgrid(intDRange,intBVrange);
178 for n=1:terms
179     intfreqs(:,:,n)=interp2(kBVrange,kDRange, ...
180         transpose(freqs(:,:,n)),BVq,DEq);
181     [vgDE(:,:,n),vgBV(:,:,n)]=gradient(2*pi*10^4*intfreqs(:,:,n)/dkint);
182     vg(:,:,n)=sqrt(vgDE(:,:,n).^2+vgBV(:,:,n).^2);
183 end
184
185 % %%Mirror data if requested
186 % if mirrorDE
187 %     freqs=cat(2,flip(freqs,2),freqs(:,2:end,:));
188 %     intfreqs=cat(2,flip(intfreqs,2),intfreqs(:,2:end,:));
189 %     kDRange=cat(2,flip(-kDRange),kDRange(2:end));
190 %     intDRange=cat(2,flip(-intDRange),intDRange(2:end));
191 % end
192 % if mirrorBV
193 %     freqs=cat(1,flip(freqs,1),freqs(2:end,:,:));
194 %     intfreqs=cat(1,flip(intfreqs,1),intfreqs(2:end,:,:));
195 %     kBVrange=cat(2,flip(-kBVrange),kBVrange(2:end));
196 %     intBVrange=cat(2,flip(-intBVrange),intBVrange(2:end));
197 % end
198
199 %%Pass data out of function
200 outdat.freqs=freqs;
201 outdat.intDRange=intDRange;
202 outdat.intBVrange=intBVrange;
203 outdat.intfreqs=intfreqs;
204 outdat.vgDE=vgDE;
205 outdat.vgBV=vgBV;
206 outdat.vg=vg;
207 outdat.kDRange=kDRange;
208 outdat.kBVrange=kBVrange;
209 end

```